



National Library
of Canada

Acquisitions and
Bibliographic Services Branch

395 Wellington Street
Ottawa, Ontario
K1A 0N4

Bibliothèque nationale
du Canada

Direction des acquisitions et
des services bibliographiques

395, rue Wellington
Ottawa (Ontario)
K1A 0N4

Your file *Votre référence*

Our file *Notre référence*

NOTICE

The quality of this microform is heavily dependent upon the quality of the original thesis submitted for microfilming. Every effort has been made to ensure the highest quality of reproduction possible.

If pages are missing, contact the university which granted the degree.

Some pages may have indistinct print especially if the original pages were typed with a poor typewriter ribbon or if the university sent us an inferior photocopy.

Reproduction in full or in part of this microform is governed by the Canadian Copyright Act, R.S.C. 1970, c. C-30, and subsequent amendments.

AVIS

La qualité de cette microforme dépend grandement de la qualité de la thèse soumise au microfilmage. Nous avons tout fait pour assurer une qualité supérieure de reproduction.

S'il manque des pages, veuillez communiquer avec l'université qui a conféré le grade.

La qualité d'impression de certaines pages peut laisser à désirer, surtout si les pages originales ont été dactylographiées à l'aide d'un ruban usé ou si l'université nous a fait parvenir une photocopie de qualité inférieure.

La reproduction, même partielle, de cette microforme est soumise à la Loi canadienne sur le droit d'auteur, SRC 1970, c. C-30, et ses amendements subséquents.

Canada

Hydrogen Storage in Metastable Fe-Ti

Pascal Tessier
Centre for the Physics of Materials
Department of Physics, McGill University
Montreal, Canada

A Thesis submitted to the
Faculty of Graduate Studies and Research
in partial fulfillment of the requirements for the degree of
Doctor of Philosophy

© Pascal Tessier, 1995



National Library
of Canada

Acquisitions and
Bibliographic Services Branch

395 Wellington Street
Ottawa, Ontario
K1A 0N4

Bibliothèque nationale
du Canada

Direction des acquisitions et
des services bibliographiques

395, rue Wellington
Ottawa (Ontario)
K1A 0N4

Your file *Votre référence*

Our file *Notre référence*

The author has granted an irrevocable non-exclusive licence allowing the National Library of Canada to reproduce, loan, distribute or sell copies of his/her thesis by any means and in any form or format, making this thesis available to interested persons.

L'auteur a accordé une licence irrévocable et non exclusive permettant à la Bibliothèque nationale du Canada de reproduire, prêter, distribuer ou vendre des copies de sa thèse de quelque manière et sous quelque forme que ce soit pour mettre des exemplaires de cette thèse à la disposition des personnes intéressées.

The author retains ownership of the copyright in his/her thesis. Neither the thesis nor substantial extracts from it may be printed or otherwise reproduced without his/her permission.

L'auteur conserve la propriété du droit d'auteur qui protège sa thèse. Ni la thèse ni des extraits substantiels de celle-ci ne doivent être imprimés ou autrement reproduits sans son autorisation.

ISBN 0-612-12496-7

Canada

*...ils sont alors comme un songe du matin,
comme un brin d'herbe verte
qui pousse et fleurit le matin,
mais que déjà le soir on coupe, et qui se fane.*

Ps. 89

CONTENTS

RÉSUMÉ	xi
ABSTRACT	xii
ACKNOWLEDGMENTS	xiii
STATEMENT OF ORIGINALITY	xv
1 INTRODUCTION	1
2 METAL-HYDROGEN SYSTEMS	7
2.1 Introduction	7
2.2 Thermodynamics of metal-hydrogen systems	9
2.3 Elastic interaction	14
2.3.1 Qualitative introduction	14
2.3.2 Discrete model	16
2.3.3 Continuum model	18
2.3.4 Coherency	20
2.3.5 Lattice expansion	21
2.3.6 Elastic energy	22
2.3.7 Validity of the Wagner-Horner theory	23
2.4 Hydrogen in amorphous alloys	23
2.5 Properties of real metal-hydrogen systems	26
2.6 Iron-titanium	27
2.6.1 The iron-titanium binary system	27
2.6.2 Hydrogen storage in Fe-Ti	28
2.6.3 Structure of iron-titanium hydrides	30
3 NANOPHASE MATERIALS	36
3.1 Overview	36
3.2 Grain boundaries	37
3.3 Hydrogen in nanophase materials	38
4 BALL MILLING	41
4.1 History of ball milling	41
4.2 The process of ball milling.	42
4.3 Amorphization by ball milling.	43
4.4 An analysis of the physics of ball milling.	43
4.5 The question of temperature.	44
4.6 Nanophase materials made by ball milling	45
4.7 CALPHAD calculations	45
4.7.1 Historical notes	45

4.7.2	Analytical formulation	45
4.7.3	Calculation of coefficients	46
4.7.4	Validity of CALPHAD calculations	47
5	EXPERIMENTAL METHODS	49
5.1	Milling procedure	49
5.2	X-ray apparatus	50
5.3	Analysis of X-ray data	51
5.3.1	Peak analysis	51
5.3.2	Determination of lattice parameter	52
5.3.3	Determination of crystallite size	53
5.3.4	Calculation of X-ray diffraction intensities	54
5.4	DSC measurements	55
5.5	Scanning electron microscopy	56
5.6	Chemical analysis	56
5.7	Hydrogen storage measurements	56
5.7.1	Description of the apparatus	56
5.7.2	Measurement sequence	58
5.7.3	Calibration	59
5.7.4	Preparation of samples	61
6	BALL MILLING OF FE-TI	63
6.1	Nanocrystalline $\text{Fe}_{50}\text{Ti}_{50}$	63
6.2	Amorphous phase and oxygen content	68
6.3	Lattice parameter	76
6.4	Mechanically alloyed $\text{Fe}_{50}\text{Ti}_{50}$	77
6.5	Amorphous $\text{Fe}_{67}\text{Ti}_{33}$	80
6.6	Nanocrystalline $\text{Fe}_{40}\text{Ti}_{60}$	83
6.7	General discussion	85
7	HYDROGEN STORAGE IN BALL-MILLED FE-TI	90
7.1	Overview of hydrogen storage results	90
7.2	Activation	93
7.3	Microstructure and phase stability	94
7.4	Discussion	100
7.4.1	Nanocrystalline Fe-Ti	100
7.4.2	Force-dipole tensor of FeTi	102
7.4.3	Spherical shell model	104
7.4.4	Uniform dispersion model	114
7.4.5	Chemical disorder	116
7.4.6	Nanocrystalline $\text{Fe}_{40}\text{Ti}_{60}$	119
7.4.7	Relaxation in amorphous Fe-Ti	119
7.5	Relaxation in nanocrystalline Fe-Ti revisited	121
7.6	Hydrogen absorption in nanocrystalline palladium	122
7.7	Kinetic properties	124

8 CONCLUSION	126
8.1 Milling experiments	126
8.2 Hydrogen storage experiments	127
8.2.1 Equilibrium properties	127
8.2.2 Kinetic properties	129
8.2.3 Future experiments	129
APPENDICES	130
A.1 Chemical potential of hydrogen gas.	130
A.2 Evaluation of the amorphous content.	134
REFERENCES	136

FIGURES AND TABLES

FIGURES

2.1	Pressure-composition isotherm of Pd-H at 300°C (measured in desorption) [59].	9
2.2	Phase diagram of Pd-H (taken from [59]). A mixture of phases is found below the line.	10
2.3	$y(c)$ for $a_{int}/kT = 0$	13
2.4	$y(c)$ for $a_{int}/kT = 4$	13
2.5	$y(c)$ for $a_{int}/kT = 8$	13
2.6	Free energy (schematic).	13
2.7	Potential energy of the host lattice (parabola), hydrogen-metal potential energy (straight line), and total potential energy (dashed line) as a function of lattice parameter expansion (ϵ). The dotted line shows the expansion at mechanical equilibrium.	14
2.8	Left: illustration of a metal lattice with one hydrogen atom. Right: illustration of a metal lattice with several hydrogen atoms. There is an overall expansion in addition to the local distortion around the hydrogen.	15
2.9	Tetrahedral site in bcc niobium.	18
2.10	Octahedral site in fcc palladium.	18
2.11	Left: illustration of a coherent interface. Right: illustration of an incoherent interface.	20
2.12	Pressure-concentration isotherms of crystalline and amorphous $Ni_{50}Zr_{50}$ (taken from [4]).	24
2.13	FeTi.	27
2.14	Phase diagram of Fe-Ti [95]. The stars are experimental points and the lines are calculated by the CALPHAD method.	28
2.15	Free energies of Fe-Ti phases at 300°C [95].	29
2.16	Pressure-composition isotherm of FeTi-H at 40°C (taken from [70]).	30
2.17	Phase diagram of FeTi-H (taken from [70]).	31
2.18	α -FeTiH _{0.06}	33
2.19	β_1 -FeTiH _{0.94} in the y-z plane (large cell: unit cell, small cell: FeTi distorted cell, Ti atoms and H2 sites are above the plane of the paper).	34
2.20	γ -FeTiH _{1.90} in the x-z plane (large cell: unit cell, small cell: FeTi distorted cell, Ti atoms and H4 sites are above the plane of the paper).	35
3.1	Schematic graph of the radial distribution function $g(r)$ for the three states of matter as a function of interatomic distance (in units of the atomic radius r_0).	37
5.1	X-ray diffraction patterns of iron and titanium powders used in this study.	50

5.2	Example of a fit for the [321] peak from the pure iron powder. The squares are experimental points and the solid line is the total calculated intensity which includes the diffraction peak and the linear background.	52
5.3	Lattice parameter as a function of diffraction angle for pure Fe.	53
5.4	Schematic diagram of a differential scanning calorimeter.	55
5.5	Gas-titration system.	57
5.6	Background signal from the gas-titration system for a hypothetical sample of one mole.	60
6.1	X-ray pattern of $\text{Fe}_{50}\text{Ti}_{50}$ (intermetallic compound) after 0, 0.5, 2, 10, 20, and 40 hours of milling.	64
6.2	Crystallite size as a function of milling time.	65
6.3	Strain as a function of milling time.	65
6.4	X-ray pattern of $\text{Fe}_{50}\text{Ti}_{50}$ (intermetallic compound) showing the (100) super-lattice peak at 0 and 20 hours of milling.	65
6.5	Long-range order parameter S of $\text{Fe}_{50}\text{Ti}_{50}$ (intermetallic compound) as a function of milling time.	65
6.6	X-ray pattern of $\text{Fe}_{50}\text{Ti}_{50}$ (elemental powders) after 0, 2, 5, 10, and 20 hours of milling.	66
6.7	X-ray pattern of $\text{Fe}_{50-\frac{x}{2}}\text{Ti}_{50-\frac{x}{2}}\text{O}_x$ after 20 hours of milling.	67
6.8	X-ray pattern fit of $\text{Fe}_{50}\text{Ti}_{50}$ (size: 6nm) [104] using one sharp peak. Dashed line: total calculated intensity (peak + background), dotted line: intensity from the peak alone.	69
6.9	X-ray pattern fit of $\text{Fe}_{50}\text{Ti}_{50}$ (size: 6nm) [104] using a sharp peak and a broad peak Dashed line: total calculated intensity, dotted lines: individual peaks.	69
6.10	X-ray pattern fit of $\text{Fe}_{50}\text{Ti}_{50}$ (size: 6nm) [104] using three sharp peaks.	69
6.11	X-ray pattern fit of $\text{Fe}_{50}\text{Ti}_{50}$ (size: 6nm) [104] using three sharp peaks and one broad peak.	69
6.12	Comparison between the superposition of the two broad peaks obtained by fitting the 6nm sample and the experimental amorphous X-ray pattern.	70
6.13	X-ray pattern fit of $\text{Fe}_{50}\text{Ti}_{50}$ milled 20 hours (size: 11nm) using one sharp peak.	70
6.14	X-ray pattern fit of the same 11nm sample using a sharp peak and a broad peak.	70
6.15	Comparison between the superposition of the two broad peaks obtained by fitting a sample milled 20 hours (size: 11nm) and the experimental amorphous pattern.	70
6.16	X-ray pattern fit of the 11nm sample using a sharp peak and the experimental pattern from amorphous $\text{Fe}_{45}\text{Ti}_{45}\text{O}_{10}$	71
6.17	(110) peak of coarse-grained FeTi	71
6.18	X-ray fit of nanocrystalline $\text{Fe}_{50}\text{Ti}_{50}$ (11nm) using the convolutions of Lorentzian functions and experimental peak functions together with the experimental pattern of amorphous $\text{Fe}_{50}\text{Ti}_{50}$ and a linear background.	71

6.19	Amorphous content versus the amount of oxygen from iron oxide in Fe-Ti-Fe ₂ O ₃ mixtures milled 20 hours.	71
6.20	Final crystallite size of Fe _{50-$\frac{x}{2}$} Ti _{50-$\frac{x}{2}$} O _x as a function of x.	72
6.21	Strain in nanocrystals contained in Fe _{50-$\frac{x}{2}$} Ti _{50-$\frac{x}{2}$} O _x samples as a function of x.	72
6.22	Lattice parameter of Fe ₅₀ Ti ₅₀ (intermetallic compound) as a function of milling time.	76
6.23	Lattice parameter as a function of long-ranger order parameter S. . .	76
6.24	X-ray pattern fit of elemental powders (composition Fe ₅₀ Ti ₅₀) milled 2 hours using 4 sharp peaks.	77
6.25	X-ray pattern fit of elemental powders (composition Fe ₅₀ Ti ₅₀) milled 2 hours using (in addition to the 3 α -Ti peaks and the Fe peak) a β -Ti(Fe) peak and a very broad peak corresponding to an amorphous phase. The experimental intensity is the solid line in a. The dashed line on the same graph is the total calculated intensity. The intensity from α -Ti and Fe is shown in b. The intensity from β -Ti(Fe) and amorphous Fe-Ti is shown in c. The scale of c is five times smaller than the scale of a and b.	78
6.26	X-ray pattern of Fe ₆₇ Ti ₃₃ (elemental powders) after 0, 0.5, 1, 2, 5, 10, and 20 hours of milling.	81
6.27	Scanning electron micrographs of Fe ₆₇ Ti ₃₃ (elemental powders) milled 0.5 hour.	82
6.28	DSC scan of Fe ₆₇ Ti ₃₃ milled 20 hours.	83
6.29	X-ray pattern of Fe ₄₀ Ti ₆₀ (elemental powders) after 0, 2, 5, and 20 hours of milling.	84
7.1	Pressure-composition isotherm for coarse-grained FeTi.	91
7.2	Pressure-composition isotherm for nanocrystalline FeTi made from the intermetallic compound FeTi (crystallite size: 12nm).	91
7.3	Pressure-composition isotherm for nanocrystalline Fe ₅₀ Ti ₅₀ made from elemental powders (crystallite size: 12nm).	91
7.4	Pressure-composition isotherm for nanocrystalline Fe ₅₀ Ti ₅₀ made from elemental powders (crystallite size: 6nm, result taken from [104], absorption only).	91
7.5	Pressure-composition isotherm for nanocrystalline Fe ₄₀ Ti ₆₀ (crystallite size: 11nm).	92
7.6	Pressure-composition isotherm for amorphous Fe ₆₇ Ti ₃₃ : squares: first storage cycle (absorption only), circles: after repeated storage cycles.	92
7.7	X-ray diffraction pattern of amorphous Fe ₆₇ Ti ₃₃ treated with palladium. The crystalline peaks are those of tungsten carbide impurities. There is not enough palladium to produce visible peaks.	96
7.8	X-ray diffraction pattern of coarse-grained FeTi before (a) and after (b) storage experiments.	96
7.9	X-ray diffraction pattern of nanocrystalline FeTi before (a) and after (b) storage experiments.	97

7.10	X-ray diffraction pattern of nanocrystalline Fe ₅₀ Ti ₅₀ before (a) and after (b) storage experiments.	97
7.11	X-ray diffraction pattern of nanocrystalline Fe ₄₀ Ti ₆₀ before (a) and after (b) storage experiments.	98
7.12	Pressure-composition isotherm of the crystalline component of coarse-grained FeTi (solid line) and nanocrystalline FeTi (dotted line), obtained by subtracting the amount of hydrogen corresponding to absorption in the amorphous phase using the isotherm of relaxed amorphous Fe ₅₀ Ti ₅₀	100
7.13	β_1 -FeTiH _{0.94} in the y-z plane (large cell: unit cell, small cell: FeTi distorted cell, Ti atoms and H atoms hiding iron are above the plane of the paper). Also drawn are the x and y axes of the initial FeTi cell, its z axis is normal to the paper. The x,y, and z sites are identified.	102
7.14	Spherical shell model.	104
7.15	Calculated pressure-composition isotherms for different amounts of amorphous phase with hydrogen concentration $c_a=0.35$, as calculated using the spherical shell model. The initial isotherm has a plateau at 12.6 atm and a maximum solubility in the α phase of 0.05 hydrogen/metal. The amorphous content is: (a) 0%, (b) 10%, (c) 20%, (d) 30%, (e) 40%.	110
7.16	Calculated pressure-composition isotherms for different amounts of amorphous phase with hydrogen concentration $c_a=0.45$, as calculated using the spherical shell model. The amorphous content is: (a) 0%, (b) 10%, (c) 20%, (d) 30%, (e) 40%.	110
7.17	Calculated pressure-composition isotherms for different amounts of amorphous phase with hydrogen concentration $c_a=0.55$, as calculated using the spherical shell model. The amorphous content is: (a) 0%, (b) 10%, (c) 20%, (d) 30%, (e) 40%.	111
7.18	Calculated pressure-composition isotherms for different concentrations of hydrogen in the amorphous phase: (a) $c_a=0.35$, (b) $c_a=0.45$, (c) $c_a=0.55$. The amorphous content of the material is set to 20%.	111
7.19	Calculated pressure-composition isotherms for different amounts of amorphous phase with hydrogen concentration $c_a=0.45$, as calculated using the spherical shell model. The volume expansion per hydrogen absorbed is assumed to be the same for the amorphous phase and β_1 -FeTiH _{0.94} . The amorphous content is: (a) 0%, (b) 10%, (c) 20%, (d) 30%, (e) 40%.	112
7.20	Uniform dispersion model.	114
7.21	Calculated pressure-composition isotherms using the uniform dispersion model for different amounts of amorphous phase: (a) 0%, (b) 5%, (c) 10%.	114
7.22	Calculated pressure-composition isotherms for partially disordered ($S = 0.9$) FeTi (b) and reference isotherm for fully ordered FeTi (a).	116
7.23	Pressure-composition isotherm for amorphous Fe ₅₀ Ti ₅₀ measured by L. Zaluski [108] (squares: as-milled material, triangles: relaxed material).	119

7.24	Pressure-composition isotherms of nanocrystalline Fe ₅₀ Ti ₅₀ with Pd catalyst measured by L. Zaluski [108]: (a) as-milled, (b) after annealing at 300°C for 0.5 hour, (c) at 400°C for 0.5 hour, (d) after long annealing at 400°C.	122
7.25	Concentration as a function of time in coarse-grained FeTi (squares) and nanocrystalline FeTi (triangles) at early times.	124
7.26	Concentration as a function of time in coarse-grained FeTi (solid line) and nanocrystalline FeTi (dashed line) for long times.	124
A.1	Peak functions determined from the X-ray pattern of coarse-grained FeTi and used for fitting experimental peaks in patterns with an amorphous component.	134

TABLES

0.1	Acknowledgments regarding McGill colleagues.	xiv
1.1	Hydrogen content in various media (taken from [2]).	1
2.1	Structure of FeTi hydrides.	32
2.2	Atomic positions in α -FeTiH _{0.06}	33
2.3	Atomic positions in β_1 -FeTiH _{0.94} and β_2 -FeTiH _{1.40}	34
2.4	Atomic positions in γ -FeTiH _{1.90}	35
6.1	Peak areas of a 11nm sample for each type of correction for the amorphous content (first column: direction, second column: no correction, third: corrected with a broad peak, fourth corrected with the experimental amorphous pattern, fifth: FeTi intermetallic (experimental), sixth: FeTi intermetallic (calculated)).	72
7.1	Pressure of the absorption and desorption plateaus of each crystalline sample (in atmospheres). The midpoint is determined from the arithmetic mean of the logarithm of the two plateaus.	90
7.2	Crystallite size of samples after activation and repeated hydrogen absorption-desorption cycles (in nanometers). For coarse-grained FeTi, the linear regression led to the origin of the axes with the error bar spanning positive and negative values. The domain size along the [h00] direction is too large to be accurately determined from the width of X-ray peaks.	94
7.3	Strain values for samples after activation and repeated hydrogen absorption-desorption cycles.	95
7.4	Amorphous content, lattice parameter d , and long-range order parameter S of samples as-milled.	95
7.5	Amorphous content, lattice parameter d , and long-range order parameter S of samples after activation and repeated hydrogen absorption-desorption cycles.	95
7.6	Number of each site per metal atom for $S = 0.9$	117

RÉSUMÉ

Le broyage à haute énergie du système Fe-Ti est réalisé pour une gamme étendue de compositions. Les compositions $\text{Fe}_{50}\text{Ti}_{50}$ et $\text{Fe}_{40}\text{Ti}_{60}$ produisent un composite amorphe-nanocristaux sous l'effet du broyage. Un amorphe pur est produit dans le cas du $\text{Fe}_{67}\text{Ti}_{33}$. Cet alliage amorphe absorbe l'hydrogène, contrairement au composé intermétallique de même composition. Les alliages nanocristallins quant à eux présentent un rétrécissement du plateau d'absorption et un abaissement de la pression de ce plateau. Cette modification des propriétés d'absorption est due à l'interaction entre les nanocristaux et la phase amorphe. Cette interaction est analysée à l'aide d'un modèle simplifié des contraintes élastiques. Enfin, l'hydrogène est absorbé beaucoup plus rapidement par les alliages nanocristallins que par les matériaux conventionnels.

ABSTRACT

High energy ball milling of the Fe-Ti system is carried out over a wide range of compositions. Milling $\text{Fe}_{50}\text{Ti}_{50}$ and $\text{Fe}_{40}\text{Ti}_{60}$ produces a composite material with amorphous regions and nanometer-sized crystals. Milling $\text{Fe}_{67}\text{Ti}_{33}$ leads to a single-phase amorphous alloy which absorbs hydrogen, in sharp contrast to the intermetallic compound of the same composition. The nanocrystalline samples on their part exhibit a narrowing of the miscibility gap and a reduction of the pressure of the absorption plateau. The change in absorption properties, which is due to the interaction between the nanocrystals and the amorphous phase, is analyzed using a simplified model of the elastic stress. Finally, hydrogen is absorbed much faster by nanocrystalline alloys than by conventional materials.

ACKNOWLEDGMENTS

This thesis is the result of a lot of work... and a lot of time. During this time, I have worked with some people, shared fun and friendship with a few, and coexisted with some others.

I must first thank my supervisor, professor John Ström-Olsen, whose “no nonsense” approach to physics I respect, together with his attitude of not giving too much attention to algebraic details. I have also appreciated his view that only excellence should be sought and rewarded. I also thank my co-supervisor, Dr. Robert Schulz, at Hydro-Québec. His enthusiasm to explore new things is contagious and stimulating.

I also thank the staff at McGill: Frank Van Gils, Michel Champagne, Cynthia MacDonald, professor Martin Zuckermann (mostly for his exquisite jokes), Dr. Zaven Altounian for his expertise on thermal analysis; and the people at IREQ: Raynald Rioux, Alain Joly, René Dubuc, Zhi-Hua Yan, and Michel Trudeau. I must give a special mention to Leszek Zaluski and Alicja Zaluska who have been helpful and friendly.

My studies have been supported by the Fonds FCAR, the Ministry of Energy and Resources of Québec, Hydro-Québec, and the Natural Sciences and Engineering Research Council of Canada.

I thank all my colleagues, in particular those of room 421. Table 0.1 gives an account of what has to be attributed to each person.

I must finally thank all the members of my family for their encouragements — and, in some cases, for their financial support —, especially Alain, Sylvain, Dominique, Françoise, Monique, Anne-Marie.

A most important person to thank for her help during this part of my life is my mother. I wish there was a way to say how much I owe her.

This is a moment my father would have liked to see. Unfortunately he could not stay with us any longer. What he has accomplished during his life will last in my memory far longer than anything I have done during my studies.

Table 0.1: Acknowledgments regarding McGill colleagues.

Karim Aguenou	friendship, political discussions
Geoffrey Soga	friendship, cool attitude toward life
Eugenia Corvera Poiré	friendship, social catalysis
Judith Müller	friendship, parties
Nick Provatas	his thoughts about hockey and politics
Erol Girt	friendship, parties, singing
Martin Lacasse	constructive criticism, crucial help with his ©Fudgit program and computers in general
Eric Dufresne	all the fun
Réjean Ducharme	
Mikko Karttunen	
Morten Nielsen	
Ross Thompson	
Margarita Koknaeva	
Noureddine Hambli	
Yan-Bin Wang	
Oleh Baran	
Benoît Lussier	
Stéphane Legault	
Grażyna Rudkowska	
François Drolet	
May Chiao	
Robert Gagnon	
Nicolas Desaulniers-Soucy	
Denis Michaud	

STATEMENT OF ORIGINALITY

The author claims the following aspects of the thesis to be original contributions to the advancement of knowledge.

- The first comprehensive study of a nanocrystalline metal hydride made by ball milling.
- The establishment of a correlation between oxygen content and amorphous fraction in ball-milled nanocrystalline Fe-Ti from X-ray diffraction measurements. An oxygen limit above which complete amorphization occurs has previously been reported [104], but we have also found a relation of proportionality to exist in cases of partial amorphization.
- The complete amorphization of $\text{Fe}_{67}\text{Ti}_{33}$ by mechanical alloying. Partial amorphization was achieved by Cocco et al. [16], Eckert et al. [26], and Chu et al. [15].
- The measurement of the enthalpy of crystallization of amorphous $\text{Fe}_{67}\text{Ti}_{33}$ obtained by mechanical alloying.
- The measurement of pressure-composition isotherms of hydrogen in ball-milled Fe-Ti at non-equiatomic compositions.
- The extension of the Wagner-Horner theory of the elastic interaction in metal-hydrogen systems to the case of crystals subjected to an external stress and the application of this model to the explanation of the hydrogen storage properties of ball-milled nanocrystalline Fe-Ti.

INTRODUCTION

In the search for alternative fuels, hydrogen stands as the ideal candidate, its combustion essentially producing water vapor. The main problem limiting the widespread use of hydrogen is the difficulty to store it in a safe and practical manner.

Hydrogen can be stored in three states: gas, liquid, and metal hydride. Gaseous storage gives a very low volume density while heavy metal containers are required for the use of high pressures. This form of storage is also dangerous, especially in vehicles since containers ruptured in accidents would pose a risk of explosion. Liquid storage is very efficient, both in terms of volume and mass density. The refrigeration system required makes this solution complicated. In addition, liquid hydrogen evaporates and losses could be important during long-term storage.

Metal hydrides certainly constitute the safest method of storing hydrogen. They can absorb up to one hydrogen atom per metal atom, this gives a higher volume density than the liquid state. Hydrogen can be dissolved in certain absorbing alloys at

Table 1.1: Hydrogen content in various media (taken from [2]).

medium	moles of H per cm ³	weight percent of H
H ₂ gas at 100atm	0.81	100
H ₂ liquid	7.0	100
MgH ₂	11.1	7.6
Mg ₂ NiH ₄	9.8	3.8
FeTiH _{1.90}	10.0	1.8
LaNi ₅ H ₆	12.6	1.5

a few atmospheres of pressure, kept there an indefinite amount of time, and retrieved by heating the alloy at a few hundred degrees. Alloys with a wide variety of absorption characteristics exist. Unfortunately metal hydrides are crippled by several problems, which we will now describe.

Hydrogen absorbing metals and alloys are generally very sensitive to surface contamination. They easily form oxides which block the passage of hydrogen atoms into the material. Because of this, metals exposed to air have to be subjected to an activation treatment at high temperatures and hydrogen pressures. If, in the course of its use, a metal hydride is exposed to air, the activation treatment must be repeated, ultimately resulting in the degradation of the storage capacity.

Crystalline metal hydrides have a miscibility gap, this means there is a concentration range where a homogeneous hydride phase is unstable. Upon hydrogen absorption, the hydrogen concentration reaches a solubility limit, after which regions with very high hydrogen content start forming if more hydrogen is dissolved. This inhomogeneous absorption translates into an inhomogeneous expansion of the material and this leads to decrepitation. The miscibility gap is reached at a certain pressure which depends on temperature and on the material. The gap shows up on pressure-composition isothermal curves as a plateau where the pressure is constant over a wide concentration range. It is an advantage from the point of view of storage since hydrogen can be successively stored and retrieved by a moderated change in pressure. Amorphous alloys, which are very disordered and have a wide distribution of binding energies, do not exhibit a plateau. Therefore they do not decrepitate but their storage properties are not as interesting since one must change the pressure by a large amount to either store or recuperate hydrogen. Decrepitation poses problems in terms of how the metal hydride powder is to be kept inside a container.

Finally, by their very nature, metal hydrides are heavy. The exception is magnesium hydride, which has a very good hydrogen mass density. Unfortunately it is the most easily oxidized metal hydride. Table 1 gives the volume density and weight percent of hydrogen of various forms of storage.

In the hope of improving the properties of metal hydrides, our group has initiated a detailed study of hydrogen storage in nanocrystalline alloys. Nanocrystalline

materials are polycrystalline materials with nanometer-sized crystallites (typically 5-100nm). In this fine microstructure an important fraction of the atoms are located at grain boundaries. Depending on the thickness of those boundaries — a currently controversial issue —, up to 50% of the atoms can be included in them. In any case, a large number of atoms in nanocrystalline materials are located within a few lattice spacings of grain boundaries. This microstructure should provide a wide variety of storage sites with binding energies more or less different from normal sites found in conventional materials. For example close to grain boundaries, especially incoherent grain boundaries, the crystal lattice will be strained, and storage sites located there will have their binding energies slightly changed. This is also true for coarse-grained material but their low density of grain boundaries makes it a negligible factor. The large number of interfaces and free surfaces, could enhance diffusion and possibly reduce decrepitation. Since nanocrystalline materials already have a very fine microstructure, hydrogenation may not necessarily break it up further. As to diffusion, it cannot be known in advance whether interfaces are a better environment for the diffusion of hydrogen, this is something our experiments are intended to reveal.

Having decided to investigate hydrogen storage in nanocrystalline materials, we had to choose a particular material and an appropriate method of synthesis. It was decided by our group to study FeTi first. FeTi is a well known storage compound with a total capacity of approximately one hydrogen atom per metal atom. Its constituent elements are also inexpensive. Its weight may limit its use to stationary applications. The work on FeTi described in this thesis was conducted in parallel with other members of our group working on other compounds.

There are three widely used methods for the synthesis of nanocrystalline metals and alloys: gas phase condensation, crystallization of an amorphous phase, and ball milling. In the condensation method, a metal is evaporated inside a chamber filled with an inert gas and collected on a cold finger. Nanometer-sized clusters are obtained by scraping the surface of the cold finger. Dense materials are obtained by compaction in ultra-high vacuum. The samples obtained by condensation are small (a few milligrams) and, in our opinion, using it for alloys may pose problems regarding the precise control of the chemical composition of the clusters.

The method of crystallization of the amorphous phase cannot be used for large samples in the Fe-Ti system. We were unable to make amorphous FeTi by melt-spinning and ball milling produces an amorphous phase only for compositions close to $\text{Fe}_{67}\text{Ti}_{33}$ or by adding oxygen. Amorphous Fe-Ti has been prepared by Sumiyama et al. [80] using vapor quenching, but the samples so-produced are inherently small and impractical for purposes of hydrogen storage.

In ball milling, balls made of a very hard material, steel or tungsten carbide, are moving rapidly inside a rotating or vibrating container with thick walls. The balls collide repeatedly and transfer energy to the powder trapped between them. This mechanical energy transfer causes deformations in the material. If we start with a single phase material, the deformation process causes a refinement of the microstructure and, in certain cases, structural transformations. If we start with a multi-component material, the milling process creates a large number of interfaces where chemical reactions can take place. In both cases a steady-state is reached where the final product normally depends only on the average chemical composition and milling conditions. Ball milling is a non-equilibrium process and thus permits the formation of metastable phases which can not be synthesized by conventional means. Ball milling has the advantage of producing large amounts of material (a few grams with laboratory equipment) and industrial scale mills already exist.

In addition we wanted to try making amorphous Fe-Ti, with the intention of controlling the crystallite size from large to very small values. The amorphous phase would correspond to the limit when the size goes to zero. Fe-Ti is not a good system for melt-spinning since amorphous phase formation is expected only close to a low temperature eutectic, something which is not found in the phase diagram of Fe-Ti. As mentioned above, our attempt was only partially successful. We made amorphous Fe-Ti only at the $\text{Fe}_{67}\text{Ti}_{33}$ composition. We could have tried using this material to make nanocrystalline Fe_2Ti by crystallization of the amorphous phase but this compound does not absorb hydrogen (iron has much less affinity for hydrogen than titanium), therefore we found limited interest in such an experiment.

Ball milling experiments on Fe-Ti have already been performed by several groups [27, 21, 15, 16]. However results concerning amorphous phase formation vary and the sub-

ject requires further investigation.

The synthesis of nanocrystalline materials is a subject of study in itself. Among the different methods of characterization, X-ray diffraction is probably the most useful. It gives precise information concerning the amount of each phase present. It also permits indirect determination of the crystallite size and strain level from the width of the peaks. In the case where two elements diffuse in each other, the lattice parameter can provide information on interdiffusion. X-ray diffraction is thus a very appropriate method for the study of phase transformations and was the main characterization method used here.

Our storage experiments were carried out in a gas-titration apparatus. Electrochemical storage where the sample serves as the cathode is another possible method of measurement but it is not as simple as gas phase measurements, and not very practical in the case of FeTi. Most of the absorption in this system occurs above atmospheric pressure and additives would have to be used in the electrolyte to prevent the evolution of hydrogen (the formation of bubbles of hydrogen at the surface of the sample). Gas storage is insensitive to the form or shape of the sample, provided that hydrogen can diffuse easily throughout the sample. This is an important factor since metal hydrides decrepitate during absorption-desorption cycles. In electrochemical measurements, we would be forced to deal with problems of mechanical integrity of the cathode.

Our investigation of hydrogen storage in ball-milled Fe-Ti will focus on the following objectives. We will determine the phase transformations occurring during milling and try to describe the reaction mechanisms involved. As to hydrogen storage, we intend to determine the new thermodynamic properties of the Fe-Ti-H system. This is especially interesting since nanocrystalline materials have significantly altered thermodynamic properties compared to their coarse-grained counterparts. In view of possible applications we will also report the changes in kinetic properties and activation behavior upon crystallite size refinement. We will finally attempt to relate our results to the findings of other groups on nanocrystalline palladium hydride. Mütschele and Kirchheim [63] followed by Eastman et al. [23] have observed a narrowing of the miscibility gap in the Pd-H system. Grain boundary regions are thought to be

responsible for these changes but the precise interpretation of the results is a cause of disagreement. In Fe-Ti we also expect the hydrogen storage properties to be affected by the high density of grain boundaries and by the chemical disorder induced by ball milling. A precise characterization of the material will be important in order to attempt explaining the properties of nanocrystalline Fe-Ti.

Our presentation is organized in the following manner. In chapter 2 we give an introduction to the properties of metal-hydrogen systems with a particular emphasis on the elastic interaction between absorbed hydrogen atoms. Chapter 3 summarizes the recent developments in the field of nanophase materials with a section on the palladium-hydrogen system. We describe the method of ball milling in chapter 4. The detailed description of our experimental methods as well as our procedure used for data analysis is found in chapter 5.

The results are given in the two following chapters: the synthesis of nanocrystalline and amorphous Fe-Ti in chapter 6, and the storage properties in 7. They are followed by a few concluding remarks in chapter 8.

METAL-HYDROGEN SYSTEMS

2.1 Introduction

The field of hydrogen absorption by metallic materials dates back as far as 1866 [39]. The imperatives of technological progress have recently given the research community the motivation to deepen its understanding of the phenomenon. A considerable amount of work has been devoted to the study of the detrimental effect of hydrogen on structural materials (steel embrittlement) and semiconductors (hydrogen impurities in silicon).

Several hydrogen absorbing metals and compounds such as Nb, V, LaNi_5 , and FeTi have been studied in the last forty years but no widespread commercial application has resulted so far. At the time of writing, there is renewed interest in the use of hydrogen storage materials.

Before we give the important results to be used in our study, we must first give some definitions and basic results. Metal-hydrogen systems are often referred to as hydrides. In this work the definition by Fukai [34] will be used. This definition includes metal-hydrogen systems where the hydrogen changes the crystalline structure (topological change) and those where the hydrogen atoms in solution at least form an ordered structure while the host lattice undergoes a slight distortion and expansion.

Many metals and intermetallic compounds absorb large amounts of hydrogen. The H_2 molecule is dissociated at the surface and the H atoms are adsorbed and then absorbed into the bulk of the material, their electron contributing to the electronic bands of the host metal [34].

The equilibrium data on metal-hydrogen systems is usually presented in the form of isothermal pressure-composition curves. We present the data for palladium which

is the most widely studied and was the first discovered hydrogen absorbing metal [39] (figure 2.1). The isothermal curve gives the relation between hydrogen pressure and hydrogen concentration in the material at equilibrium, temperature being kept constant. If pressure-composition isotherms are obtained for a range of temperatures, a phase diagram can be established (figure 2.2).

Isotherms measured during absorption are generally different from those measured during desorption. Isotherms measured during desorption are normally shifted to lower pressures with respect to that obtained during absorption. This hysteresis is caused by plastic work occurring during the formation and decomposition of the hydride phase.

In the low pressure region, we find a disordered solution. The hydrogen is randomly distributed over storage sites (fcc octahedral sites in the case of Pd-H). In this pressure range the concentration varies very slowly with pressure. The concentration roughly follows Sieverts law:

$$c \propto \sqrt{P}. \quad (2.1)$$

At a certain pressure, which depends on temperature and on the absorbing material, the concentration increases while there is no change in hydrogen pressure. A so-called "plateau" is reached. After this plateau is passed an increase in pressure is again necessary in order to augment the hydrogen concentration. The plateau corresponds to the formation of a hydride phase. Instead of having a continuous change of hydrogen concentration with hydrogen pressure, regions of hydride phase (regions with high hydrogen concentration) start forming. We thus have a phase separation which occurs below the critical temperature. The plateau region is also referred to as a miscibility gap. Above the critical temperature there is no phase separation and the relation between concentration and pressure is continuous (figure 2.2). The phase separation is due to the interaction between dissolved hydrogen atoms. The interaction includes an elastic as well as an electronic contribution. Their relative importance varies from one system to another. In the case of Pd-H, it is nearly equal [20]. This transformation from a phase with low concentration to a phase with high concentration is responsible for the hysteresis observed as the material passes through a full absorption-desorption cycle. As regions of high concentration grow,

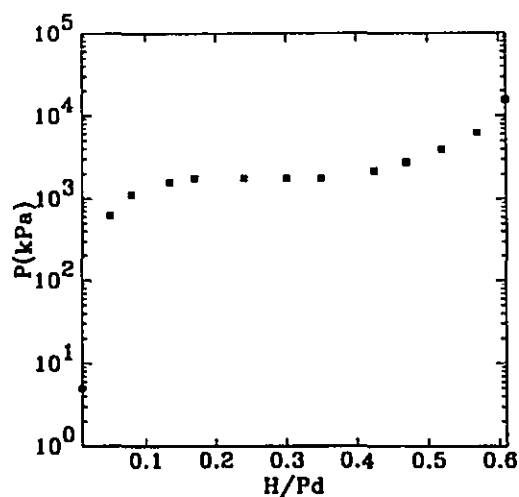


Figure 2.1: Pressure-composition isotherm of Pd-H at 300°C (measured in desorption) [59].

plastic work occurs because of the inhomogeneous lattice expansion. Upon absorption the pressure must be raised higher than the equilibrium plateau pressure in order to initiate the transformation. In the same manner, upon desorption, the pressure has to be decreased further than the equilibrium pressure in order to decompose the hydride phase. The equilibrium pressure-composition isotherm is that which would be observed were there no interface between the low-concentration solution and the hydride phase. The absence of a miscibility gap above the critical temperature is due to the thermal motion of the hydrogen atoms, which is such that phase separation is no longer possible and a homogeneous disordered solution is found at all hydrogen pressures.

2.2 Thermodynamics of metal-hydrogen systems

At equilibrium the chemical reaction



has equal reaction rates in both directions. From a thermodynamic point of view, the hydrogen gas is in equilibrium with the hydrogen in solution in the metal host if the Helmholtz free energy A of the combined gas-solution system is at a minimum. The

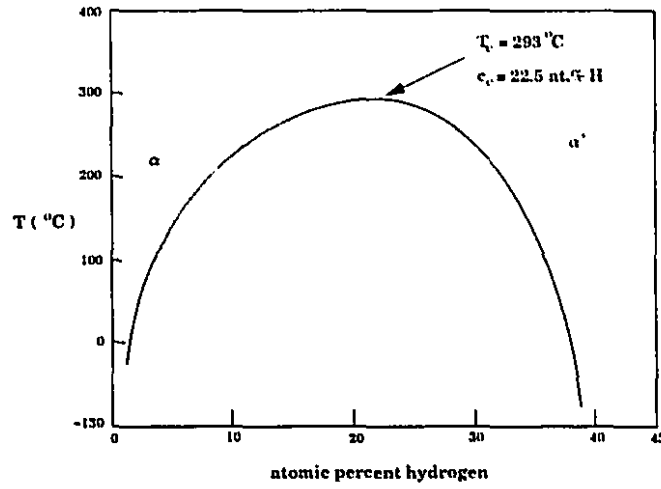


Figure 2.2: Phase diagram of Pd-H (taken from [59]). A mixture of phases is found below the line.

total number of hydrogen atoms is conserved:

$$N_{total} = 2N_{gas} + N. \quad (2.3)$$

N , the number of hydrogen atoms dissolved, completely determines the state of the system. There is a factor 2 in front of the number of H_2 molecules N_{gas} because there are two hydrogen atoms per molecule. The free energy is at a minimum if

$$\frac{\partial A}{\partial N} = 0. \quad (2.4)$$

The total free energy comprises that of the hydrogen gas and that of the metal-hydrogen solution:

$$A = A_{H_2gas} + A_{solution}. \quad (2.5)$$

Equation (2.4) becomes:

$$\frac{\partial A_{H_2gas}}{\partial N} + \frac{\partial A_{solution}}{\partial N} = 0 \quad (2.6)$$

$$\frac{\partial A_{H_2gas}}{\partial N_{gas}} \frac{dN_{gas}}{dN} + \frac{\partial A_{solution}}{\partial N} = 0. \quad (2.7)$$

From (2.3) we have

$$\frac{dN_{gas}}{dN} = -\frac{1}{2} \quad (2.8)$$

and (2.7) becomes

$$\frac{1}{2} \frac{\partial A_{H_2gas}}{\partial N_{gas}} = \frac{\partial A_{solution}}{\partial N}, \quad (2.9)$$

Where

$$\frac{\partial A_{H_2gas}}{\partial N_{gas}} = \mu_{H_2gas} \quad (2.10)$$

is the chemical potential of the gas and

$$\frac{\partial A_{solution}}{\partial N} = \mu_{solution} \quad (2.11)$$

is that of the metal-hydrogen solution. Equation (2.9) is the well known rule that several phases of the same constituent are in equilibrium with each other if the chemical potentials of all phases are equal:

$$\frac{1}{2} \mu_{H_2gas} = \mu_{solution}, \quad (2.12)$$

using (2.10) and (2.11). There would not be a factor of $\frac{1}{2}$, had we chosen to define the chemical potential of hydrogen gas as the derivative of the free energy with respect to the number of hydrogen atoms instead of the number of hydrogen molecules.

The chemical potential of hydrogen gas is

$$\mu_{H_2gas} = E_d + kT \ln \left(\frac{P}{P_0} \right), \quad (2.13)$$

where E_d is the dissociation energy of the hydrogen molecule, k is Boltzmann's constant, T is the temperature, and P_0 varies as $T^{7/2}$. The derivation of equation (2.13) and the significance of P_0 is found in appendix A.1.

On the other hand the free energy of the hydrogen in solution is:

$$A = H_{solution} - TS_{solution} \quad (2.14)$$

$$A = H_s - TS_{nc} - TS_c. \quad (2.15)$$

S_{nc} and S_c are respectively the non-configurational and configurational parts of the entropy.

The configurational part is:

$$S_c = k \ln \left[\frac{N!}{N_H!(N - N_H)!} \right]. \quad (2.16)$$

N is the number of dissolved hydrogen atoms and N_H the number of sites (one type of site is assumed). The non-configurational part includes vibrational and electronic contributions. The chemical potential follows:

$$\mu_{solution} = \frac{\partial A}{\partial N} \quad (2.17)$$

$$\mu_{solution} = \frac{\partial H_s}{\partial N} - T \frac{\partial S_{nc}}{\partial N} + kT \ln \left(\frac{N}{N_H - N} \right) \quad (2.18)$$

$$\mu_{solution} = \mu_0(T) + kT \ln \left(\frac{c}{1-c} \right) - a_{int}c. \quad (2.19)$$

where $c = N/N_H$ is the hydrogen concentration and $\mu_0(T)$ depends on temperature but not on concentration. The term $(-a_{int}c)$ is the first-order correction, in terms of concentration, to $\partial H_s/\partial N$ and $-T(\partial S_{nc}/\partial N)$. This last term in (2.19) expresses the interaction between hydrogen atoms dissolved in the metallic matrix.

Substituting (2.13) and (2.19) in (2.12) gives us the relation between pressure and concentration:

$$\frac{1}{2}kT \ln \left(\frac{P}{P_0} \right) = \mu_0(T) - \frac{E_d}{2} + kT \ln \left(\frac{c}{1-c} \right) - a_{int}c. \quad (2.20)$$

The plot of the function

$$y(c) = \ln \left(\frac{c}{1-c} \right) - \frac{a_{int}}{kT}c \quad (2.21)$$

for different values of a_{int}/kT shows what happens when the strength of the interaction increases. In figure 2.3 a_{int}/kT is set to zero. The chemical potential monotonically increases with concentration. When $a_{int}/kT = 4$ (figure 2.4), the curve is flat at $c = 0.5$. If $a_{int}/kT = 8$ then $y(c)$ has a negative slope in the $c = 0.5$ region (figure 2.5). The significance of this fact is that the pressure-concentration relation (2.20) does not represent equilibrium in this case. The actual equilibrium curve is found using Maxwell's construction [34] (the dotted line in figure 2.5). The physical meaning behind this so-called plateau is that at a given concentration c_α it becomes thermodynamically favorable to start forming regions of concentration c_β , with $c_\alpha + c_\beta = 1$, instead of continuing to increase the concentration homogeneously. The values of c_α and c_β are obtained from the requirement of minimal free energy which leads to an equal area construction:

$$\mu_{solution}(c_\alpha) = \mu_{solution}(c_\beta) = \frac{1}{c_\beta - c_\alpha} \int_{c_\alpha}^{c_\beta} \mu_{solution}(c)dc. \quad (2.22)$$

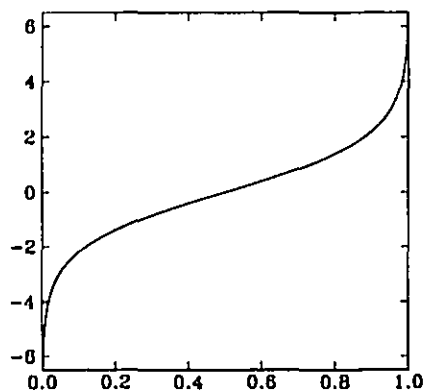
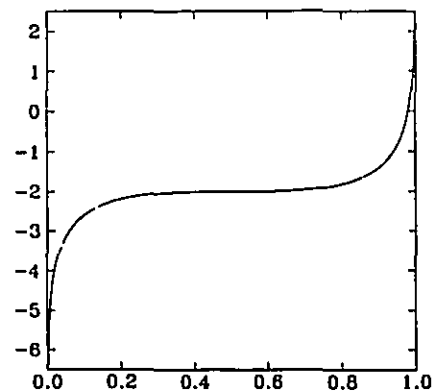
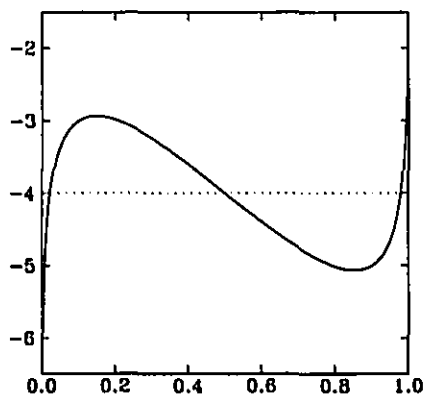
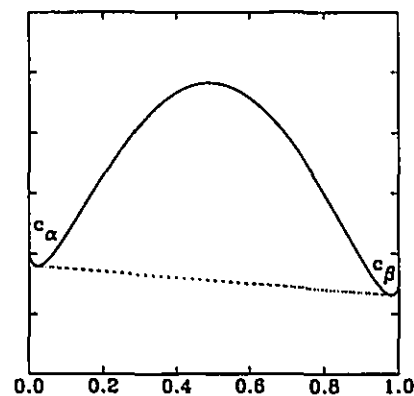
Figure 2.3: $y(c)$ for $a_{int}/kT = 0$.Figure 2.4: $y(c)$ for $a_{int}/kT = 4$.Figure 2.5: $y(c)$ for $a_{int}/kT = 8$.

Figure 2.6: Free energy (schematic).

Equation (2.22) is equivalent to the common tangent rule familiar to physical metallurgists. Figure 2.6 shows a schematic free energy curve where the dotted line is the free energy of the mixture of two phases with concentrations c_{α} and c_{β} .

Physically this phase separation has its origin in the effective interaction between dissolved hydrogen atoms. It has been shown [1] that this interaction mostly stems from the volume expansion caused by the interstitial atoms. Electronic effects also play a role whose importance vary from one system to another.

A high temperature will counteract the interaction and concentration will homogeneously increase with pressure. The critical temperature for equation (2.20) is given

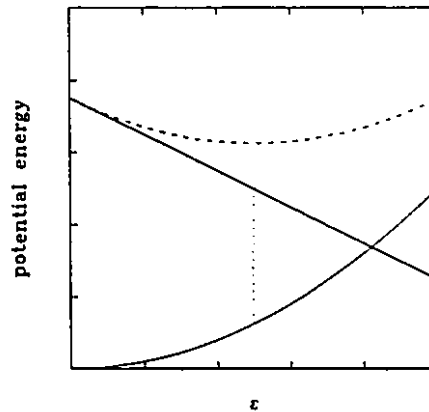


Figure 2.7: Potential energy of the host lattice (parabola), hydrogen-metal potential energy (straight line), and total potential energy (dashed line) as a function of lattice parameter expansion (ϵ). The dotted line shows the expansion at mechanical equilibrium.

by

$$\frac{a_{int}}{kT_c} = 4 \quad (2.23)$$

(see figure 2.4) and the critical concentration is $c_c = 0.5$.

Having discussed the effect of the H-H interaction on the equilibrium properties of metal-hydrogen systems we shall turn our attention to its origin.

2.3 Elastic interaction

A microscopic theory of the elastic interaction has been developed by H. Wagner and H. Horner in 1974 [92]. The approximations used are that hydrogen-metal interactions are described by a linear potential (“Kanzaki forces” [46]) and the harmonic approximation for the elasticity of the metal lattice. We shall review their theory in this section.

2.3.1 Qualitative introduction

When an atom of hydrogen is dissolved in a metal lattice, it exerts forces on the neighbouring atoms. These forces are generally repulsive. If the lattice expands, the potential energy of the hydrogen atom is decreased, while the elastic energy of the lattice is increased. The configuration of the hydrogen-metal system at equilibrium results from the minimization of the sum of these two potentials.

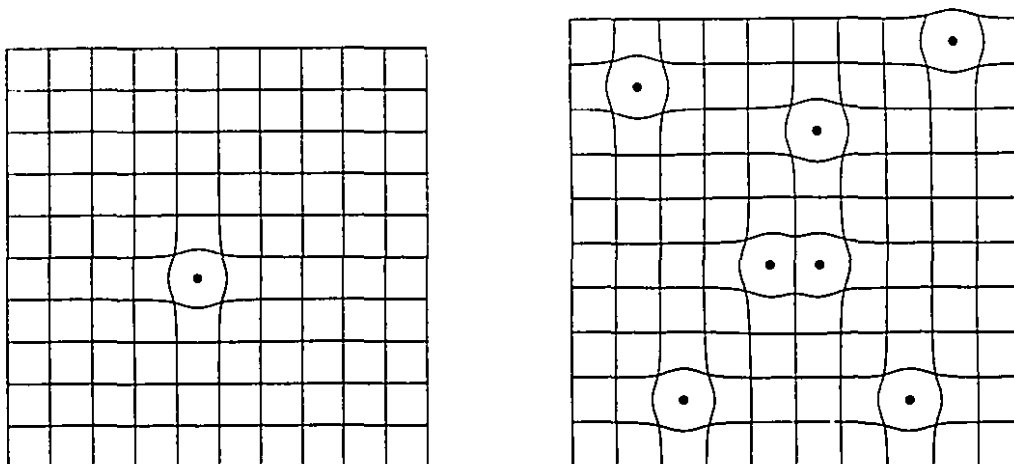


Figure 2.8: Left: illustration of a metal lattice with one hydrogen atom. Right: illustration of a metal lattice with several hydrogen atoms. There is an overall expansion in addition to the local distortion around the hydrogen.

The elastic energy of the lattice is generally described by a potential which is proportional to the square of the displacement of the atoms. This is the so-called harmonic approximation. There is no linear term in the elastic energy because the pure lattice is in a state of mechanical equilibrium. When a hydrogen atom is introduced in the lattice, the atomic positions of the pure lattice no longer represent mechanical equilibrium. The interaction between hydrogen atoms and metal atoms is described in first approximation by a potential which is linear in terms of hydrogen-metal interatomic distances. There will be of course higher order terms, but because the interatomic potential is likely to be a well behaved function and the hydrogen-induced deformations are of the order of a few percents, a linear potential is expected to describe well the physics of metal-hydrogen systems. The resulting potential energy will of course be harmonic, since the metal-hydrogen solution has to follow a harmonic potential near its equilibrium configuration (see figure 2.7).

The deformation induced by a hydrogen atom has two very different contributions. There is the deformation that would occur if the lattice was infinite. It is essentially a shear deformation. The presence of a free surface (the surface of the crystal), induces an expansion which is necessary to release the stress at the surface (see figure 2.8). Mechanical equilibrium is reached only if the surface is stress-free. This deformation

is called the “image” field [29].

As a second hydrogen atom is introduced, it finds itself in an pre-expanded lattice. Since the hydrogen-metal potential is — roughly — linear, the force the hydrogen exerts on the neighbouring atoms is constant. The second hydrogen causes an expansion which is approximately the same as that of the first hydrogen. The potential energy of this second atom, however, will be lower than the potential energy it would have in the absence of the expansion caused by the first atom. A consequence of this is that the potential energy of a crystal with two hydrogen atoms decreases as the two hydrogens get closer, until short-range repulsion becomes important.

The first-order dependence in concentration of the interaction term in the chemical potential (2.20) is easy to understand. The expansion of a lattice caused by an homogeneous distribution of identical dilatation centers is proportional to their number. At the same time, because of the linear hydrogen-metal potential energy, the change in the energy of solution of a hydrogen atom in the metal, thus the change in chemical potential of hydrogen in solution caused by the hydrogen already present, is proportional to the expansion of the lattice. Therefore the variation of the chemical potential with concentration has to be proportional to concentration itself.

This is the physical origin of the effective elastic interaction between hydrogen atoms in a metal lattice. We now turn our attention to the mathematical description of this interaction in order to obtain the necessary quantitative expressions.

2.3.2 *Discrete model*

The position of metal atoms is given by

$$\mathbf{w}_m = \mathbf{u}_m + \mathbf{v}_m \quad (2.24)$$

where \mathbf{u}_m is the rest position in the pure host lattice and \mathbf{v}_m is the displacement. Similarly the position of hydrogen atoms is

$$\mathbf{z}_a = \mathbf{x}_a + \mathbf{y}_a. \quad (2.25)$$

The total potential energy includes that of the host metal $\Phi(w)$, the hydrogen-hydrogen interaction energy $U(z)$, and the interaction energy between the hydrogen

atoms and the lattice $\Psi(w, z)$. To each hydrogen site corresponds an occupation number τ_a .

The potential energy of the pure host is given by

$$\Phi(w) = \Phi(u) + \frac{1}{2} \mathbf{v}_m \cdot \Phi_{mn} \cdot \mathbf{v}_n \quad (2.26)$$

where the linear term vanishes due to the requirement of mechanical equilibrium ($\Phi_{m\mu} = 0$).¹

Assuming a two-body central potential between hydrogen atoms and metal atoms

$$\Psi(z, w, \tau) = \sum_{ma} \psi(|\mathbf{z}_a - \mathbf{w}_m|) \tau_a. \quad (2.27)$$

Expanding in series with respect to the displacements \mathbf{v}_m and \mathbf{y}_a and keeping only zeroth and first order terms one obtains

$$\Psi(z, w, \tau) = \Psi(x, u, \tau) + \Psi_m(x, u, \tau) \cdot \mathbf{v}_m \quad (2.28)$$

where

$$\Psi_{m\mu}(x, u, \tau) = \sum_a \frac{\partial \psi(|\mathbf{x}_a - \mathbf{u}_m|) \tau_a}{\partial u_{m\mu}} \quad (2.29)$$

$$= \Psi_{m\mu a} \tau_a \quad (2.30)$$

There is no term in $y_{a\nu}$ because the force on each hydrogen vanishes at rest ($\Psi_{a\nu}(x, u) = 0$). In the first term on the right side of equation (2.28), τ is the only variable since x and u are determined by the pure host lattice. We may write

$$\Psi(x, u, \tau) = \Psi(\tau). \quad (2.31)$$

The hydrogen-hydrogen electronic interaction is replaced by a hard-core repulsion:

$$U(x, \tau) = \frac{1}{2} \sum_{ab} U_{ab} \tau_a \tau_b = U(\tau), \quad (2.32)$$

with

$$U_{ab} = \infty \text{ for } |\mathbf{x}_a - \mathbf{x}_b| < R \quad (2.33)$$

$$= 0 \text{ for } |\mathbf{x}_a - \mathbf{x}_b| > R \quad (2.34)$$

¹Greek indices designate coordinate axes. There is a summation over repeated indices unless specified otherwise.

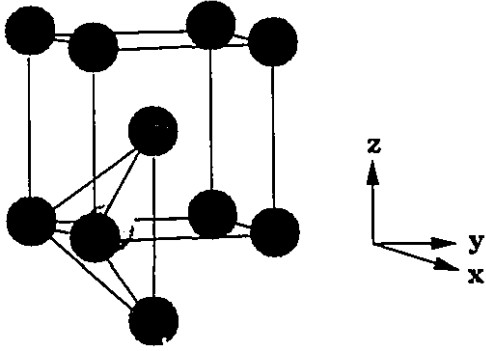


Figure 2.9: Tetrahedral site in bcc niobium.

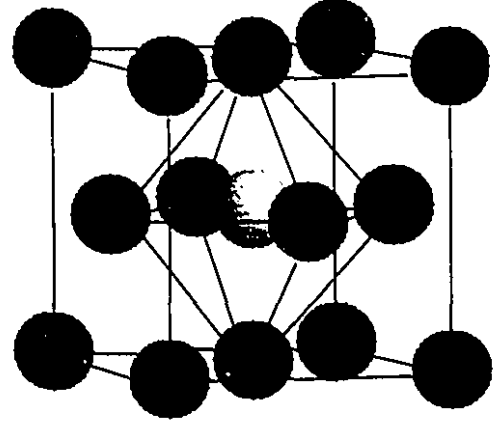


Figure 2.10: Octahedral site in fcc palladium.

where R is chosen to be representative of the closest distance between hydrogen atoms in the hydride phase being studied. The metal-hydrogen Hamiltonian is now:

$$H_{tot} = \Phi + \frac{1}{2} \mathbf{v}_m \cdot \Phi_{mn} \cdot \mathbf{v}_n + U(\tau) + \Psi(\tau) + \Psi_m(\tau) \cdot \mathbf{v}_m. \quad (2.35)$$

The displacement of metal atoms consists of an elastic part due to strains caused by interstitial hydrogen and a thermal vibration:

$$\mathbf{v}_m = \mathbf{v}_{el,m} + \mathbf{v}_{vib,m}. \quad (2.36)$$

The requirement of time-averaged mechanical equilibrium $\overline{\mathbf{v}_{vib,m}} = 0$ leads to

$$\Phi_{mn} \cdot \mathbf{v}_{el,n} = -\Psi_m(\tau) = -\Psi_{ma} \tau_a \quad (2.37)$$

or

$$\mathbf{v}_{el,m}(\tau) = \mathbf{D}_{mn} \cdot \Psi_n(\tau) \quad (2.38)$$

where \mathbf{D}_{mn} is the inverse of the matrix Φ_{mn} . The force that the hydrogen atoms exert on a metal atom is balanced by the elastic forces of the surrounding metal atoms.

2.3.3 Continuum model

The elastic Hamiltonian

$$H_{elastic} = \mathbf{v}_m \cdot \Psi_{ma} \tau_a + \frac{1}{2} \mathbf{v}_m \cdot \Phi_{mn} \cdot \mathbf{v}_n \quad (2.39)$$

and the equation

$$\Phi_{mn} \cdot \mathbf{v}_n = -\Psi_{ma} \tau_a \quad (2.40)$$

have a continuous version. The reader shall find the conversion from discrete to continuous variables in reference [92].

The elastic constants

$$C_{\alpha\beta\mu\nu} = \frac{1}{V} u_{m\alpha} \Phi_{m\beta\nu\mu} u_{n\mu} \quad (2.41)$$

in harmonic approximation and the strain field

$$\epsilon_{\mu\nu}(\mathbf{r}) = \frac{1}{2} \left(\frac{\partial v_\nu(\mathbf{r})}{\partial r_\mu} + \frac{\partial v_\mu(\mathbf{r})}{\partial r_\nu} \right) \quad (2.42)$$

are used together with the density of the force-dipole tensor

$$\Pi_{\alpha\beta}(\mathbf{r}) = \sum_j \rho_j(\mathbf{r}) P_{\alpha\beta j} \quad (2.43)$$

where

$$P_{\alpha\beta j} = \sum_m (x_{m\alpha} - u_{a\alpha}) \Psi_{m\beta a} \quad (2.44)$$

(no summation over a) depends on the symmetry of the lattice and ρ_j is the partial density of hydrogen on sites of type j . The index j designates the axis of symmetry of the different sites.

From the symmetry of the lattice and considering neighboring atoms only we find

$$P_{\alpha\beta j} = P' \delta_{\alpha\beta} + (P - P') \delta_{\alpha j} \delta_{\beta j} \quad (2.45)$$

(no sum over index j) for bcc tetrahedral sites. For example the site $j = 2$ (y-site) shown in figure 2.9 will have $P_{11} = P'$, $P_{22} = P$, and $P_{33} = P'$ with all the other components equal to zero. In the case of fcc octahedral sites (figure 2.10) $P = P'$ and

$$P_{\alpha\beta j} = P \delta_{\alpha\beta}. \quad (2.46)$$

In the continuum model (2.39) becomes

$$H_{elastic} = \frac{1}{2} \int \epsilon_{\alpha\beta}(\mathbf{r}) C_{\alpha\beta\mu\nu} \epsilon_{\mu\nu}(\mathbf{r}) d^3\mathbf{r} + \int \Pi_{\alpha\beta}(\mathbf{r}) \epsilon_{\alpha\beta}(\mathbf{r}) d^3\mathbf{r} \quad (2.47)$$

while (2.40) is turned into

$$C_{\alpha\beta\mu\nu} \frac{\partial \epsilon_{\mu\nu}(\mathbf{r})}{\partial r_\beta} = -\frac{\partial \Pi_{\alpha\beta}(\mathbf{r})}{\partial r_\beta} \quad (2.48)$$

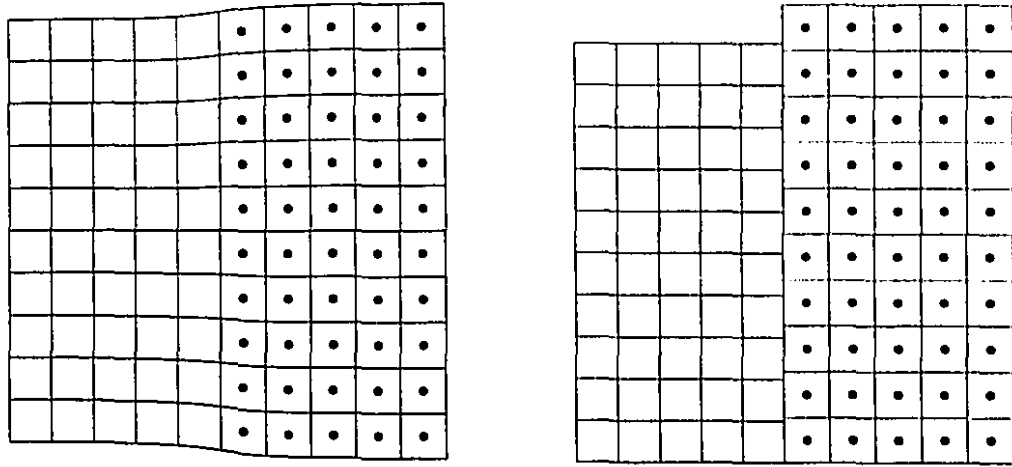


Figure 2.11: Left: illustration of a coherent interface. Right: illustration of an incoherent interface.

inside the crystal. We also have the following boundary condition on the surface:

$$C_{\alpha\beta\mu\nu}\hat{n}_\beta(\mathbf{r})\epsilon_{\mu\nu}(\mathbf{r}) = -\hat{n}_\beta(\mathbf{r})\Pi_{\alpha\beta}(\mathbf{r}) \quad (2.49)$$

($\hat{n}(\mathbf{r})$ is a unit vector pointing outward).

The density of the force-dipole tensor is the stress caused by the hydrogen dissolved. It has the units of pressure. The force-dipole itself ($P_{\alpha\beta}$) is the induced stress per unit of hydrogen density. The right-hand terms of (2.47) are the elastic energy of the pure lattice and the decrease in hydrogen-metal potential energy caused by the relaxation (expansion) of the lattice. Equations (2.48) and (2.49) are the usual equations of mechanical equilibrium of elasticity theory in the presence of the stress $\Pi_{\alpha\beta}(\mathbf{r})$. Equations (2.47), (2.48), and (2.49) are valid in the absence of external forces.

2.3.4 Coherency

An important question that arise when discussing metal-hydrogen systems is how the expansion of the lattice can be accommodated. The expansion caused by the hydrogen atoms creates stress that can exceed the elastic limit of the material. Plastic work is done during the formation and decomposition of hydrides. This plastic work will cause the hysteresis found in pressure-composition isotherms.

Figure 2.11 shows the difference between a coherent interface between the pure

metal and the hydride phase and an incoherent interface. In the incoherent crystal, the strain field suffers a discontinuity at the interface between the two phases. Wagner and Horner [92] have discussed in detail coherent density modes (hydrogen density variations which do not create incoherent interfaces). However these modes are only found in samples prepared in special conditions [101, 102]. Samples can generally be considered incoherent; the stress is released by creating dislocations and cracks. In the case of polycrystalline samples where an equilibrium between crystallites with different hydrogen concentrations should involve much less interfacial energy than density modes inside a crystal, the absence of coherency stresses is even more expected.

2.3.5 Lattice expansion

In light of these facts the stress tensor

$$\sigma_{\alpha\beta}(\mathbf{r}) = \Pi_{\alpha\beta}(\mathbf{r}) + C_{\alpha\beta\mu\nu}c_{\mu\nu}(\mathbf{r}) \quad (2.50)$$

(see equation (2.47)) is set to zero, therefore

$$\Pi_{\alpha\beta}(\mathbf{r}) = -C_{\alpha\beta\mu\nu}c_{\mu\nu}(\mathbf{r}) \quad (2.51)$$

or

$$c_{\mu\nu}(\mathbf{r}) = -S_{\mu\nu\alpha\beta}\Pi_{\alpha\beta}(\mathbf{r}) \quad (2.52)$$

$$= -S_{\mu\nu\alpha\beta} \sum_j \rho_j(\mathbf{r}) P_{\alpha\beta j}. \quad (2.53)$$

The components $S_{\mu\nu\alpha\beta}$ are the elastic moduli

$$S_{\mu\nu\alpha\beta}C_{\alpha\beta\kappa\lambda} = \frac{1}{2}(\delta_{\mu\kappa}\delta_{\nu\lambda} + \delta_{\mu\lambda}\delta_{\nu\kappa}) \quad (2.54)$$

and $\rho_j(\mathbf{r})$ the partial density of j sites. Equation (2.53) can be used to calculate the components of the force-dipole tensor from experimental values of the lattice parameters and hydrogen densities. For example the volume expansion of cubic crystals with constant hydrogen density is:

$$\Delta V = \epsilon_{\mu\mu}V \quad (2.55)$$

$$= -S_{\mu\mu\alpha\beta} \sum_j [N_j P_{\alpha\beta j}] \quad (2.56)$$

$$= -S_{\mu\mu\alpha\beta} \sum_j N_j [P' \delta_{\alpha\beta} + (P - P') \delta_{\alpha j} \delta_{\beta j}] \quad (2.57)$$

$$= -S_{\mu\mu\alpha\alpha} P' N - (P - P') \sum_j S_{\mu\mu j j} N_j, \quad (2.58)$$

where N_j is the number of hydrogen atoms on j sites and N is the total number of hydrogen atoms dissolved. $S_{\mu\mu\alpha} = K$ is the compressibility of the pure metal and $S_{\mu\mu jj} = K/3$ (with no sum over j) for cubic crystals. We finally obtain

$$\Delta V = -\frac{1}{3}K(P + 2P')N. \quad (2.59)$$

2.3.6 Elastic energy

Equation (2.51) can be used to simplify (2.47):

$$H_{elastic} = \frac{1}{2} \int \epsilon_{\alpha\beta}(\mathbf{r}) C_{\alpha\beta\mu\nu} \epsilon_{\mu\nu}(\mathbf{r}) d^3\mathbf{r} + \int \Pi_{\alpha\beta}(\mathbf{r}) \epsilon_{\alpha\beta}(\mathbf{r}) d^3\mathbf{r} \quad (2.60)$$

$$= -\frac{1}{2} \int \epsilon_{\alpha\beta}(\mathbf{r}) \Pi_{\alpha\beta}(\mathbf{r}) d^3\mathbf{r} + \int \Pi_{\alpha\beta}(\mathbf{r}) \epsilon_{\alpha\beta}(\mathbf{r}) d^3\mathbf{r} \quad (2.61)$$

$$= \frac{1}{2} \int \Pi_{\alpha\beta}(\mathbf{r}) \epsilon_{\alpha\beta}(\mathbf{r}) d^3\mathbf{r}. \quad (2.62)$$

Using (2.52):

$$H_{elastic} = -\frac{1}{2} \int \Pi_{\alpha\beta}(\mathbf{r}) S_{\alpha\beta\mu\nu} \Pi_{\mu\nu}(\mathbf{r}) d^3\mathbf{r} \quad (2.63)$$

$$= -\frac{1}{2} \int \sum_j \rho_j(\mathbf{r}) [P' \delta_{\alpha\beta} + (P - P') \delta_{\alpha j \beta j}] S_{\alpha\beta\mu\nu} \sum_i \rho_i(\mathbf{r}) [P' \delta_{\mu\nu} + (P - P') \delta_{\mu i \nu i}] d^3\mathbf{r} \quad (2.64)$$

$$= -\frac{1}{2} \int \sum_{ji} \rho_j(\mathbf{r}) \rho_i(\mathbf{r}) [P'^2 S_{\alpha\alpha\mu\mu} + P'(P - P')(S_{\alpha\alpha ii} + S_{jj\mu\mu}) + (P - P')^2 S_{jj\mu\mu}] d^3\mathbf{r}. \quad (2.65)$$

In the case where $\rho_j(\mathbf{r}) = \rho/3$, equation (2.65) simply becomes:

$$H_{elastic} = -\frac{1}{2} \left[\frac{P + 2P'}{3} \right]^2 \frac{KN^2}{V}. \quad (2.66)$$

Taking $H_{elastic}$ into account in calculating the chemical potential of the hydrogen-metal solution we introduce a correction

$$\Delta\mu_{elastic} = - \left[\frac{P + 2P'}{3} \right]^2 \frac{KN}{V} \quad (2.67)$$

$$= - \left[\frac{P + 2P'}{3} \right]^2 \frac{K}{v_M} \frac{N_H}{N_L} c \quad (2.68)$$

$$(2.69)$$

where v_M is the specific volume of the metal, N_L is number of metal atoms, and N_H is the number of hydrogen storage sites. In terms of equation (2.20) this translates into

$$a_{int,elastic} = \left[\frac{P + 2P'}{3} \right]^2 \frac{K}{v_M} \frac{N_H}{N_L}. \quad (2.70)$$

2.3.7 Validity of the Wagner-Horner theory

The theory described above has been tried in the calculation of the Nb-H phase diagram [42]. The results are surprisingly good: the calculated critical temperature falls between the values measured by different investigators. The critical concentration however is not as close to experimental values (0.4 hydrogen atom/metal atom instead of the experimental values centered around 0.3). These results support the hypothesis that elastic forces are responsible for the phase separation in metal hydrides. A more precise treatment of short-range H-H interactions is needed in order to obtain better agreement with experimental data. In particular, the use of a hard-core repulsion is expected to introduce large errors. This theory will be used in the analysis of our experiments on nanocrystalline Fe-Ti.

2.4 Hydrogen in amorphous alloys

Hydrogen is absorbed not only in crystalline materials but also in amorphous alloys [109]. The most important difference between the two is that no phase separation between low and high density regions has yet been found in any amorphous hydride. This is shown by the absence of a plateau in pressure-composition isotherms of these materials. The isotherms of crystalline and amorphous $Ni_{50}Zr_{50}$ are shown in figure 2.12. Structural disorder has an effect similar to thermal disorder in preventing phase separation. High temperatures inhibit phase separation when the thermal motion of hydrogen atoms is such that they cannot stay confined in condensed hydride regions. In the case of amorphous alloys, the energy difference between the different sites is so high that hydrogen atoms go into deep storage sites which are homogeneously dispersed in the amorphous matrix and therefore can only form homogeneous phases. While in crystalline materials the pressure-composition isotherm is the result of a balance between configurational entropy and the effective H-H in-

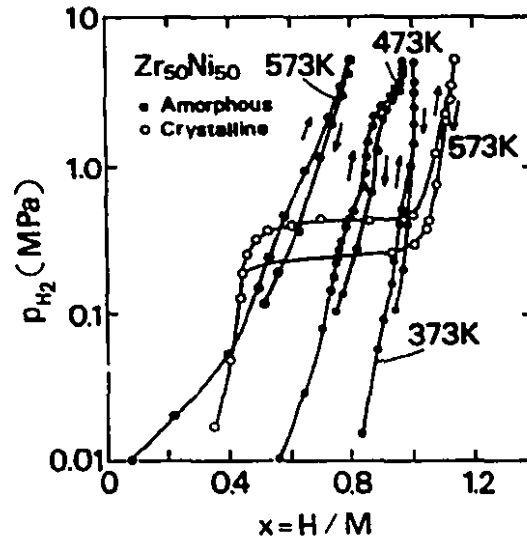


Figure 2.12: Pressure-concentration isotherms of crystalline and amorphous $\text{Ni}_{50}\text{Zr}_{50}$ (taken from [4]).

teraction, in amorphous alloys the spread in energy of the different storage sites is usually much larger than kT and the isotherm roughly corresponds to the internal energy. Though there is no theoretical reason to prevent an amorphous material from exhibiting phase separation, none has been found with such a behavior. The structural disorder is probably too important in any amorphous alloy to allow phase separation. Recent experiments have shown that the plateau can even be suppressed in un-relaxed nanocrystalline FeTi [108].

The storage sites can no longer be described by well defined energies and a simple concentration

$$c = \frac{1}{N_H} \sum_j N_j. \quad (2.71)$$

There is now an energy distribution $D(E)$ (number of sites per energy unit) and a partial concentration $x(E)$, the proportion of occupied sites of energy E . The total number of sites is

$$N_H = \int_{-\infty}^{+\infty} D(E) dE \quad (2.72)$$

and the total concentration

$$c = \frac{1}{N_H} \int_{-\infty}^{+\infty} D(E) f(E) dE. \quad (2.73)$$

The partial concentration is given by the Fermi-Dirac distribution:

$$x(E) = \frac{1}{e^{(E-\mu)/kT} + 1}. \quad (2.74)$$

The chemical potential is obtained from the integral (2.73).

If we consider a square distribution

$$D(E) = \begin{cases} \frac{N_H}{2\Delta} & \text{for } -\Delta < E - E_0 < \Delta \\ 0 & \text{otherwise,} \end{cases} \quad (2.75)$$

we find

$$c = \frac{kT}{2\Delta} \ln \left[\frac{e^{-(E_0-\Delta-\mu)/kT} + 1}{e^{-(E_0+\Delta-\mu)/kT} + 1} \right]. \quad (2.76)$$

Isolating μ in (2.76) yields

$$\mu = E_0 - \Delta + kT \ln \left[\frac{e^{2\Delta c/kT} - 1}{1 - e^{2\Delta(c-1)/kT}} \right]. \quad (2.77)$$

If we include an interaction term the chemical potential becomes

$$\mu = E_0 - \Delta - a_{int}c + kT \ln \left[\frac{e^{2\Delta c/kT} - 1}{1 - e^{2\Delta(c-1)/kT}} \right]. \quad (2.78)$$

A positive critical temperature is found if

$$a_{int} > 2\Delta. \quad (2.79)$$

The details of the calculations are found in the work by Griessen [40]. More generally, for symmetric distributions with a single peak at E_0 , the criterion for having a plateau is

$$a_{int} > \frac{1}{D(E_0)}. \quad (2.80)$$

Amorphous alloys are, of course, more complex. They can be modeled in the following way [41, 18]. It is assumed that storage sites are tetrahedral. In binary alloys this means that five types of site are found: A_xB_{4-x} with $x = 0, 1, 2, 3, 4$. The justification for using tetrahedral sites comes from scattering experiments [81, 45] which provide evidence that hydrogen atoms stored in amorphous alloys are surrounded by four nearest-neighbours. The energy of a site is expected to vary as a function of x . The energy distribution is modeled as a sum of Gaussians centered around each site

energy E_x . The distribution can be determined by performing precise measurements of the concentration as a function of chemical potential. This is usually done by electrochemical charging of electrodes made of the material studied [41]. Experiments seem to support the model [109].

2.5 *Properties of real metal-hydrogen systems*

Materials studied in the laboratory differ from the ideal behavior described in the preceding sections. The first difference encountered is the influence of the surface. The surface of metals is generally oxidized. This oxide layer is an effective barrier against the movement of hydrogen atoms [74]. An initial activation treatment, consisting of repeated exposure to high temperatures and hydrogen pressures, is generally required, especially in the case of hydrides of intermetallic compounds [73]. Different mechanisms have been observed to operate during activation. In one of them, the rather uniform oxide layer breaks into more stable oxide clusters, leaving some of the surface free for hydrogen diffusion.

During the activation procedure, the hydride phase is formed, partially at first, completely at the end of the procedure. The initial hydride formation causes extensive cracking and decrepitation of the material. This is presumably due to the large volume expansion ($\sim 10\%$) induced by the interstitial hydrogen during the formation of the hydride phase. Amorphous alloys, in which the hydrogen concentration is always homogeneous, also expand but do not decrepitate.

Another non-equilibrium feature that remains even in fully activated samples is hysteresis. The growth of the hydride phase inside the metallic phase involves interfacial stress and, as a consequence, plastic work. Hysteresis causes formation pressures to be higher than decomposition pressures. This effect is detrimental to practical applications.

Some researchers tend to consider decomposition isotherms as those representing equilibrium. However theoretical [32, 33] and experimental [87] evidence suggests that equilibrium lies halfway, in terms of chemical potential, between formation and decomposition isotherms.

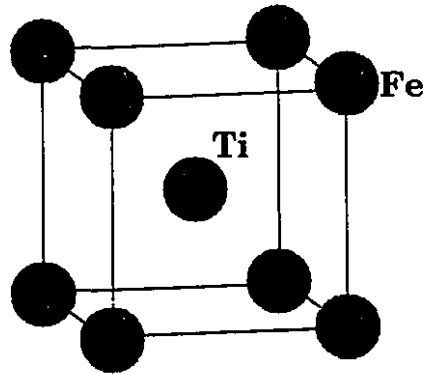


Figure 2.13: FeTi.

The work done during a complete hysteresis cycle is given by:

$$W = N_L(c_\beta - c_\alpha) \frac{1}{2} kT \ln \left(\frac{P_F}{P_D} \right). \quad (2.81)$$

The extent of hysteresis widely varies. In the case of Nb-H, it is 3.7kJ/mol H [53].

2.6 Iron-titanium

2.6.1 The iron-titanium binary system

The Fe(Z=26)-Ti(Z=22) binary system has two stable compounds: FeTi and Fe₂Ti. Fe₂Ti has the MgZn₂-type Laves structure (space group $P6_3/mmc$) while FeTi has a simple cubic ($Pm3m$) structure (figure 2.13) where iron is located at the corners of the unit cell and titanium is at the center (or vice versa). The phase diagram [95] (figure 2.14) also reveals an extended bcc solid solution β -Ti at relatively high temperatures (>850K).

The free energies of the different phases in the Fe-Ti system and the phase diagram have been calculated using the CALPHAD method [97, 95] (figure 2.15). The CALPHAD method is basically a fit of the available thermodynamic data concerning a particular intermetallic system to a function which describes the free energy. This function contains terms involving the concentration of each element and the temperature. Certain assumptions are made as to which terms are to be included, depending on the particular system and the conclusions which can be made from the thermodynamic data. Once a best fit is obtained for the coefficients of these terms, one can calculate the free energies of the various phases for different compositions and

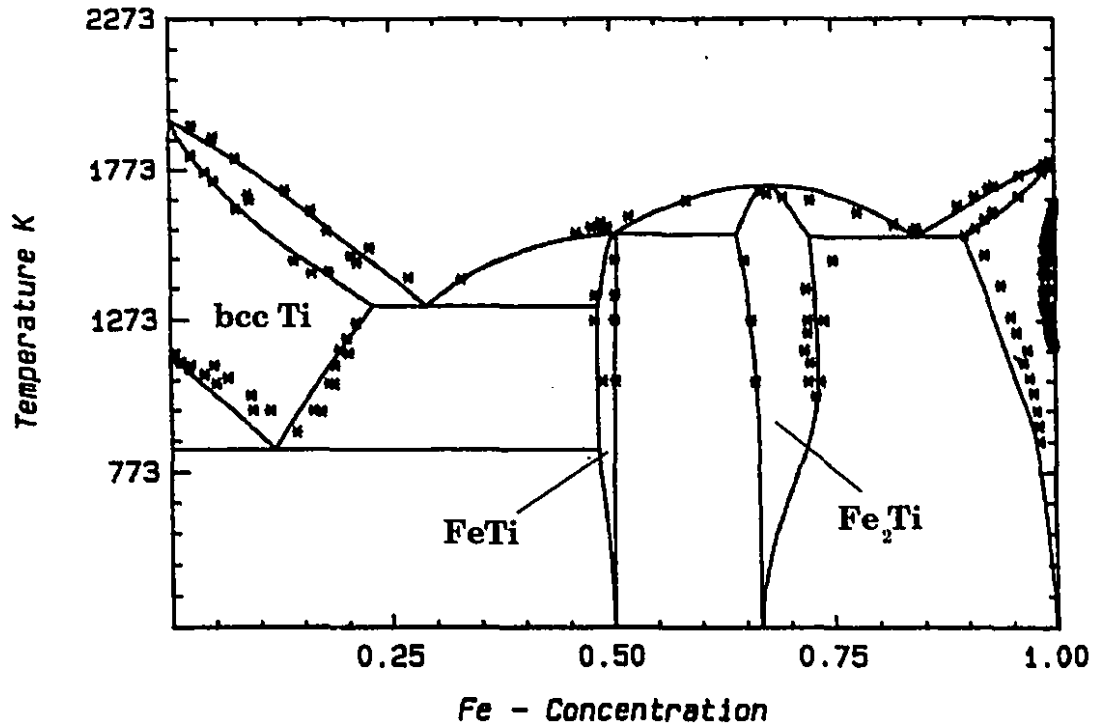


Figure 2.14: Phase diagram of Fe-Ti [95]. The stars are experimental points and the lines are calculated by the CALPHAD method.

temperatures, and establish a phase diagram. The CALPHAD method is described in more detail in chapter 4. Of particular interest is the free energy of the amorphous phase which exhibits a phase separation. These free energy curves shall prove useful in the analysis of the ball milling process applied to iron-titanium.

2.6.2 Hydrogen storage in Fe-Ti

Reilly and Wiswall [70] discovered in 1974 the remarkable hydrogen storage properties of iron-titanium. The compound Fe₂Ti does not absorb hydrogen. On the other hand FeTi does absorb hydrogen in large amounts, up to approximately one hydrogen atom per metal atom.

Samples have to be prepared carefully. Iron and titanium form very stable oxides, samples must therefore be kept in an inert atmosphere or under vacuum. They must also be subjected to an activation procedure in order to absorb hydrogen. The activation cycle used by Reilly and Wiswall consists of an exposure to a moderate hydrogen pressure (~7 atmospheres) at 400°C for 30 minutes followed by cooling in

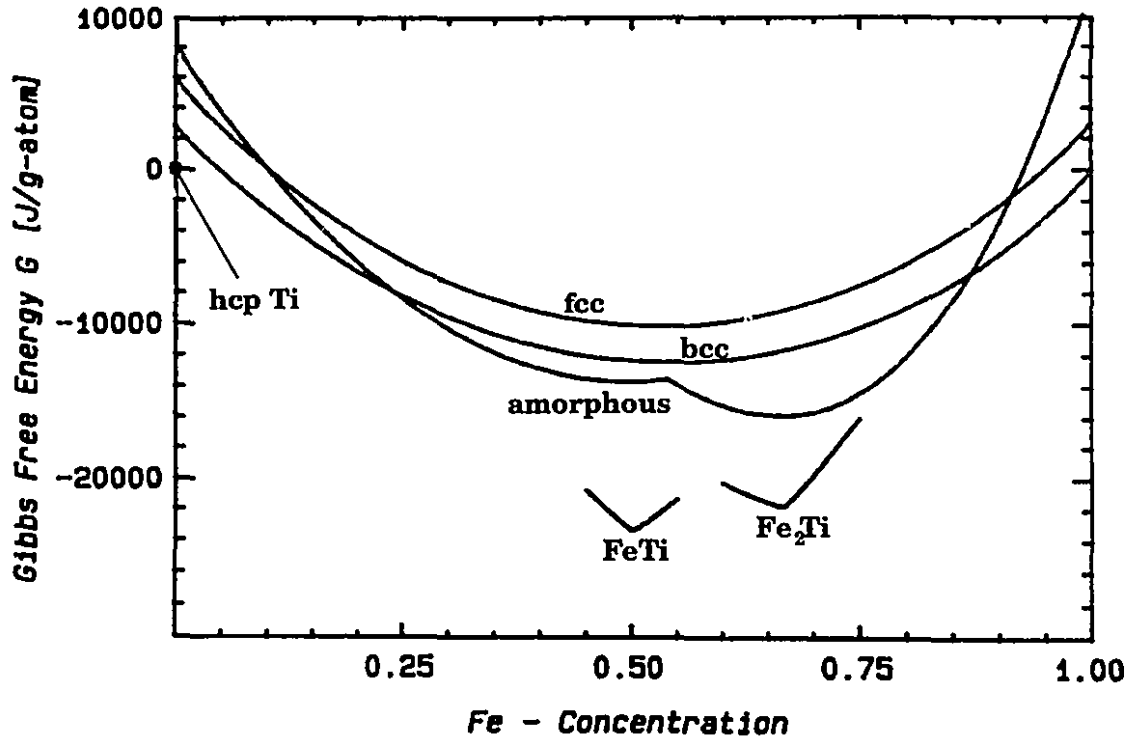


Figure 2.15: Free energies of Fe-Ti phases at 300°C [95].

vacuum after which a high pressure (~ 65 atmospheres) of hydrogen is applied to the sample. This cycle has to be repeated in order to have a reproducible absorption of the maximum amount of hydrogen. Exposure to air of a previously activated sample renders it inactive. The chemical reactions involved in the activation process are the subject of intense research activity [74, 89].

The pressure-composition isotherm of polycrystalline FeTi-H is shown in figure 2.16 for a temperature of 40°C. There is an initial solubility in FeTi. This solid solution is called the α phase. At around 15 atmospheres there is a plateau indicating the formation of a new phase (β phase) of approximate composition FeTiH. Further increase of the pressure leads to the formation of the γ phase with approximately one hydrogen atom per metal atom. The isotherm exhibits a typical hysteresis. However the fact that the absorption plateau extends to a much higher composition than the desorption plateau is unusual. It has been found that two phases exist in this range of composition: the β_1 -FeTiH_{0.94} phase formed by desorption and β_2 -FeTiH_{1.40} formed during absorption [72]. Their structures are similar, only the occupation of H sites

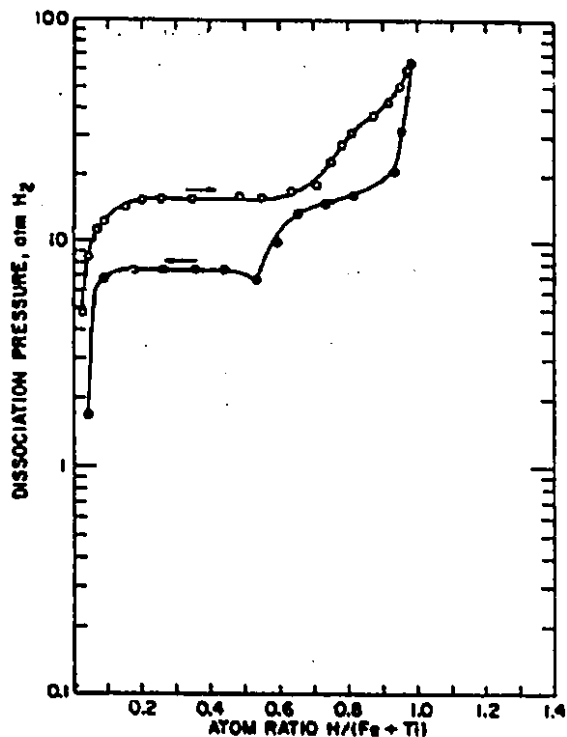


Figure 2.16: Pressure-composition isotherm of FeTi-H at 40°C (taken from [70]).

and their lattice parameters differ. A curious dip is found in the desorption curve. More work remains to be done for a satisfactory explanation of this phenomenon. The phase diagram of the FeTi-H system is given below (figure 2.17).

2.6.3 Structure of iron-titanium hydrides

Because hydrogen scatters X-rays very weakly, this method of diffraction gives only lattice parameters, so that atomic positions must be determined using neutron diffraction. Structural studies were performed on deuterides because the scattering length of deuterium is different from both iron and titanium, making the measurement more sensitive to the position of deuterium compared to hydrogen, in addition there is no significant inelastic scattering for deuterons. It was found however that hydrides and deuterides of iron-titanium are iso-structural [69]. The lattice parameters and phase compositions obtained from X-ray experiments [69] (see table 2.1) will be used in conjunction with atomic positions given by neutron diffraction.

Deuterium occupies octahedral sites with two iron atoms as nearest-neighbors. In

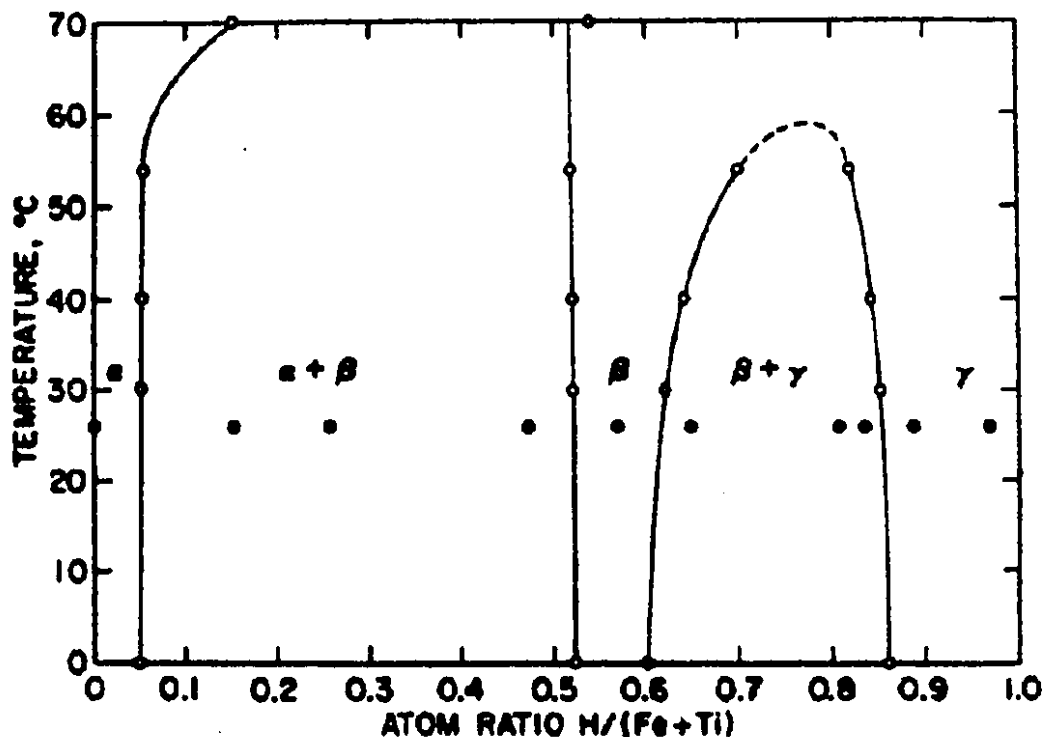


Figure 2.17: Phase diagram of FeTi-H (taken from [70]).

the α phase these sites are occupied randomly [85] (see figure 2.18 and table 2.2). In the β_1 phase occupied sites form chains and the cubic symmetry is lost. Figure 2.19 shows the new orthorhombic structure [84, 30, 91]. The lattice parameter c corresponds to that of the initial α cell but is expanded. The distorted initial α cell is also shown. A second set of sites (0.5,0.25,0.25) is present. Few of these H2 sites are occupied —12%—, while 88% of the H1 sites are. The β_2 phase has the same crystal structure but the occupancy of H1 and H2 sites becomes 0.92 and 0.45 respectively. The transformation to the γ phase involves further loss of symmetry. Sites with two titanium atoms as nearest-neighbors are also occupied (see table 2.4 and figure 2.20). These H4 sites have an occupancy of 85%. They form a network of octahedra with the (2Fe,4Ti) sites [86].

Table 2.1: Structure of FeTi hydrides.

phase	space group	lattice parameters Å
α -FeTiH _{0.06}	Pm3m	a=2.9792
β_1 -FeTiH _{0.94}	P222 ₁	a=2.954 b=4.538 c=4.381
β_2 -FeTiH _{1.40}	P222 ₁	a=3.094 b=4.513 c=4.391
γ -FeTiH _{1.90}	P2/m	a=4.713 b=2.834 c=4.713 $\beta=97.1^\circ$

Table 2.2: Atomic positions in α -FeTiH_{0.06}.

site	x	y	z
Ti	0	0	0
Fe	0.5	0.5	0.5
H	0	0	0.5

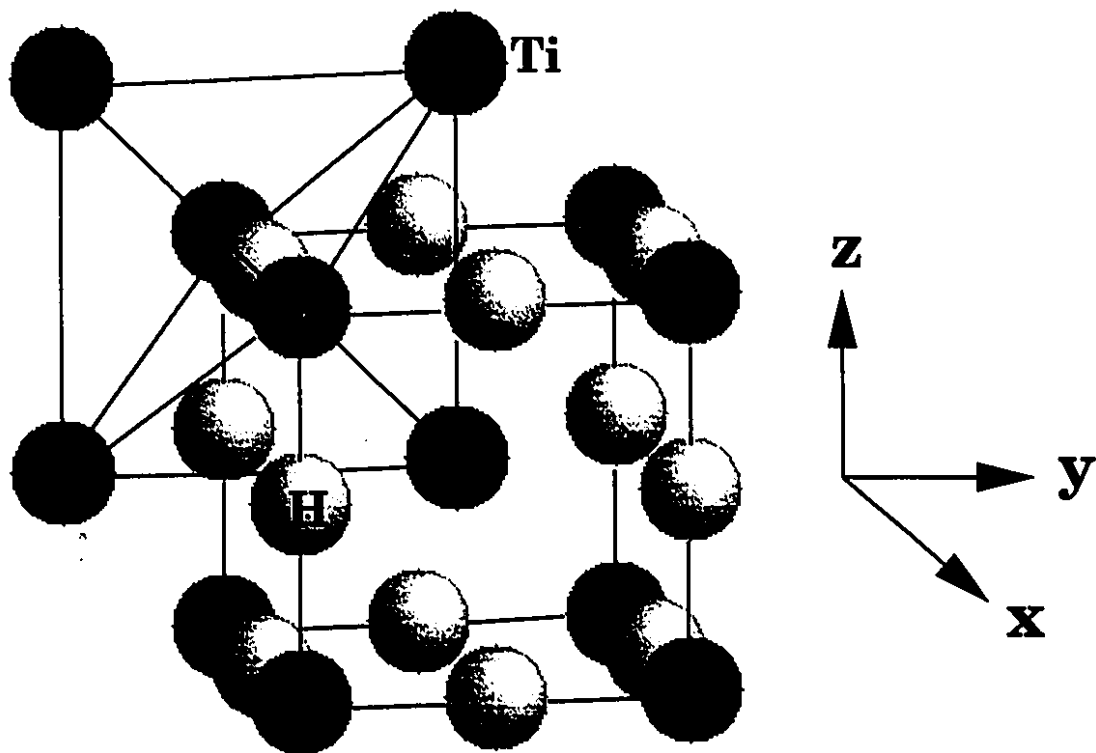
Figure 2.18: α -FeTiH_{0.06}.

Table 2.3: Atomic positions in β_1 -FeTiH_{0.94} and β_2 -FeTiH_{1.40}.

site	x	y	z
Ti	0.5	0.25	0.75
Fe	0	0.211	0.25
H1	0	0.5	0
H2	0.5	0.25	0.25

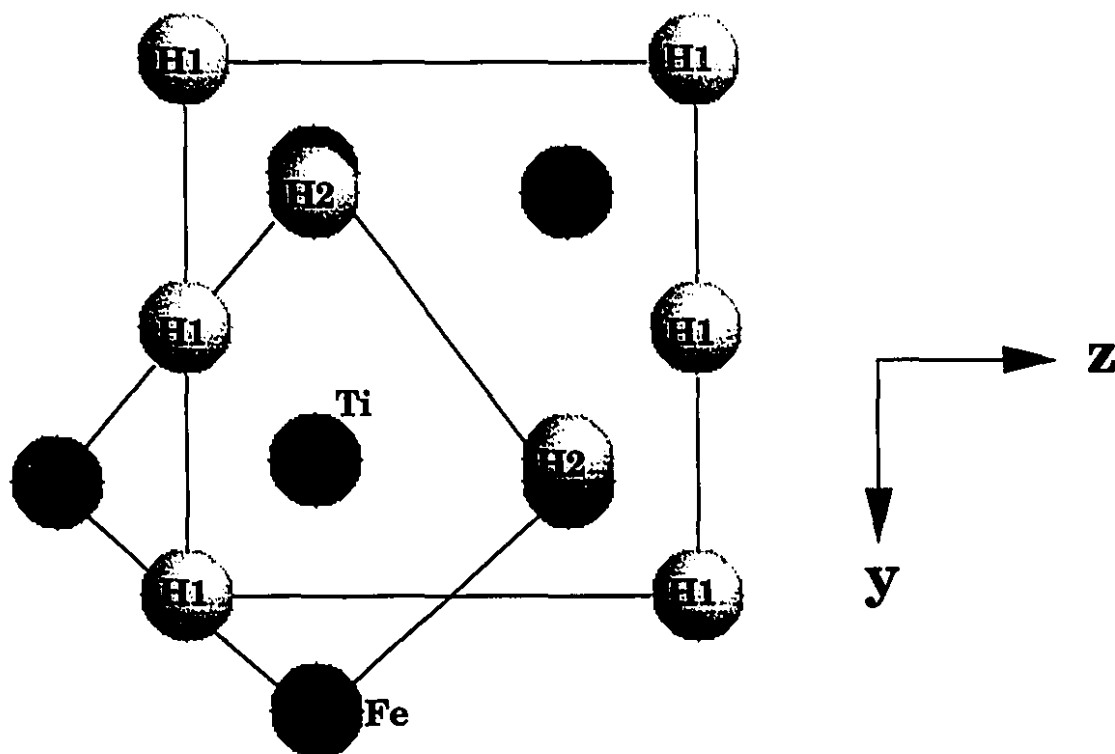
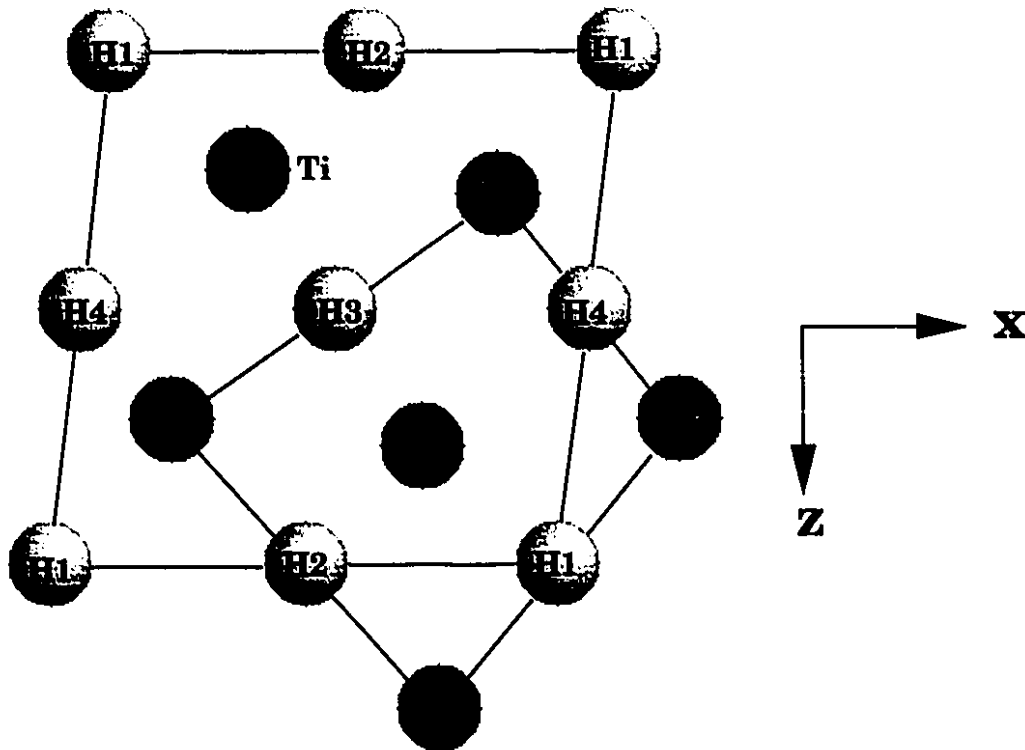
Figure 2.19: β_1 -FeTiH_{0.94} in the y - z plane (large cell: unit cell, small cell: FeTi distorted cell, Ti atoms and H2 sites are above the plane of the paper).

Table 2.4: Atomic positions in γ -FeTiH_{1.90}.

site	x	y	z
Ti	0.294	0.5	0.229
Fe	0.203	0	0.721
H1	0	0	0
H2	0.5	0	0
H3	0.5	0	0.5
H4	0	0.5	0.5

Figure 2.20: γ -FeTiH_{1.90} in the x-z plane (large cell: unit cell, small cell: FeTi distorted cell, Ti atoms and H4 sites are above the plane of the paper).

NANOPHASE MATERIALS

3.1 Overview

The generally accepted definition of nanophase materials is that the domain size of structures (crystals, compositional modulations) is of the order of a few nanometers (10^{-9} meter). The interfaces between these domains become a component as important as the domains themselves in these materials.

The present interest in nanophase materials follows the work by H. Gleiter [9] on grain boundaries and his suggestion to make polycrystalline materials with very small crystals, the increased volume fraction of atoms located at or near grain boundaries being expected to provide larger signals in experiments on these materials, for example, a stronger X-ray background from grain boundaries in diffraction experiments, or a more easily observed heat release in DSC scans during the relaxation of these boundaries.

The initial motivation of studying the structure of grain boundaries has largely given way to the technological potential offered by the novel properties of these materials. Diffusion can be greatly enhanced by the reduction of the crystallite size [43]. Mechanical properties are improved in certain cases [47].

From the point of view of materials science the thermodynamic properties of nanophase materials are especially interesting with regard to the changes in the stability of phases when synthesized in nanocrystalline form. Phases existing normally at high temperature or high pressure can exist at ambient conditions in the nanocrystalline form [82].

A very interesting example of a change in stability is the dependence of the melting temperature of metals on crystallite size [13, 14]. For example the melting tempera-

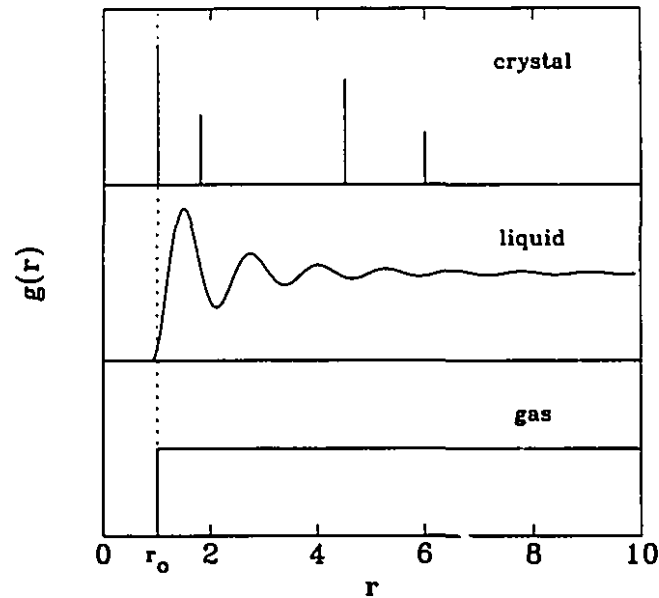


Figure 3.1: Schematic graph of the radial distribution function $g(r)$ for the three states of matter as a function of interatomic distance (in units of the atomic radius r_0).

ture of gold clusters of radius 1 nm is only half of the melting temperature of bulk gold [14]. To this effect investigators are studying the differences in atomic vibrations between coarse-grained polycrystalline metals and nanocrystalline metals [100, 78]. This could be very important in nanocrystalline metal hydrides since a large change in critical temperature may eliminate the plateau in the temperature range which may be useful for applications.

3.2 Grain boundaries

As mentioned above, the important difference between nanocrystalline materials and coarse-grained polycrystalline materials is the presence of a large number of grain boundaries.

In early work [9] it was claimed that while individual grain boundaries can exhibit periodicity, the ensemble of grain boundaries in a material may lack any sort of long-range or even short-range order [9]. Because interatomic distances in a crystal are determined for all distances up to infinity (long-range order), their radial distribution

function consists of sharp peaks (delta functions in ideal crystals). In liquids and amorphous alloys, interatomic distances are found around broad maxima at short distances, and become flat at large distances; they are said to exhibit only short-range order. In the case of gases, there is neither short-range nor long-range order and the radial distribution function is flat, except for distances smaller than the atomic radius, for which it is zero (see figure 3.1). The ensemble of grain boundaries would have had the same kind of disorder as a gas and a similar radial distribution function, with interatomic distances and coordination between nearest-neighbours assuming a wide variety of values.

The atoms located at grain boundaries are not necessarily located at positions which correspond to the lattice of both adjacent crystals. This causes a displacement of atoms located several atomic layers inside crystals [37]. These strains, while unimportant in coarse-grained materials, are bound to affect the structural and thermodynamic properties of materials as the crystallite size is reduced to a few nanometers, therefore a few lattice spacings.

Grain boundaries are also expected to have an effect on the diffusion of chemical species because of the larger free volume inside grain boundaries. Mütschele and Kirchheim [63] have found hydrogen diffusion to be faster in nanocrystalline palladium at certain concentrations than in single crystals. The diffusional flow of atoms at grain boundaries is thought to be responsible for the low temperature ductility of nanocrystalline ceramics [47].

3.3 *Hydrogen in nanophase materials*

Two series of studies have been done on nanocrystalline palladium. One by Mütschele and Kirchheim [63, 62] and another by Eastman et al. [23, 25].

Mütschele and Kirchheim have performed diffusion measurements as well as isothermal equilibrium curves by electrochemical methods on Pd samples with a crystallite size of 5nm. Here there is a relation between the chemical potential and the cell voltage instead of the logarithm of the hydrogen pressure. Starting at zero concentration of hydrogen, the diffusion coefficient of nanocrystalline palladium is smaller than that of palladium single crystals. The diffusion coefficient increases with hydrogen concen-

tration and becomes larger than the coefficient for single crystals at a concentration $H/Pd \simeq 0.003$. The diffusion coefficient reaches a maximum at $H/Pd \simeq 0.03$, after which the diffusivity starts decreasing with increasing concentration.

In a second article [62] Mütschele and Kirchheim have determined pressure-composition isotherms using the same electrochemical charging method. They found a miscibility gap at the same voltage for both nanocrystalline ($\sim 10\text{nm}$) and coarse-grained samples. The plateau however is narrower in the case of the nanocrystalline sample. The maximum hydrogen solubility in the alpha phase is $c_\alpha = 0.03$ and the minimum hydrogen content of the beta phase is $c_\beta = 0.44$ compared to $c_\alpha = 0.015$ and $c_\beta = 0.58$ for the coarse-grained sample. Mütschele and Kirchheim interpreted this difference by assuming that the grain-boundary regions, which would have a thickness of 0.7 to 1.1nm, do not form the β -Pd-H phase.

J.A. Eastman and other investigators have drawn other conclusions. In a transmission electron microscopy study (TEM) of nanocrystalline palladium [83] they conclude that grain boundaries of palladium are highly ordered and that the region showing large displacements from ideal lattice positions does not exceed 0.4nm. This study was followed by a precise analysis of the diffuse background intensity from X-ray diffraction by nanocrystalline and coarse-grained palladium [31]. They found that the background intensity is the same for both materials and concluded that nanocrystalline palladium did not have a large volume of a highly disordered grain boundary phase. They proposed that the increased background intensity between Bragg peaks reported in nanocrystalline α -Fe [110] was in fact the intensity from the tails of the neighbouring peaks, dismissing the possibility of large relaxation effects near grain boundaries. They also measured pressure-composition isotherms on nanocrystalline palladium [23, 25]. They used an indirect method, the lattice expansion determined from X-ray diffraction, to obtain the hydrogen concentration. However, the X-ray diffraction data obtained during hydrogen charging was useful in following the transformation from the α to the β phase. They argue that these two latest studies support their previous conclusions that there is no extra solubility at highly disordered grain boundary regions and that the narrowing of the miscibility gap also observed by Mütschele and Kirchheim [62] is due to a change of the free energy of solution in the

bulk of the lattice with decreasing crystallite size. They point to atomic displacements of thermal or static origin to explain the modification in storage behavior.

Monte Carlo simulations have also been done on nanometer-sized clusters of palladium using embedded atom method potentials [94]. The results indicate that hydrogen is stored at the surface first, then inside the nanocrystals. Nanocrystalline palladium is evidently different from isolated nanocrystals but this information is still interesting given that there is excess free volume in grain boundaries.

A recent study [79] of vibrational modes of hydrogen in nanocrystalline palladium by inelastic neutron-scattering experiments reveals two types of storage sites: interfacial sites and lattice sites similar to those found in coarse-grained palladium. The authors propose that the results of Eastman et al. can be explained by the long-range strains induced by the hydrogen stored at grain boundary sites, which can cause an expansion of the lattice without the presence of hydrogen in the bulk of the nanocrystals. They also point out that these interfacial sites, with different potential energies and vibrational properties, may still be located at crystallographic lattice positions.

Although our experiments involves iron-titanium only, we intend to extrapolate from our analysis of the Fe-Ti system to understand some aspects of the nanophase Pd-H system.

BALL MILLING

4.1 History of ball milling

Since their initial discovery by Duwez et al. [44] in 1960, metallic glasses have been mostly synthesized by rapid quenching from the melt, usually by the technique known as melt spinning. The quenching process imposes a limit on the size of the samples because of the cooling rate requirements. Today it is possible to manufacture wide sheets of amorphous metallic alloys, however thickness is limited to the order of 10 microns or less. Amorphous metallic alloys have also been prepared by thin film deposition at low temperature since as early as 1954 [12]. An alternative process, called mechanical alloying, is now widely used in laboratories to make these new alloys and offers the prospect of manufacturing amorphous alloys in bulk form.

Mechanical alloying is a process in which an alloy is formed by direct reaction in the solid state between elemental components, which are subjected to intense mechanical deformation. The apparatus usually consists of a container placed in a rotating (e.g. attritor, planetary ball mill) or vibrating frame (shaker mill). Inside the container is placed a certain number of balls made of hard steel or tungsten carbide and material to be alloyed, called the charge. Non metallic ball mills (e.g. agate) also exist but are usually only used for mixing, not for alloying. In the present work we have used only metallic milling tools.

We may define high energy ball milling as a ball milling process in which the energy transfer to the charge is such that it provokes structural modifications at the atomic level. In a SPEX mill the energy of collisions between balls is around 0.01 J. A few collisions reach 0.1 J [19].

In the past mechanical alloying by ball milling has been extensively used to produce

dispersion strengthened alloys [36]. In these alloys a small quantity of oxides are dispersed in a metallic matrix. Following the work of Yermakov et al. on Y-Co and Gd-Co [99, 98] which was not widely known, an article by Koch et al. [52] published in 1983 attracted the attention of materials scientists to the possibility that amorphous alloys could be synthesized by ball milling. After a little more than 10 hours of milling in a SPEX 8000 mixer/mill they obtained amorphous Ni₆₀Nb₄₀, as seen by X-ray diffraction, from a mixture of pure elements. Schwarz and Koch [77] subsequently produced amorphous alloys in the Ni-Ti system.

These results were since confirmed by many other groups and at the time of writing many different amorphous alloys have been produced by this technique. Comparison between amorphous alloys produced by ball milling and rapid quenching [10] shows only minor differences in some physical properties and it is observed that both processes lead to the same atomic structure.

4.2 *The process of ball milling.*

The mechanics of ball milling have been first described by Benjamin and Volin [7]. It involves repeated fracture and cold welding. As far as ductile elements are concerned, repeated fracture and cold welding of particles lead to the formation of a layered structure made from the two starting elements (in the case where we start with two elemental powders) as shown by scanning electron microscopy. It is believed that a solid state amorphization reaction is taking place at the interfaces, similar to the one described by Schwarz et al. [76] for Au-La multilayers. The layered structure present in ball milled powder particles provides clean interfaces for a diffusive reaction between the two elements. Continuous homogenization of the powder leads to a complete reaction.

When we start with an intermetallic compound instead of elemental components to form an amorphous alloy the mechanism must be very different. Obviously, in this last situation, there is no such thing as a layered structure inside powder particles. The process can also be very different when brittle materials are considered, again non ductile materials cannot form layered structures.

4.3 *Amorphization by ball milling.*

There are two generally accepted conditions to the formation of an amorphous binary alloy starting from pure elements [76]:

- 1) One of the elements must be a fast diffuser in the other element
- 2) The heat of mixing in the amorphous alloy must be large and negative.

The diffusion of one element into the other occurs at the interfaces formed between the two components. The system is driven by the negative heat of mixing into a state of lower energy (the metastable amorphous state) while the transformation into a more stable crystalline state is kinetically suppressed, either because the temperature does not rise above that of the glass transition or because the material cools too rapidly after each impact for crystallization to take place. The fast diffusion ($\sim 10^{-11} \text{ cm}^2/\text{s}$ at $\sim 400\text{K}$) of one element into the other allows the solid state amorphization reaction to take place below the glass transition.

The amorphization of intermetallic compounds occurs when a sufficient amount of defects increases the free energy of the system above that of the amorphous alloy. The system then lowers its free energy by transforming into the amorphous state. It must be noted that not all intermetallic compounds can be amorphized by ball milling and that the result of these experiments may strongly depend upon particular parameters related to the equipment used. The inverse reaction is possible, some amorphous alloys become crystalline when submitted to ball milling [90].

4.4 *An analysis of the physics of ball milling.*

In the early days of amorphization by ball milling there was no quantitative understanding of the physical processes occurring. Such problems as the movement of the balls, the amount of powder crushed during collisions, the distribution of angles of collision, and the transfer of energy during collisions, for example, still had to be addressed. Recently, however, a model has been put forward by Maurice and Courtney [60]. They use an impact theory due to Hertz [56]. They assume that ball on ball and ball on wall collisions (without powder) are elastic (the compression energy is restored after impact). They then suppose that the powder between colliding surfaces does not substantially alter the collisions. Calculations show that for a SPEX mill

the amount of energy transferred to the powder is of the order of a few percent of the energy of compression. The model has not yet been applied to the understanding of a particular alloy but gives some suggestion about the temperatures encountered during ball milling as we shall see in the next section.

4.5 *The question of temperature.*

A very important question yet to be resolved in any analysis of ball milling is a precise evaluation of the temperatures the powders are subjected to during the process. Two temperatures have to be considered: the average ambient temperature in the vial and the maximum temperature during collisions.

The ambient temperature is slightly higher than room temperature (a fact easily observed by measuring the container's temperature) but this has little impact on the process. The more important value is the maximum temperature during the collisions. In their article, Maurice and Courtney showed that in a SPEX mill, powder grains had enough time to cool to ambient temperature between the collisions. They give temperature rises for several materials and mill configurations. Values are generally below 200K; however we should be cautious. Miller et al. [61] determined that crystalline solids submitted to a rapid deformation show local temperature rises far greater than those one would get assuming that the heat is distributed over all the material. Davis et al. [19], using a computer model, found that temperature rises had to be not more than 350K. They also performed an experiment in which they monitored the martensitic transformation in a certain type of steel. They concluded that no transformations involving temperature rises higher than 300K occurred. However, ball milling is very different from a thermal process and usually structural transformations can not be explained as being caused solely by heating, a fact that has been clearly demonstrated recently [90]. In the case of AlNi, an explosive reaction takes place during milling, probably sustained by the large heat of mixing. Electron microscopy provides evidence that melting occurs in this case [5].

We must conclude that thermal phenomena in ball milling processes are not clearly understood. Also, the temperatures encountered during collisions are not precisely known:

4.6 Nanophase materials made by ball milling

The first method used for the systematic synthesis of nanophase materials was gas phase condensation. Metals are evaporated in an evacuated chamber backfilled with an inert gas and collected on a cold finger - Clusters forming on this cold finger are scraped and compacted in vacuum [9].

The method of ball milling is now widely used in laboratories to produce nanophase materials in large amounts. While certain alloys simply become amorphous after long milling times, others remain in a nanocrystalline form with constant grain size after a certain milling time. The parameters that determine the final crystallite size are under investigation (see references [51, 71, 26, 35, 55]).

4.7 CALPHAD calculations

4.7.1 Historical notes

The CALPHAD method mentioned in chapter 2 has been successfully used in the past to make predictions about the thermodynamics of metastable phases by extrapolating from available thermodynamic data on a given binary system. The purpose of this section is to give the reader an introduction to the CALPHAD method in order to understand the calculations of the free energies of phases in the Fe-Ti system we refer to in our analysis [95, 97].

The history of the CALPHAD method (from *calculation of phase diagram*) can be traced back to the work of Bernstein and Kaufman [48]. The computer program used to calculate the free energy of phases in the Fe-Ti system was written by Lukacs et al. [57, 58]. Basically, the free energies of phases are expressed as analytical functions in terms of composition and temperature. These expressions are compared to available experimental thermodynamic data and the coefficient of each term is optimized in order to obtain the best fit.

4.7.2 Analytical formulation

The temperature dependence of pure elements is given by the SGTE description [64]:

$$G_i(T) = A_i + B_i T + C_i T \ln T + D_i T^2 + E_i/T + F_i T^3 + G_{i,mag}, \quad (4.1)$$

where a magnetic term $G_{i,mag}$ is included. The free energy of a binary solution is given by

$$G(x_1, x_2) = x_1G_1 + x_2G_2 + G_{EX} - TS_{MIX}. \quad (4.2)$$

In (4.2) we have weighed contributions from the pure elements x_1G_1 and x_2G_2 , an ideal mixing entropy term

$$S_{MIX} = R(x_1 \ln x_1 + x_2 \ln x_2), \quad (4.3)$$

and an excess term given by a Redlich-Kister [68] expression:

$$G_{EX} = x_1x_2 \sum_{j=0}^m a_j(x_1 - x_2)^j - Tx_1x_2 \sum_{k=0}^n b_k(x_1 - x_2)^k - \frac{1}{T}x_1x_2 \sum_{l=0}^p c_l(x_1 - x_2)^l. \quad (4.4)$$

The first series contains higher order terms of the enthalpy and reduces to the regular solution model in the case $m = 0$. The higher order terms for the entropy are in the second series. The temperature dependence of the specific heat of liquids is found in the third series, which takes into account the effect of short-range order [66]. The short-range order becomes important for amorphous phases which are described as undercooled liquids below the glass transition. The free energy of a compound is given by

$$G_c = x_1G_1 + x_2G_2 + \Delta H_c - T\Delta S_c, \quad (4.5)$$

where ΔH_c and ΔS_c are respectively the enthalpy and entropy of formation of the compound. A description similar to the solution model given above may be used if one wants to investigate compositions which deviate from the nominal stoichiometry of the compound.

The specific heat is given by the Neumann-Kopp rule:

$$C_p = x_1C_{p1} + x_2C_{p2}, \quad (4.6)$$

except for liquid phases where an excess specific heat is considered as in equation (4.4).

4.7.3 Calculation of coefficients

The free energy of phases can be expressed as

$$G = f(c_r, T, x), \quad (4.7)$$

where the c_r 's can be the coefficients a_j , b_k , and c_l of equation (4.4) or ΔH_c and ΔS_c of equation (4.5). The concentration of the two elements are not independent and only one of them has to be used. This is why there is only one concentration, x , appearing in (4.7). Suppose we have m measured thermodynamic quantities Q_m (heats of formation, crystallization, melting, etc...). These can be linked to the coefficients c_r by means of (4.7). We have to decide which coefficients will be considered. This choice is a very important step in the CALPHAD calculation. Physical considerations are involved in the selection of coefficients. A modified set of coefficients may be considered in light of the results of the first calculations.

One might go to the extreme of using as many coefficients there are measured quantities in order to obtain a perfect fit. However this approach would probably lead to unphysical results as the results are extrapolated. It is often best to use as few coefficients as necessary while keeping the errors at reasonable values.

The computer program is provided with a trial set of coefficients and optimizes their value in order to minimize the mean square deviation:

$$\sum_m w_m (Q_{m,cal} - Q_{m,exp})^2. \quad (4.8)$$

where the weighing factor w_m depends on the uncertainty on each measured quantity:

$$w_m = \frac{1}{(\Delta Q_{m,exp})^2} + \left(\frac{\partial Q_m}{\partial T} \Delta T \right)^2 + \left(\frac{\partial Q_m}{\partial x} \Delta x \right)^2. \quad (4.9)$$

$\Delta Q_{m,exp}$ is the uncertainty on the measured quantity $Q_{m,exp}$, while Δx and ΔT are the respective uncertainties on composition and temperature for that measurement. The w_m factors give more weight to measurements which are more precise.

All CALPHAD calculations were performed by Zhi-Hua Yan at Hydro-Québec [97, 95] in collaboration with Rüdiger Bormann of GKSS Research Center (Geesthacht, Germany).

4.7.4 Validity of CALPHAD calculations

CALPHAD calculations can be used to calculate the free energies of metastable phases and predict possible phase transformations in processes where metastable and stable equilibrium free energies play a role. For example the free energies calculated by the CALPHAD method correctly predict the range of compositions where bcc Ti-Cr will

transform to an amorphous phase (inverse melting [96]). It has also been used to analyze the behavior of binary systems during ball milling. It is known that during ball milling the temperature reached during collisions is rarely sufficient to directly induce phase transformations and that the transformations proceed by an increase of the free energy through the gradual introduction of defects. In particular the main mechanism for the amorphization of intermetallic alloys is thought to be chemical disorder [6].

EXPERIMENTAL METHODS

5.1 *Milling procedure*

Milling was carried out in a commercial SPEX 8000 mixer/mill. We used 0.5 inch tungsten carbide balls with cobalt as a binder and a custom made tungsten carbide vial. This vial had an internal diameter of $1\frac{3}{8}$ inch (34.9 mm) and internal height of $1\frac{5}{8}$ inch (41.3 mm). Before milling the vial was sealed in a glove box with continuous flow of argon. A rubber o-ring with silicon-based vacuum grease was used. Pure powders of iron (99.9%) and titanium (99.5%) were used in our milling experiments. Their X-ray diffraction patterns are shown in figure 5.1. In certain experiments the pure powders were weighed in the desired composition and directly introduced into the vial for milling. For experiments on the intermetallic compound these powders were thoroughly mixed, pressed into a pellet and melted at least twice in the arc-furnace. Using powders introduced extra amounts of oxygen. Therefore we did another series of milling experiments with the pre-formed intermetallic compound, starting with solid pieces of iron (99.98%) and titanium (99.7%). This last series of samples was used in hydrogen storage experiments on the milled intermetallic compound.

We also performed a series of milling experiments where oxygen was added on purpose by means of iron oxide (99.7%), mixed with the pure metals in the proportions giving the desired composition.

The weight of the iron and titanium part was weighed to a precision of 0.001 gram. All starting mixtures had a mass of 4.000 ± 0.002 grams. Samples generally lost ~ 0.05 gram during arc-melting. After milling the vial was opened inside the glove box and samples kept there until used in measurements. Usually, 1 gram of material was recovered after milling. The rest of the powder was stuck to the walls of the vial and

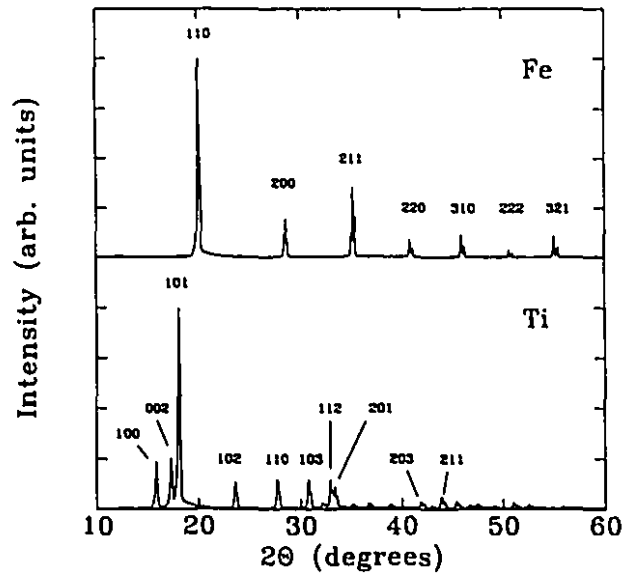


Figure 5.1: X-ray diffraction patterns of iron and titanium powders used in this study.

to the balls. The vial was cleaned by milling without sample and with water in the vial. Sometimes, when large amounts of metals were stuck on the walls of the vial, milling with clean glass was effective in removing them. A few times the vial had to be re-machined. The balls were replaced regularly.

5.2 X-ray apparatus

X-ray diffraction was performed in a Philips PW1050 diffractometer with large focus $\text{MoK}\alpha$ radiation, a planar graphite monochromator and a scintillation detector. The powders were placed on a glass plate with four layers of scotch tape as a spacer. The samples were thick enough to prevent any signal from the glass plate.

The same parameters were used for each sample. The step between points was 0.05° . We measured the intensity from $2\theta=10^\circ$ to 90° . We counted for 30 seconds at each point.

5.3 Analysis of X-ray data

5.3.1 Peak analysis

The characteristics of X-ray peaks (position, area, width at half-maximum) were obtained by fitting the peak with a sum of Gaussian and Lorentzian functions. We used a sum of Gaussian and Lorentzian components only to obtain a better fit. It is known however that the broadening related to crystal size is best described by a Lorentzian function while strain broadening is closer to a Gaussian function [49], a fact we have observed in our measurements.

We used the Marquardt-Levenberg fitting procedure. A linear function was included to account for the incoherent scattering. Since both $K\alpha_1$ and $K\alpha_2$ wavelengths were present in the pattern we had to introduce doublets of peaks with determined relations between their respective positions, areas, and widths.

The wavelengths of $K\alpha_1$ and $K\alpha_2$ are 0.70930 Å and 0.71359 Å respectively. We designate them by λ_1 and λ_2 . The function describing a peak is:

$$\begin{aligned} & \frac{I_{g1}}{w_1} \sqrt{\frac{4 \ln 2}{\pi}} e^{-4 \ln 2 \left(\frac{\theta-\theta_1}{w_1}\right)^2} + \frac{I_{g2}}{w_2} \sqrt{\frac{4 \ln 2}{\pi}} e^{-4 \ln 2 \left(\frac{\theta-\theta_2}{w_2}\right)^2} \\ & + \frac{I_{l1}}{w_1} \sqrt{\frac{4 \ln 2}{\pi}} \frac{1}{1 + 4 \ln 2 \left(\frac{\theta-\theta_1}{w_1}\right)^2} \\ & + \frac{I_{l2}}{w_2} \sqrt{\frac{4 \ln 2}{\pi}} \frac{1}{1 + 4 \ln 2 \left(\frac{\theta-\theta_2}{w_2}\right)^2} \end{aligned} \quad (5.1)$$

where

$$\theta_2 = 2 \arcsin \left[\frac{\lambda_2}{\lambda_1} \sin \left(\frac{\theta_1}{2} \right) \right] \quad (5.2)$$

$$I_{g2} = \frac{1}{2} I_{g1} \quad (5.3)$$

$$I_{l2} = \frac{1}{2} I_{l1} \quad (5.4)$$

$$w_2 = w_1. \quad (5.5)$$

In 5.1, the first and third terms are the Gaussian and Lorentzian components of the peak. The second and fourth terms are the Gaussian and Lorentzian components of the companion peak produced by the $K\alpha_2$ wavelength. We have used the area to

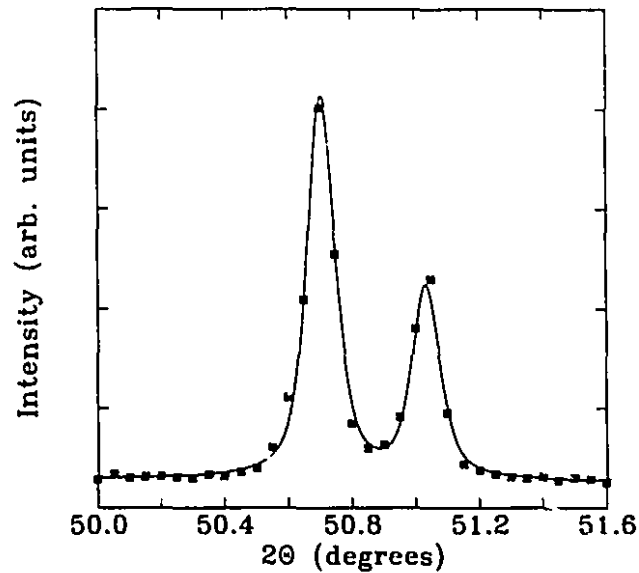


Figure 5.2: Example of a fit for the $[321]$ peak from the pure iron powder. The squares are experimental points and the solid line is the total calculated intensity which includes the diffraction peak and the linear background.

width ratio in 5.1 instead of the height of the peak because the area (or integrated intensity) is the parameter we used in our calculations.

Given that the peak from $K\alpha_2$ is fully determined by the parameters of the peak from $K\alpha_1$, there are only four independent parameters needed to describe a peak: θ_1 , I_{g1} and I_{l1} , as well as w_1 . Once the fitting procedure has been done for a peak, we used $I_{g1} + I_{l1}$ as the intensity in calculations.

Figure 5.2 shows the fit for a peak from the pure iron powder.

5.3.2 Determination of lattice parameter

The lattice parameter is determined from the position of X-ray peaks. The effect of systematic errors in the measurement of the diffraction angle becomes less important as the diffraction angle approaches 90° . Warren [93] suggests collecting lattice parameter values for angles near 90° , and then to perform a linear extrapolation to 90° . Because we used $MoK\alpha$ radiation in our experiments, peaks above $\Theta=45^\circ$ are very weak. We therefore used the peak ranging from 30 to 45 degrees ($2\Theta = 60^\circ$ to 90°). There is no systematic variation of the lattice parameter in this range of diffraction

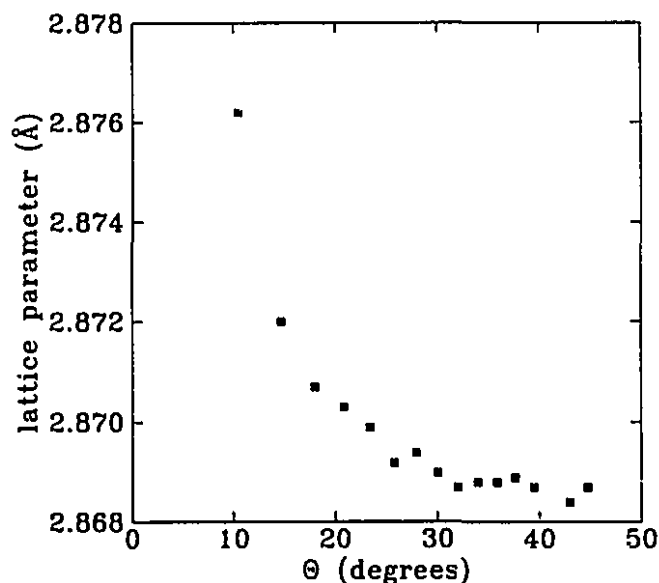


Figure 5.3: Lattice parameter as a function of diffraction angle for pure Fe.

angles. As an example we give the lattice parameter of Fe as a function of diffraction angle in figure 5.3. The value for each individual peak is precise to one part in a hundred thousand (close to $\Theta = 100^\circ$), but we see that these values fluctuate, limiting the actual precision of our measurements to 0.001 Å. We do not know the reason for these fluctuations. They are possibly related to the peak shape changing from one reflection to another. We obtained a value of 2.869 Å which compares well to the literature value of 2.867 Å [38]. The lattice parameters of the titanium hexagonal structure is much more difficult to determine since at high angles, we find an almost continuous superposition of peaks.

5.3.3 Determination of crystallite size

The average size of crystallites can easily be obtained from the width of diffraction peaks together with the strain (the root of the mean square deviation from the equilibrium position of the atoms). The derivation of the method is rather complicated and the reader is referred to Warren [93] for the detailed treatment.

The width must be given in reciprocal space. The instrumental broadening must be subtracted from the observed width. The way the instrumental broadening is

subtracted depends on the shape of the functions that describe the broadening from both the instrument and the crystallite size reduction. If the broadening from both the instrument and the sample is purely Gaussian, the correction is quadratic:

$$\Delta k = \sqrt{(\Delta k_{\text{observed}})^2 - (\Delta k_{\text{instrumental}})^2}. \quad (5.6)$$

In the case of Lorentzian functions, the correction is linear:

$$\Delta k = \Delta k_{\text{observed}} - \Delta k_{\text{instrumental}}. \quad (5.7)$$

We have used a sum of Gaussian and Lorentzian functions to model our peaks. Therefore we calculated the crystallite size using both a quadratic and a linear correction. We used the average as the final value and the difference as the error bar.

The instrumental broadening is approximately given by

$$\Delta k_{\text{instrumental}} = Ak + B \quad (5.8)$$

where A and B were determined using a standard sample with very large crystallite size. Once Δk is determined for peaks which are multiples of the same reflection, we plot it against k and perform a linear regression. The slope gives the value of the strain and the $\Delta k(k = 0)$ value gives the crystallite size according to the formula

$$D = \frac{0.9 \cdot 2\pi}{\Delta k(k = 0)}. \quad (5.9)$$

The value of D is the domain size along the direction chosen (as determined by the Miller indices). For cubic structures only 2 peaks are available for the linear regression because higher multiples are always buried under other reflections [93]. For example we can use the [110] and [220] reflections but the [330] reflection is superposed to the [411] reflection. The [200] and [400] peaks can also be used when the [400] peak is sufficiently sharp to be distinguished from the background.

Comparison between X-ray experiments and observations in the transmission electron microscope has shown that the crystallite size determination from the X-ray peak broadening is reliable.

5.3.4 Calculation of X-ray diffraction intensities

We calculated the relative intensity of X-ray peaks for the FeTi intermetallic compound using the structure factors provided in reference [93]. We also included the

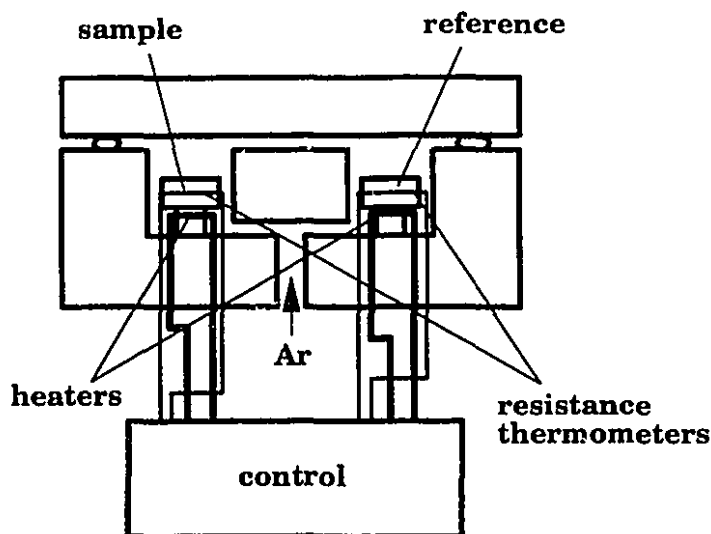


Figure 5.4: Schematic diagram of a differential scanning calorimeter.

multiplicity and Lorentz-polarization factors. The temperature factor was neglected. These calculated intensities were used for matters of comparison with experimental intensities. The calculated value of the ratio of the intensities of the [100] and [200] peaks were used to calculate the long-range order parameter of disordered FeTi.

5.4 DSC measurements

Differential scanning calorimetry measurements were done in a Perkin-Elmer DSC-2C with flowing argon. A differential scanning calorimeter (figure 5.4) is calibrated to heat a reference and a sample at a given rate. The sample holder and the reference are heated by resistive elements and the temperature measured by resistance thermometers. Argon flows through the apparatus to prevent reaction of the sample with air. Temperature differences between the sample and the reference are measured by the resistive thermometers and the computer records the power needed to keep them at the same temperature. The instrument therefore gives the heat flow in and out of the sample. One may thus measure enthalpies of transformations and transition temperatures.

The calorimetric behavior of nanocrystalline samples was difficult to analyze because there was heat released from 200°C to the maximum temperature the DSC could reach (725°C).

5.5 Scanning electron microscopy

We used a 30kV Hitachi S-570 scanning electron microscope to obtain images from the samples and verify their composition using energy dispersive X-ray analysis (EDX). The X-rays are emitted as excited electrons fall back to lower energy levels. We did not use a standard for this analysis, we therefore expect a precision of a few percents. In the case of Fe-Ti, since there is no light element, the precision is estimated at 2%. Generally, in the composition of a Fe_xTi_y sample ($x+y=100$), x and y could vary by 0.5.

5.6 Chemical analysis

For certain samples we had their hydrogen and oxygen content determined. The oxygen content was measured by melting the sample in a Leco O_2/N_2 analyzer. In this instrument, the sample is heated on a graphite crucible in an electrode furnace. The oxygen combines with carbon, passes through a rare earth copper oxide which transforms it into carbon dioxide. Carbon dioxide is detected by an infrared cell. Helium is used as a carrier gas. The uncertainty is 1% of the measured value.

The hydrogen content was measured in a Leco H_2 analyzer. The sample is heated in the same manner as in the O_2/N_2 analyzer except that the amount of hydrogen is determined by measuring the thermal conductivity of the gas. Hydrogen has a much higher thermal conductivity than other gases ($1.6 \times 10^9 \text{ Jm}^{-1}\text{s}^{-1}\text{K}^{-1}$ compared to $1.4 \times 10^9 \text{ Jm}^{-1}\text{s}^{-1}\text{K}^{-1}$ for helium and $2.0 \times 10^8 \text{ Jm}^{-1}\text{s}^{-1}\text{K}^{-1}$ for oxygen). The uncertainty is 1% of the measured value.

These chemical analyses were performed by a technician at the Materials Characterization Laboratory of Hydro-Québec ¹.

5.7 Hydrogen storage measurements

5.7.1 Description of the apparatus

Gas storage measurements were performed in the system shown in figure 5.5. The apparatus consists essentially of two compartments: a reference chamber, which includes

¹All experiments were performed by the author unless otherwise specified.

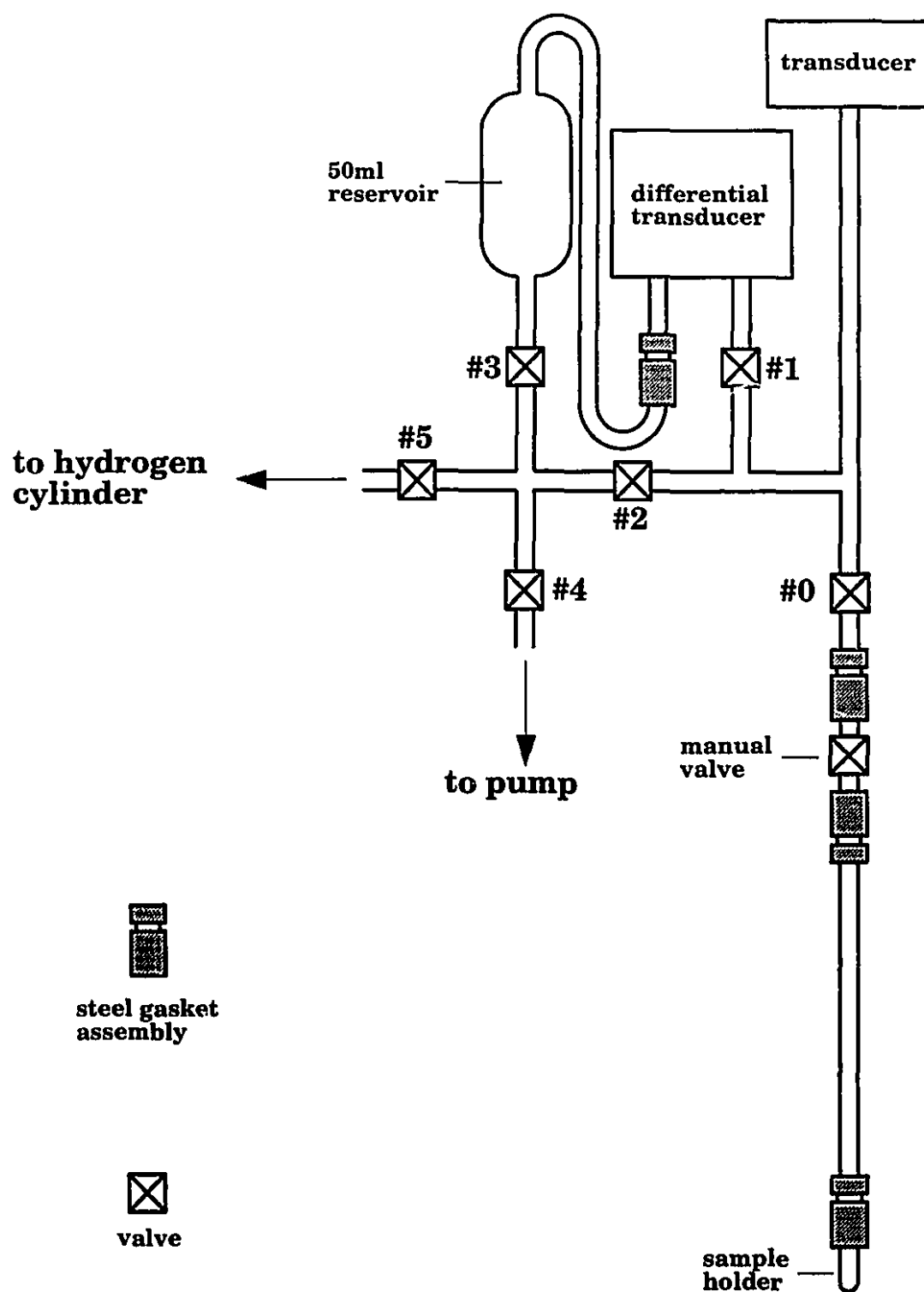


Figure 5.5: Gas-titration system.

a 50ml reservoir and goes from valve #3 to one port of the differential transducer, and a sample chamber, which is closed by valve #2, by the other port of the differential transducer, and by the sample holder itself, a small cylinder closed at the bottom. The gasket closing the sample holder has a filter to prevent the powder from traveling throughout the system.

The purpose of such a configuration is to provide very precise measurements of the pressure difference between the reference chamber and the sample chamber, allowing to precisely follow the evolution of the hydrogen pressure. The pressure inside the reference chamber is always close to that inside the sample chamber and the differential transducer is designed to be sensitive to small pressure differences, while the absolute transducer gives a reading of the pressure itself but is less sensitive to small changes in the pressure. When acquiring pressure-composition isothermal curves, the absolute transducer is used to obtain the value of the pressure, and the pressure change measured by the differential transducer is used to determine the amount of hydrogen absorbed.

The apparatus is connected to a high pressure hydrogen cylinder and a pumping station comprising a diffusion pump and a rotary pump. The tubes, valves, gaskets are made of 316 stainless steel. The valves are controlled by a computer which also reads the data from the two transducers.

The apparatus is encased in a Plexiglas box except for the components which are located below valve #0. These components are inside a plastic tube connected to the Plexiglas box. Air is circulated through the tube and inside the box by a small fan and kept at 32°C by a light bulb connected to a temperature controller. This temperature was chosen because it was easiest to maintain in the variable temperature conditions of the building.

A tubular furnace can be placed around the sample holder to heat the sample. This was done for activation treatments and can also be used for absorption measurements at high temperature.

5.7.2 *Measurement sequence*

We started the measurement of a pressure-composition isotherm by establishing a vacuum (10^{-9} atm) inside the apparatus. All valves were closed before starting the

experiment. The regulator on the hydrogen cylinder was set to a pressure of approximately 1 atm. Valve #5 was opened and then closed. We then opened in sequence valves #3, #2, and #1. A pause of 1 second was observed after which valve #3 was closed. After another pause of 1 second valve #0 was opened and the computer started collecting data from the two transducers.

Once equilibrium was reached the procedure described above was repeated. From time to time we increased the pressure setting on the regulator. This was necessary because if the pressure behind valve #5 was too high the pressure difference established by opening valve #0 and the subsequent pressure decrease in the sample chamber due to absorption would make the pressure difference between the two chambers exceed the range of the differential transducer. Once the maximum pressure for the experiment was reached and equilibrium for that pressure established, the pressure was decreased step by step, in the same way described for increasing the pressure except that instead of opening valve #5, we opened valve #4, which goes to the pump.

The experiment was terminated when the pressure went below a pre-determined limit. We fixed this limit at 0.3 atm because there was no interesting feature below this pressure and our gas-phase apparatus was not precise enough in that range to extract useful information.

5.7.3 Calibration

The relation between the density and pressure of the hydrogen gas is essential in order to determine the amount of hydrogen absorbed from a measurement of the change in pressure. The equation of state can be expressed as a series in terms of the specific volume of the gas (the so-called virial expansion):

$$P = RT \left(\frac{A}{v} + \frac{B}{v^2} + \frac{C}{v^3} \right). \quad (5.10)$$

R is the gas constant, P is the pressure, v is the specific volume, and A , B , and C are called the virial coefficients. These coefficients depend only on the nature of the gas and on temperature. Values of these coefficients are given by Dymond and Smith [22]. We calculated an average of the values we judged reliable, after performing a linear interpolation to get the coefficients for a temperature of 32°C. In our experiments,

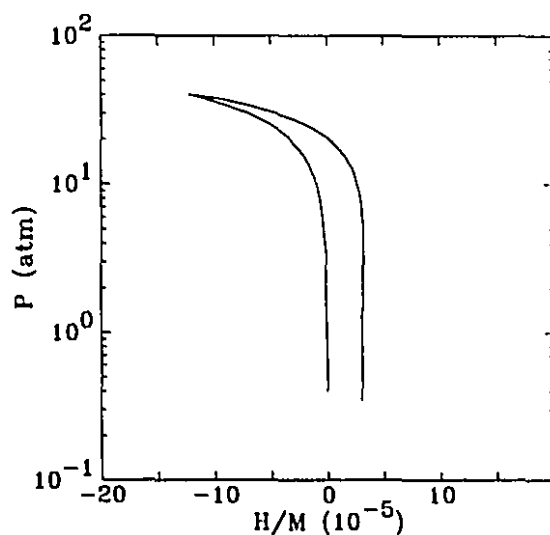


Figure 5.6: Background signal from the gas-titration system for a hypothetical sample of one mole.

all pressure-composition isotherms were determined at this temperature, therefore we did not require a temperature dependent expression for the coefficients. Even so, their temperature dependence is moderate. For example the value of B is -0.0148 ± 0.0005 at 300K (27°C) and -0.0152 ± 0.0005 at 400K (127°C). The values we used are:

$$A = 1 \text{ (exact)} \quad (5.11)$$

$$B = 0.0148 \pm 0.0005 \quad (5.12)$$

$$C = 0.00038 \pm 0.00007. \quad (5.13)$$

These values are valid for v in l/mol and P is in atm.

We had to determine the volume inside the sample chamber. First we established vacuum inside the sample chamber. Then we introduced a certain amount of gas inside the chamber except in the sample holder itself (the space below valve #0). After measuring the pressure, we opened valve #0 and we measured the pressure again. Using the equation of state 5.10, we determined in this manner the volume ratio between the sample chamber with and without the space below valve #0. This ratio was calculated several times at various pressures using helium and hydrogen. We calculated the same volume ratio with a reservoir of known volume connected to the sample holder. It was then a simple problem of linear algebra to determine the

internal volume of the sample chamber. We found $V_{SC} = 20.75 \pm 0.25$ ml.

This volume had to be corrected because of the presence of the sample and its expansion during absorption. We determined the volume of the sample by assuming a density of 100%. This is not unreasonable, hydrogen should be able to diffuse in all the pores of the material. We also considered an expansion of 2.9\AA^3 by hydrogen atom absorbed. This value is a compromise between the volume of hydrogen in the various phases and what would be expected for hydrogen dissolved in amorphous Fe-Ti.

A final correction due to the background signal from the instrument had to be performed. A change in the reading from the differential transducer was observed as the pressure was increased step by step. This change could be due to the small nonlinearity of the differential transducer or to the filter at the center of the gasket located above the sample (see bottom of figure 5.5). If complete equilibrium between the two sides of the filter (which restricts the movement of the gas) is not established before the computer begins data acquisition, a transient gas movement will register as an absorption in the experiment. Indeed a short pressure variation was observed in the first seconds of each measurement step, far shorter than the pressure variations associated with absorption or desorption in the sample. The resulting background for a sample of one mole is shown in figure 5.6.

We estimate the precision on the concentration to be 1.5%. This error mainly comes from the error on the volume of the sample chamber, the mass of the sample, and the temperature inside the sample chamber. The pressure measurement has a precision of 0.03 atm.

5.7.4 *Preparation of samples*

The samples used in hydrogen storage experiments were weighed and put in the sample holder within a few hours of their synthesis by ball milling. The steel gasket with filter was put on the sample holder, the manual valve on the sample holder assembly was closed and the assembly was connected to the gas-titration apparatus, using another steel gasket. Vacuum was established in the apparatus. At no time was the sample exposed to air from the moment it was introduced in the vial for milling to the end of storage experiments.

After vacuum was established in the sample holder we heated the sample to 400°C and continuously pumped for 30 minutes. It was then cooled to 32°C . This was followed by the activation treatment. We decided to use an activation treatment similar to that of Reilly and Wiswall [70]. A high hydrogen pressure was introduced (~ 50 atm) and we waited until the system reached equilibrium. The absorption at 50 atm was simply followed with the absolute transducer since the pressure change in such experiments was very large. The pressure was then decreased to ~ 7 atm and the sample annealed at 400°C for half an hour. The apparatus was again evacuated and the sample cooled to 32°C . This activation treatment was repeated until the absorption curve at 50 atm stopped evolving. Pressure-composition isotherms could then be obtained. After a complete absorption-desorption cycle the sample was heated to 400°C and cooled immediately while pumping in order to be certain that as little hydrogen as possible was left inside the sample.

BALL MILLING OF FE-TI

6.1 Nanocrystalline Fe₅₀Ti₅₀

The results for the first series of milling experiments are shown in figure 6.1 where we started with the intermetallic compound FeTi prepared by arc-melting. Some investigators submit their samples to long annealing treatments at high temperatures ($\sim 1000^\circ\text{C}$) but we have found that melting the FeTi ingots twice makes the samples free of Ti precipitates. As milling time increases, X-ray peaks become broader. A certain amount of tungsten carbide goes into the sample as a result of the wear of the grinding material (vial and balls). The crystallite size and strain evaluated from the broadening of the X-ray peaks is shown on figures 6.2 and 6.3. Both of them vary rapidly in the first two hours of milling. After 20 hours, a steady state is reached. Milling up to 40 hours does not bring any significant change. The sample milled 10 hours does not seem to be consistent with the other samples, especially if we consider the strain value. It is possible that something happened during the experiments that caused a larger amount of oxygen to be present (the influence of oxygen is discussed in the next section). The final crystallite size is around 11 nanometers. The final strain value is approximately 1.5%.

The small difference in scattering factor between Fe ($Z=26$) and Ti ($Z=22$) makes the measurement of the long-range order parameter (S) difficult. The integrated intensity of the (100) peak, which is the super-lattice peak of the bcc structure, is 1.6% of the strongest reflexion (110). Long counting times in the diffractometer allow an approximate measurement of S (see figures 6.4 and 6.5). At long milling times the (100) peak has to be de-convoluted from one of the tungsten carbide peaks. The

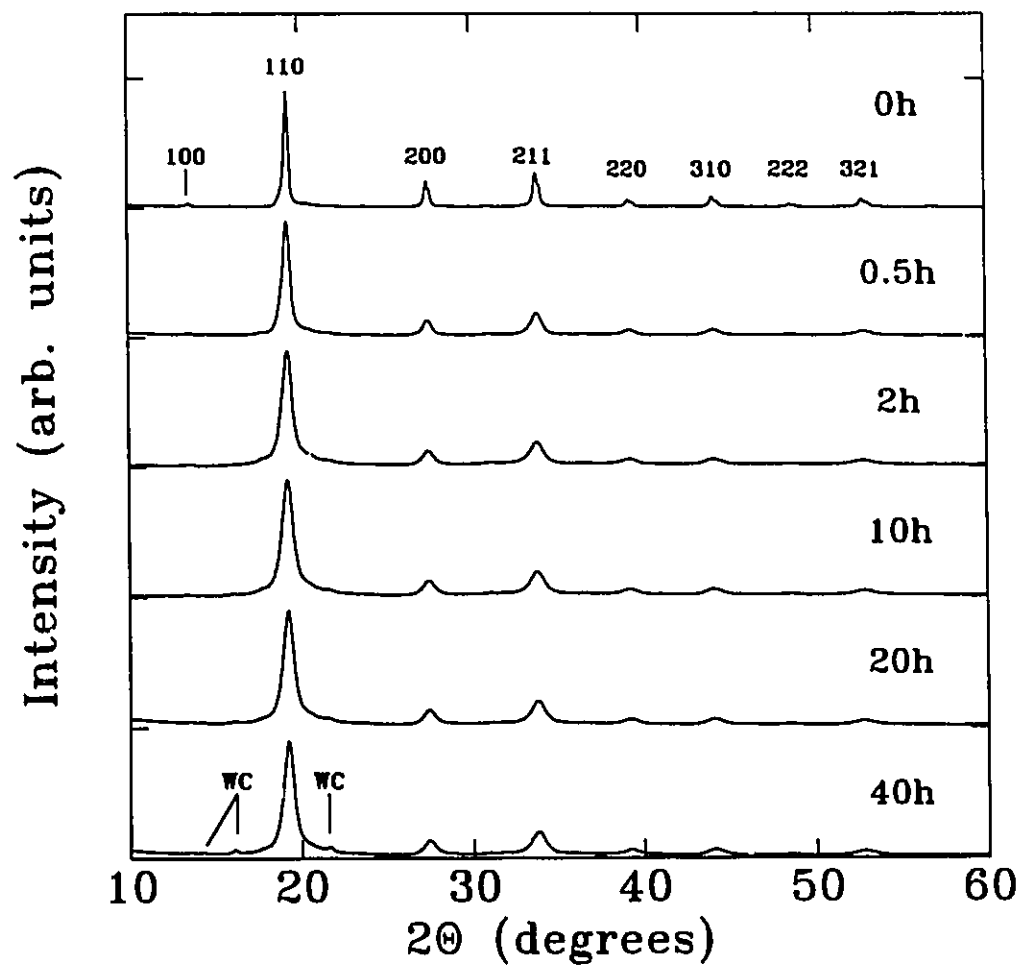


Figure 6.1: X-ray pattern of $\text{Fe}_{50}\text{Ti}_{50}$ (intermetallic compound) after 0, 0.5, 2, 10, 20, and 40 hours of milling.

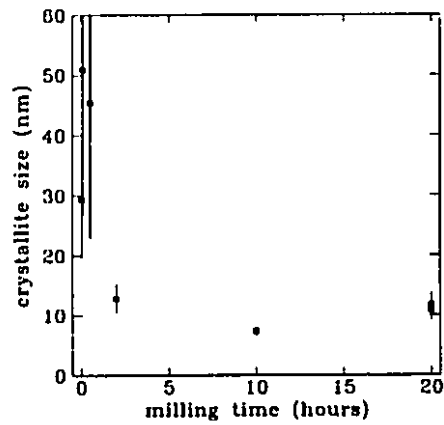


Figure 6.2: Crystallite size as a function of milling time.

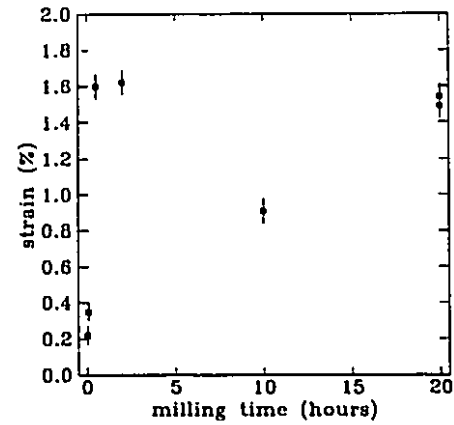


Figure 6.3: Strain as a function of milling time.

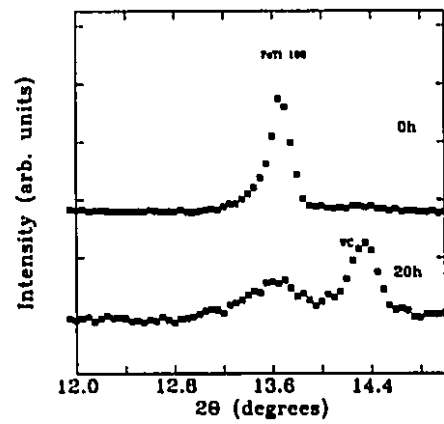


Figure 6.4: X-ray pattern of $\text{Fe}_{50}\text{Ti}_{50}$ (intermetallic compound) showing the (100) super-lattice peak at 0 and 20 hours of milling.

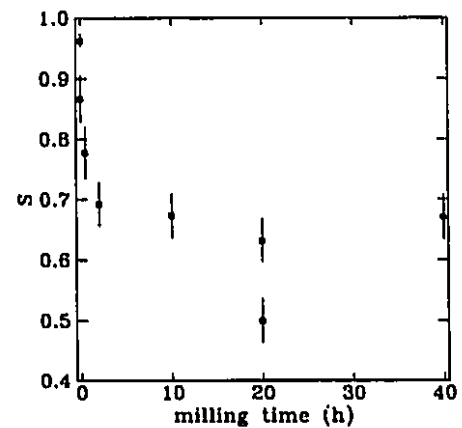


Figure 6.5: Long-range order parameter S of $\text{Fe}_{50}\text{Ti}_{50}$ (intermetallic compound) as a function of milling time.

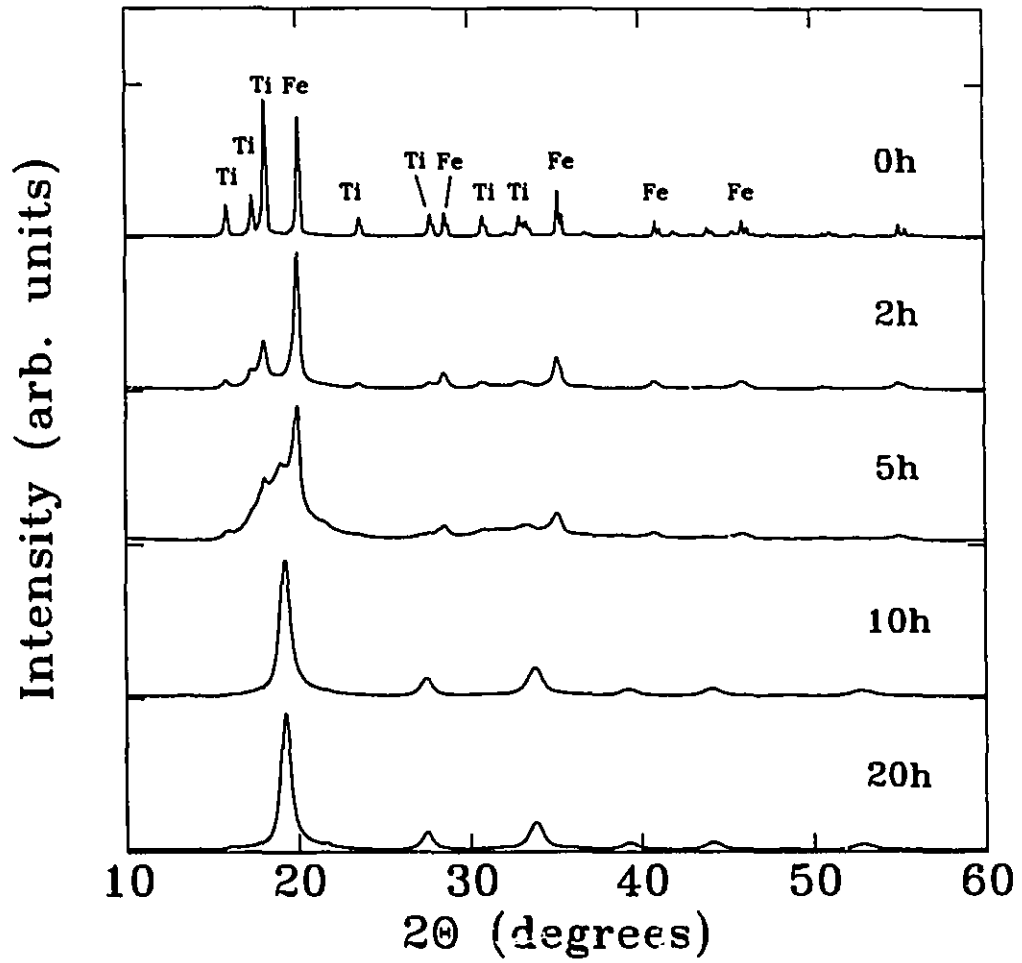


Figure 6.6: X-ray pattern of Fe₅₀Ti₅₀ (elemental powders) after 0, 2, 5, 10, and 20 hours of milling.

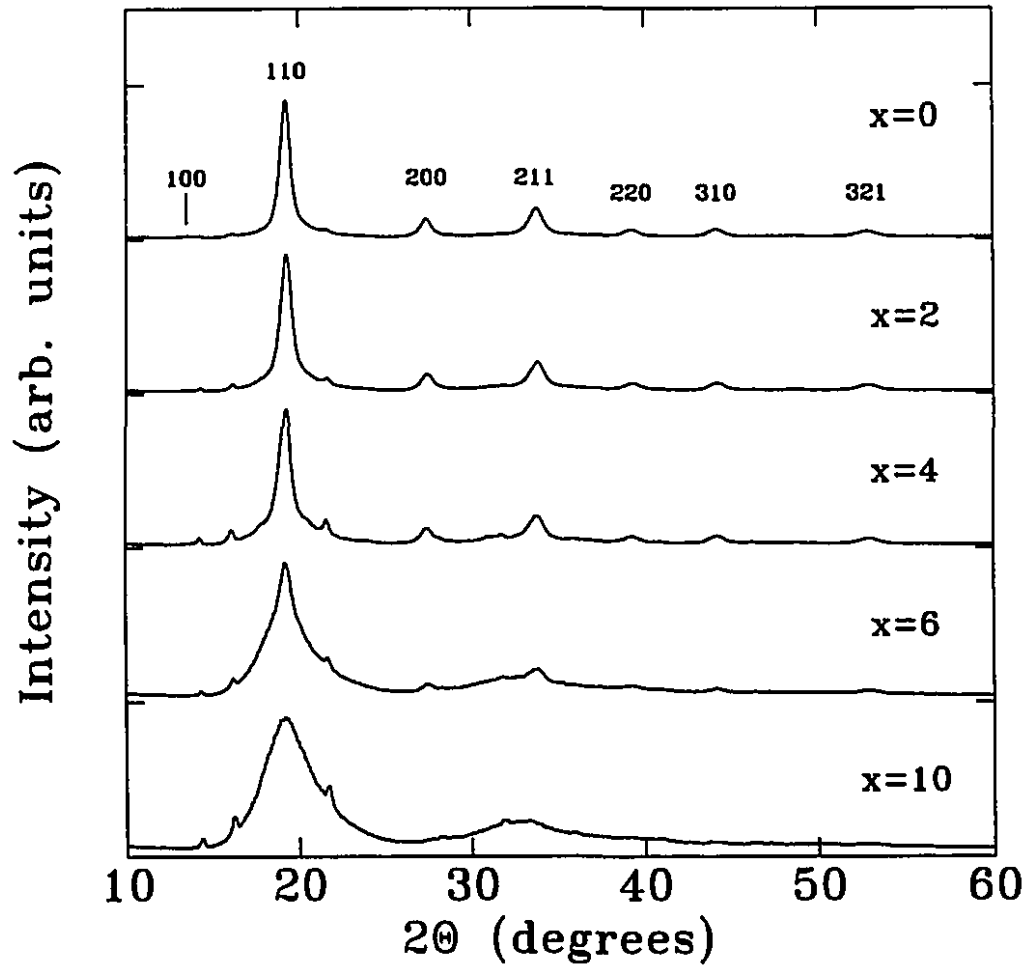


Figure 6.7: X-ray pattern of $\text{Fe}_{50-x}\text{Ti}_{50-x}\text{O}_x$ after 20 hours of milling.

definition of S is:

$$S = R_{\text{Fe}} + R_{\text{Ti}} - 1 \quad (6.1)$$

where R_{Fe} and R_{Ti} are the fraction of Fe sites occupied by Fe atoms and Ti sites occupied by Ti atoms respectively. The equilibrium FeTi intermetallic compound has $S = 1$ while the fully disordered bcc phase has $S = 0$. The value of S is given by the integrated intensity of super-lattice peaks. In the case of the (100) peak:

$$S = \sqrt{\left(\frac{I_{100}}{I_{100}(S=1)}\right)} \quad (6.2)$$

where $I_{100}(S=1)$ is the area for the fully ordered phase [93]. The intensity was normalized using the (200) peak. The evolution of S is given in figure 6.5. The final value of S is about 0.65.

The same nanocrystalline materials can be obtained by milling elemental powders of iron and titanium in the proportion $\text{Fe}_{50}\text{Ti}_{50}$ (figure 6.6). The resulting material has a crystallite size of 12nm and a long-range order parameter around 0.7.

An important factor in milling experiments is the effect of impurities, especially oxygen. In the case of Fe-Ti, our group has found [104] that above a certain concentration, oxygen causes the amorphization of Fe-Ti. This is shown in a series of milling experiments where we added iron oxide (Fe_2O_3) to the elemental powders in different concentrations. These mixtures were milled 20 hours, which we have determined to be amply sufficient to reach a steady state. The X-ray patterns of the materials produced in this way are shown in figure 6.7. At an oxygen concentration of 10% the material is fully amorphous. This is somewhat different from the 3% value obtained in a previous study [104]. This probably comes from the differences in milling conditions. The reactions occurring during the milling of iron and titanium elemental powders are discussed in later sections. We now turn our attention to the amorphous phase and its link with oxygen content.

6.2 Amorphous phase and oxygen content

A fact that escapes a first look is that the X-ray pattern of nanocrystalline samples includes the signal coming from an amorphous phase. To show this we have used

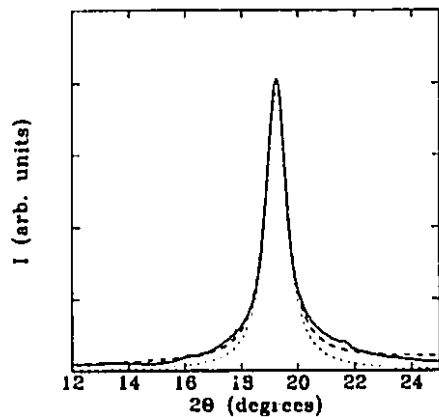


Figure 6.8: X-ray pattern fit of $\text{Fe}_{50}\text{Ti}_{50}$ (size: 6nm) [104] using one sharp peak. Dashed line: total calculated intensity (peak + background), dotted line: intensity from the peak alone.

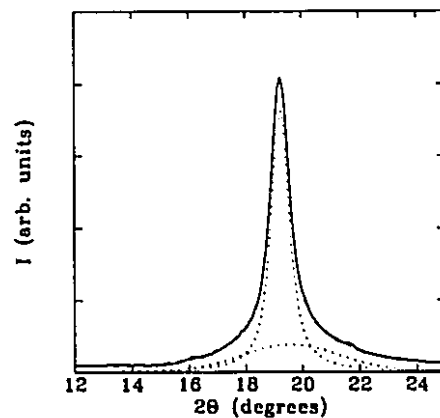


Figure 6.9: X-ray pattern fit of $\text{Fe}_{50}\text{Ti}_{50}$ (size: 6nm) [104] using a sharp peak and a broad peak. Dashed line: total calculated intensity, dotted lines: individual peaks.

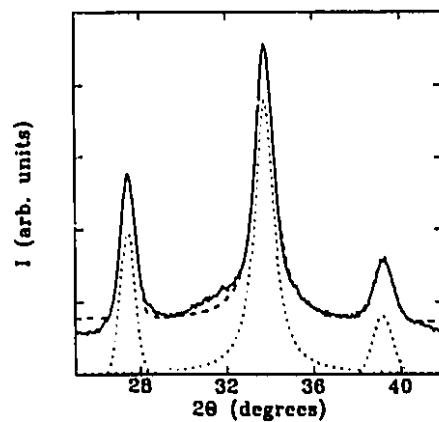


Figure 6.10: X-ray pattern fit of $\text{Fe}_{50}\text{Ti}_{50}$ (size: 6nm) [104] using three sharp peaks.

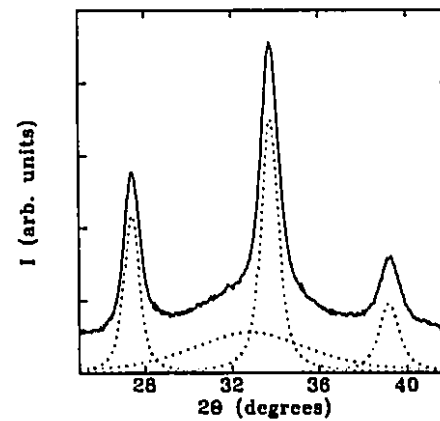


Figure 6.11: X-ray pattern fit of $\text{Fe}_{50}\text{Ti}_{50}$ (size: 6nm) [104] using three sharp peaks and one broad peak.

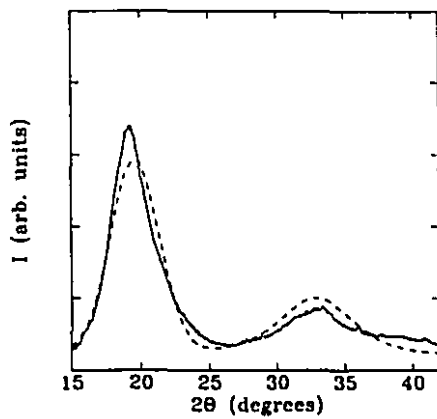


Figure 6.12: Comparison between the superposition of the two broad peaks obtained by fitting the 6nm sample and the experimental amorphous X-ray pattern.

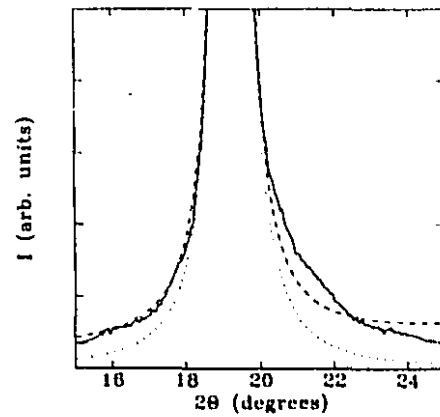


Figure 6.13: X-ray pattern fit of $\text{Fe}_{50}\text{Ti}_{50}$ milled 20 hours (size: 11nm) using one sharp peak.

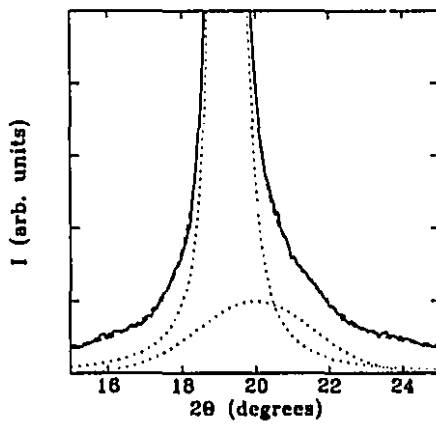


Figure 6.14: X-ray pattern fit of the same 11nm sample using a sharp peak and a broad peak.

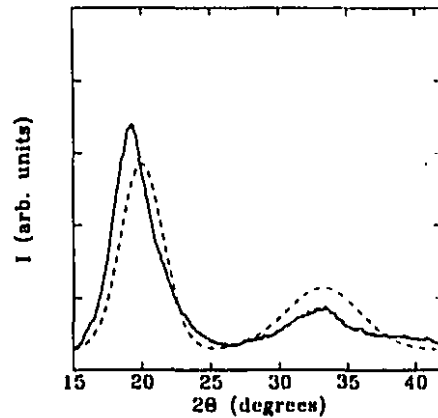


Figure 6.15: Comparison between the superposition of the two broad peaks obtained by fitting a sample milled 20 hours (size: 11nm) and the experimental amorphous pattern.

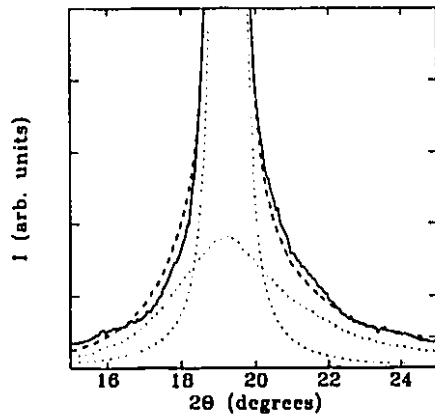


Figure 6.16: X-ray pattern fit of the 11nm sample using a sharp peak and the experimental pattern from amorphous $\text{Fe}_{15}\text{Ti}_{45}\text{O}_{10}$.

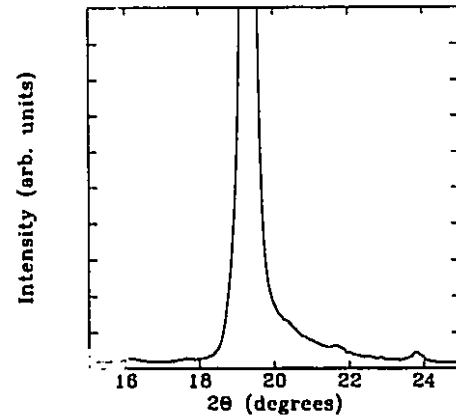


Figure 6.17: (110) peak of coarse-grained FeTi

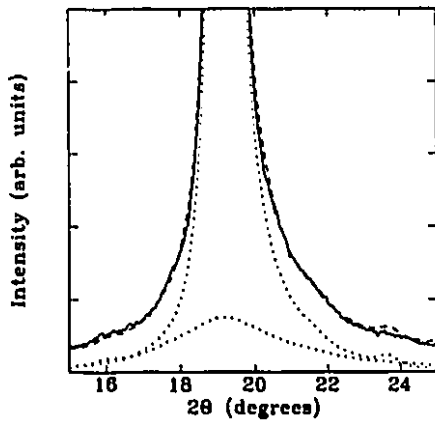


Figure 6.18: X-ray fit of nanocrystalline $\text{Fe}_{50}\text{Ti}_{50}$ (11nm) using the convolutions of Lorentzian functions and experimental peak functions together with the experimental pattern of amorphous $\text{Fe}_{50}\text{Ti}_{50}$ and a linear background.

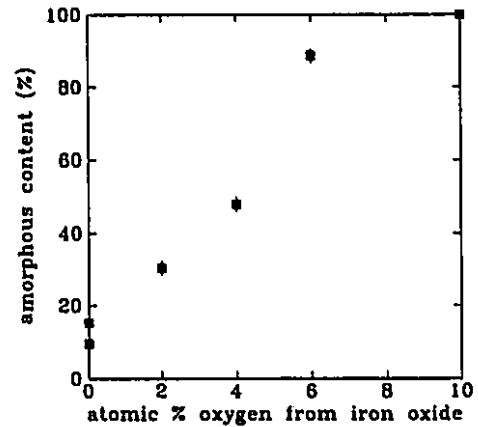


Figure 6.19: Amorphous content versus the amount of oxygen from iron oxide in Fe-Ti- Fe_2O_3 mixtures milled 20 hours.

Table 6.1: Peak areas of a 11nm sample for each type of correction for the amorphous content (first column: direction, second column: no correction, third: corrected with a broad peak, fourth corrected with the experimental amorphous pattern, fifth: FeTi intermetallic (experimental), sixth: FeTi intermetallic (calculated)).

hkl	original	broad peak	amorphous	FeTi (exp.)	FeTi (calc.)
110	100.0	100.0	100.0	100.0	100.0
200	10.8	15.0	15.3	26.4	16.6
211	26.3	25.1	28.8	35.0	31.8
220	4.3	7.7	5.6	8.5	9.2
310	8.1	9.4	10.3	12.1	11.9
222	1.2	1.4	1.6	3.2	2.7
321	8.6	10.0	10.9	11.1	12.1

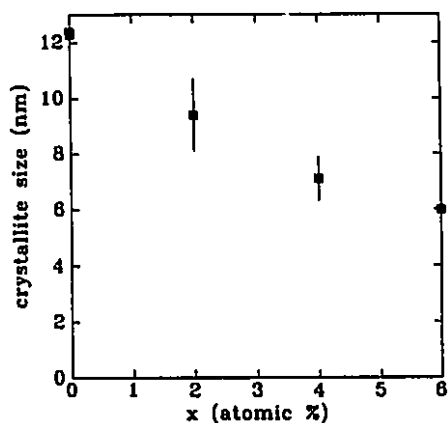


Figure 6.20: Final crystallite size of $\text{Fe}_{50-x}\text{Ti}_{50-x}\text{O}_x$ as a function of x .

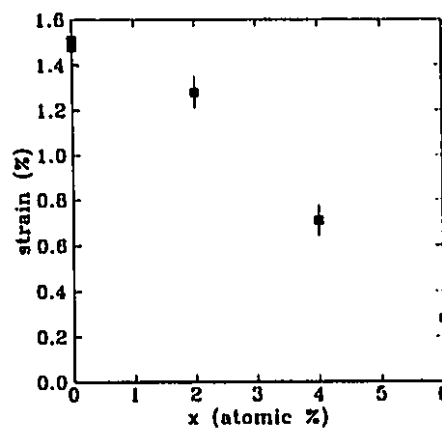


Figure 6.21: Strain in nanocrystals contained in $\text{Fe}_{50-x}\text{Ti}_{50-x}\text{O}_x$ samples as a function of x .

a 6nm sample made by L. Zaluski [104] on which we have performed our own X-ray measurements. Again, the different grain size is likely due to different milling conditions. We have fitted the main peak at around 20 degrees ([110] direction) with one sharp peak (figure 6.8) in a first step. In a second step we have done a similar fit using a sharp peak and a broad peak (figure 6.9). On these figures the solid line is the experimental intensity while the dashed line represents the total calculated intensity. Dotted lines represent the intensity of individual peaks. The fit with two peaks gives a mean square deviation one order of magnitude lower than with one peak. Visually, we can see that in the single peak fit the program attempts to take into account the left shoulder above 21 degrees with the help of the linear background. The calculated intensity does not follow the experimental data satisfactorily. On the other hand, the calculated intensity given by the double peak fit is practically indistinguishable from the experimental intensity. We have done a similar calculation for the three following peaks (figures 6.10 and 6.11). Again the use of a broad peak for the second maximum of the amorphous pattern clearly improves the fit of the experimental intensity. If we now take the two broad peaks obtained by this procedure and use them to fit the experimental intensity of amorphous $\text{Fe}_{45}\text{Ti}_{45}\text{O}_{10}$, allowing a multiplying factor and the adjustment of the linear background (figure 6.12), we see that the two curves are very similar. The multiplying factor is necessary since the amorphous deduced from the nanocrystalline sample is a fraction of the signal which would be obtained from a sample made only of this phase. In short, the function used for fitting is:

$$I = \text{factor} \cdot [I(\text{first broad peak}) + I(\text{second broad peak})] + (\text{linear background}) \quad (6.3)$$

where the factor is independent of the diffraction angle and the intensities of the two broad peaks are those obtained by fitting the nanocrystalline sample. Here the tungsten carbide peaks were subtracted from the experimental amorphous pattern. We have applied the same fitting procedure to our 11nm $\text{Fe}_{50}\text{Ti}_{50}$ sample obtained by milling elemental powders. The result, shown on figures 6.13, 6.14, and 6.15, also indicates that a significant portion of the sample is amorphous, though the comparison is not as good as that with the 6nm sample. We then used the experimental pattern from the amorphous phase itself to fit the data from the 11nm sample (figure 6.16). The fit is not as good as the one with a broad peak but it is still much better than

the fit with a single sharp peak. From the partial intensity of the amorphous phase obtained with such a fit it is possible to obtain the amount of amorphous phase contained in nanocrystalline samples. The same scattering power is assumed for both the crystalline and amorphous phases.

The crystalline peaks obtained with our diffractometer were not perfectly symmetric, especially at low angles where it interferes most with the evaluation of the amorphous background. Figure 6.17 shows the (110) peak of coarse-grained iron-titanium. The high-angle tail is more intense than the low-angle tail. The high-angle tail is in the same region as the main maximum of the amorphous background. This overlap resulted in an over-estimation of the amorphous content by our normal fitting procedure. In order to circumvent this problem we fitted the crystalline peaks in the X-ray patterns samples which contained some amorphous phase with a convolution of a Lorentzian function with the experimental peak of the coarse-grained sample, as explained in appendix A.2. The fit for the same 11nm Fe₅₀Ti₅₀ sample is shown on figure 6.18. We see that the agreement is as good as that of figure 6.14 which involved a broad peak to mimic the first maximum of the amorphous phase. That broad peak was displaced towards higher angles compared to the experimental amorphous pattern. The integrated intensity of the amorphous component is visibly less than that obtained by using a symmetric function for the crystalline peak (figure 6.16). This shows that if a symmetric function were to be used for the crystalline peak, the amount of amorphous phase would be overestimated. We calculated an amorphous content of 25 percent for the 6nm sample and 12 percent for our 11nm samples.

In the calculation of the crystallite size and strain values from the (110) and (220) reflections we corrected for the amorphous signal in order to obtain the true position, intensity, and width of the (110) peak. There was however little difference with values obtained without the correction except for the 6nm sample from L. Zaluski. In this case the correction makes the crystalline (110) peak sharper and the size obtained with this is 7.5nm. This is still close to the 6nm value. The order parameter S was calculated using the (100) and (200) peaks in order to exclude undesirable influences from the (110) peak. The peak areas of the original and corrected patterns for the 11nm sample are displayed in table 6.1. The corrections with a broad peak (sum of

Lorentzian and Gaussian peaks) and the amorphous experimental pattern both make the areas closer to the values expected for equilibrium FeTi. Our experimental values for coarse-grained FeTi are from samples milled 2 to 5 minutes (in order to have powders). The intensities they have for the (200) and (211) are too high compared to the calculated values. We think this is due to a preferential orientation of the powders. For such samples milled a very short time the crystallite size reduction process is anisotropic. The domain size obtained from the (200) and (400) peaks give results similar to the ones given by the (110) and (220) peaks for long milling times. In the case of short milling times, the (h00) peaks give a domain size twice as large as for the [hh0] direction.

As explained in the preceding chapter, we were able to improve our sample preparation technique and decrease the oxygen content of the arc-melted ingots and, consequently, the sample obtained by milling these FeTi ingots. This also resulted in a reduced amount of amorphous phase. These samples with minimal oxygen content were used in hydrogen storage experiments: the coarse-grained sample (milled only 2 minutes), had 0.29 atomic % of oxygen and the nanocrystalline sample 1.38 atomic %. The amount of amorphous phase correlates well with oxygen content.

In figure 6.19 we give the amorphous content as a function of oxygen contained in the iron oxide mixed with the metallic Fe and Ti powders (from figure 6.7). There is more oxygen from the surface of Fe and Ti powders and, possibly, some extra oxygen contamination during milling. The lowest point at 0% corresponds to the same sample shown at the bottom of figure 6.6, with 2.3 atomic % oxygen (as determined with the Leco O₂/N₂ analyzer).

For the milling conditions we have used, the ratio of amorphous content over oxygen content is 10 ± 1.5 (figure 6.19).

If we look at the crystallite size (figure 6.20) and strain (figure 6.21) data, we see that the samples with x=0 have 12nm crystals and a strain value of 1.5% (there is two data points at x=0). As the oxygen content is increased, therefore the fraction of amorphous phase, the crystals become smaller and reach a diameter as low as 6nm. The average strain falls to 0.3% for x=6. Keeping in mind that these values are averages for the whole sample, we propose that 11-12nm is the smallest diameter

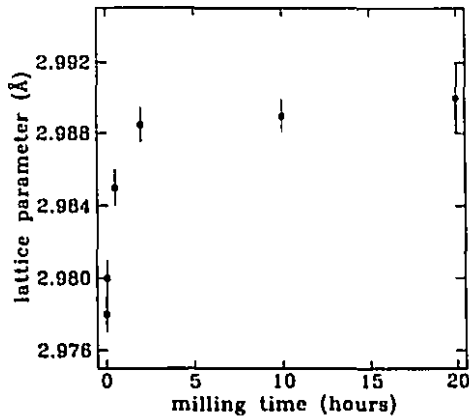


Figure 6.22: Lattice parameter of $\text{Fe}_{50}\text{Ti}_{50}$ (intermetallic compound) as a function of milling time.

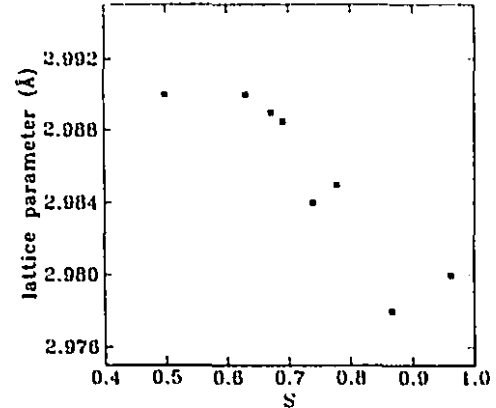


Figure 6.23: Lattice parameter as a function of long-range order parameter S .

for which a nanocrystal can exist with a highly distorting defect inside (such as a dislocation or oxygen impurity, and that smaller crystals are free of such defects. Chemical disorder of Fe and Ti sites is possibly still present at very low sizes. The minimum possible crystallite size is close to 5-6nm.

6.3 Lattice parameter

The lattice parameter of the intermetallic compound increases slightly during milling (figure 6.22). We are not certain about the cause for such a change. An expansion of the lattice parameter has been observed before the amorphization of certain materials [35] by ball milling, when the crystallite size reaches a critical value. Another possibility has to do with impurities. An important fact is that the low oxygen sample milled 20 hours has a lattice parameter of 2.984\AA instead of 2.990\AA for the other samples. However it might be related to its long-range order parameter which is higher than the samples with higher oxygen content ($S=0.74$ compared to $S=0.65$ as in figure 6.5). If we plot the lattice parameter as a function of S (figure 6.23), regardless of milling time and oxygen content, there seems to be a good relation between the two quantities.

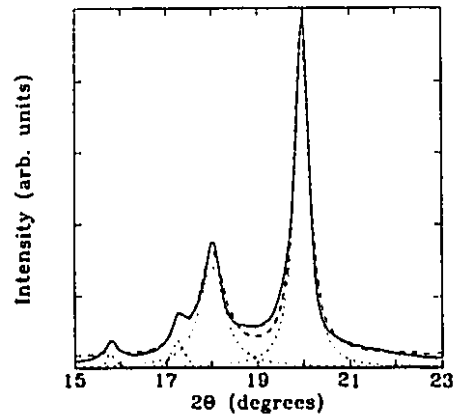


Figure 6.24: X-ray pattern fit of elemental powders (composition $\text{Fe}_{50}\text{Ti}_{50}$) milled 2 hours using 4 sharp peaks.

6.4 Mechanically alloyed $\text{Fe}_{50}\text{Ti}_{50}$

Figure 6.6 shows the X-ray data for the equiatomic mixture of elemental powders after different milling times. There is a rapid decrease in titanium content in the first two hours of milling. There is also a broadening of both Ti and Fe peaks. After 5 hours titanium is almost completely transformed and there is a new peak appearing between the main Fe and Ti peaks. After 10 hours no iron peak is visible. The only crystalline phase is cubic with a small peak at 13.5 degrees indicating partial long-range order. Milling ten more hours does not bring any significant change. The rapid transformation is consistent with the fact that only 3 atomic % of iron is sufficient to transform hexagonal close-packed titanium into body-centered cubic titanium ($\beta\text{-Ti}(3\text{at.}\%\text{Fe})$) [104].

Figure 6.24 illustrates our attempt to fit the pattern from the sample milled 2 hours with 4 peaks between 15 and 23 degrees. The result is clearly unsatisfactory: there is intensity not accounted for at 19 degrees and the main titanium ($\sim 18^\circ$) and iron ($\sim 20^\circ$) peaks obtained from the fit have intensities too high with respect to the other peaks at higher angle.

From the area of the high angle Fe and Ti peaks it is possible to estimate the amount of pure iron and pure titanium left by comparing them with their value for the mixture not yet milled. The sample milled 2h contains 14 at.% $\alpha\text{-Ti}$ and 40at.%

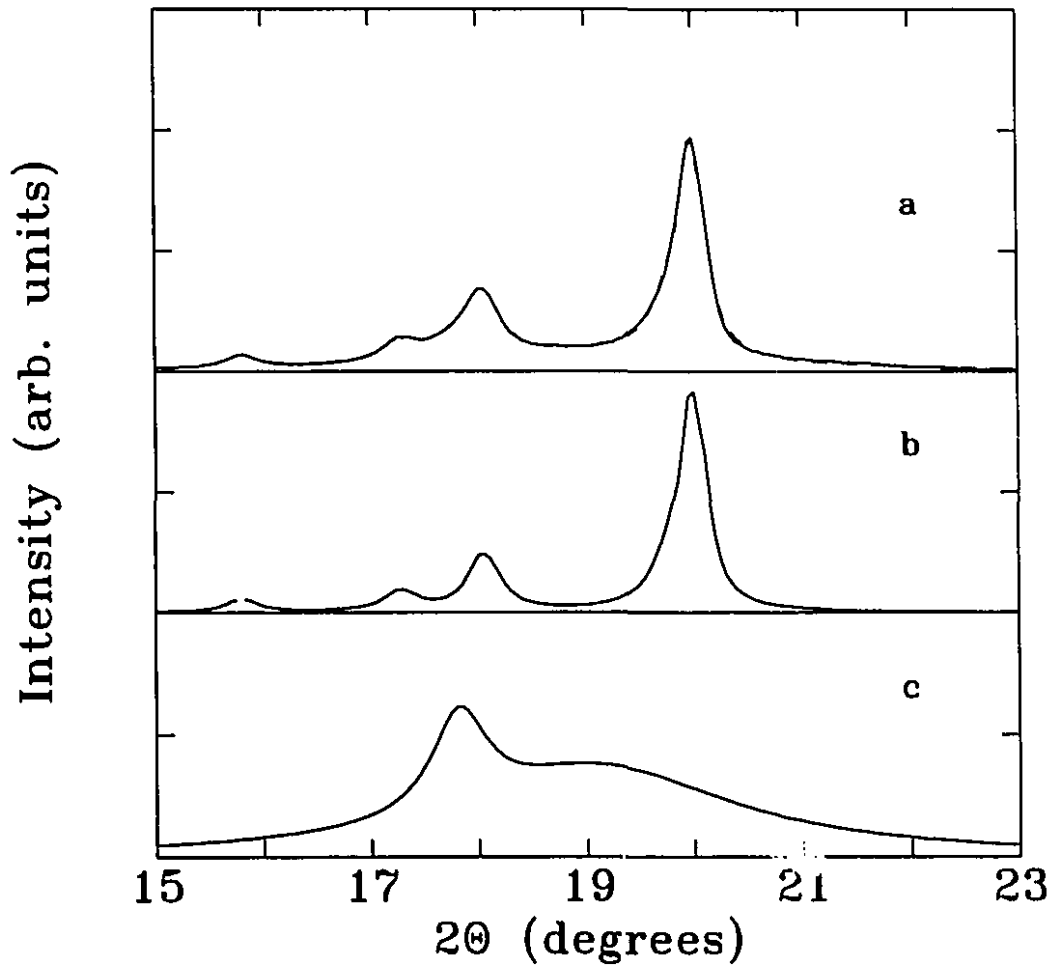


Figure 6.25: X-ray pattern fit of elemental powders (composition $\text{Fe}_{50}\text{Ti}_{50}$) milled 2 hours using (in addition to the 3 α -Ti peaks and the Fe peak) a β -Ti(Fe) peak and a very broad peak corresponding to an amorphous phase. The experimental intensity is the solid line in a. The dashed line on the same graph is the total calculated intensity. The intensity from α -Ti and Fe is shown in b. The intensity from β -Ti(Fe) and amorphous Fe-Ti is shown in c. The scale of c is five times smaller than the scale of a and b.

α -Fe. This gives $\text{Fe}_{20}\text{Ti}_{80}$ as the average composition of the reaction products. A bcc phase with such a composition would have a lattice parameter of 3.124\AA (using results from splat-cooled samples [67]) and a (110) peak at about 18.5° . There is no peak visible at this angle. Furthermore, in figure 6.24, we see there is signal not accounted for by the four peaks throughout the angle interval shown.

A more likely possibility is that we have a mixture of β -Ti and amorphous Fe-Ti. We successfully fitted the pattern of $\text{Fe}_{50}\text{Ti}_{50}$ milled 2 hours using a peak at 17.75° and a very broad peak around 19° to mimic the signal from an amorphous phase. The results is shown on figure 6.25. The calculated signal is much closer to the experimental data than the fit with only four peaks. All the peak parameters were optimized by the computer program: position, intensity, and width. The signal from the bcc phase and the amorphous phase are shown at the bottom of figure 6.25. The y-axis has its scale multiplied by five compared to the upper half. One might of course question the validity of our procedure, arguing that it is possible to add as many peaks a needed until a good fit is found. Since the intensity of the Fe and Ti peaks between 15 and 23 degrees are known from the higher angle peaks, we know there is extra intensity coming from at least one phase which is a reaction product. Also, on figure 6.24, we see that some of this extra signal extends to both ends of the x axis. The program tries to account for it using the linear background which, of course, cannot replace the faraway tails of a broad peak. Using only this extra broad peak leads the program to give too high intensities to the titanium peaks at 17.5 and 18 degrees. Another argument is that the position of the bcc peak, 17.76° , gives a lattice parameter of 3.25\AA , exactly what is found for bcc β -Ti(3at.%Fe), a very plausible result. In addition to all this, the peak intensities for the 3 Ti and the Fe peak given by the fit of figure 6.24 are much closer to what they should be, according to the high angle peaks than what is found by fitting the pattern with four peaks. From these high angle peaks the intensities of the peaks Ti(100), Ti(002), Ti(101), and Fe(110) should be 590, 836, 3101, and 8971 counts respectively. The 4-peak fit gives 242, 637, 6786, and 12152. The 6-peak fit in turn yields 583, 929, 2624, and 10515. These facts strengthen our conviction that β -Ti(Fe) and amorphous Fe-Ti are present as intermediate reaction products.

The match between calculated and experimental intensities is less good on each side of the Fe(110) peak. This is due to the asymmetry of the Fe peaks at this stage of milling. We think this asymmetry originates in the diffusion of a certain amount of titanium into iron, expanding the lattice of some of the iron still present. The positions of the iron peaks are indeed shifted to lower angles after 2 hours of milling and the average lattice parameter obtained from these is 2.873Å instead of 2.869Å for pure iron. In the last fit we had to use an asymmetric peak for the (100) reflection of iron. A more precise shape analysis with some link to diffusion processes would of course be desirable. The final lattice parameter of $\text{Fe}_{50}\text{Ti}_{50}$ is 2.982, the crystallite size 12nm.

6.5 Amorphous $\text{Fe}_{67}\text{Ti}_{33}$

The free energy curves (figure 2.15) suggest there is a rather stable amorphous phase at the $\text{Fe}_{67}\text{Ti}_{33}$ composition. We have milled a mixture of elemental powders with this composition and the results are displayed in figure 6.26. We obtain the same rapid transformation of titanium while iron peaks show little change in the early stages of milling. The apparent increase of intensity of the second Ti peak with respect to the other Ti peaks in the X-ray pattern of the sample milled 30 minutes is due to the shape of this sample. At that stage of milling we obtain metallic flakes. In order to make a good sample for diffraction, these flakes were put flat in a resin and polished. It seems that the sample had a certain degree of texture. The scanning electron micrographs (figure 6.27) of a cross section of one of these flakes shows the typical lamellar aspect of mechanically alloyed samples. This is one argument in favor of comparing ball-milled materials with multilayers of the same elements.

After 2 hours of milling there is little titanium left while iron peaks are still very strong. After 5 hours the intensity from the amorphous phase becomes dominant. After 20 hours the reaction is complete. Peaks from tungsten carbide are highly visible in this case because the absolute intensity of amorphous samples is low (while their integrated intensity is the same as that of crystalline samples). Cocco et al. have already milled $\text{Fe}_{67}\text{Ti}_{33}$, however they did not obtain a completely amorphous material [16].

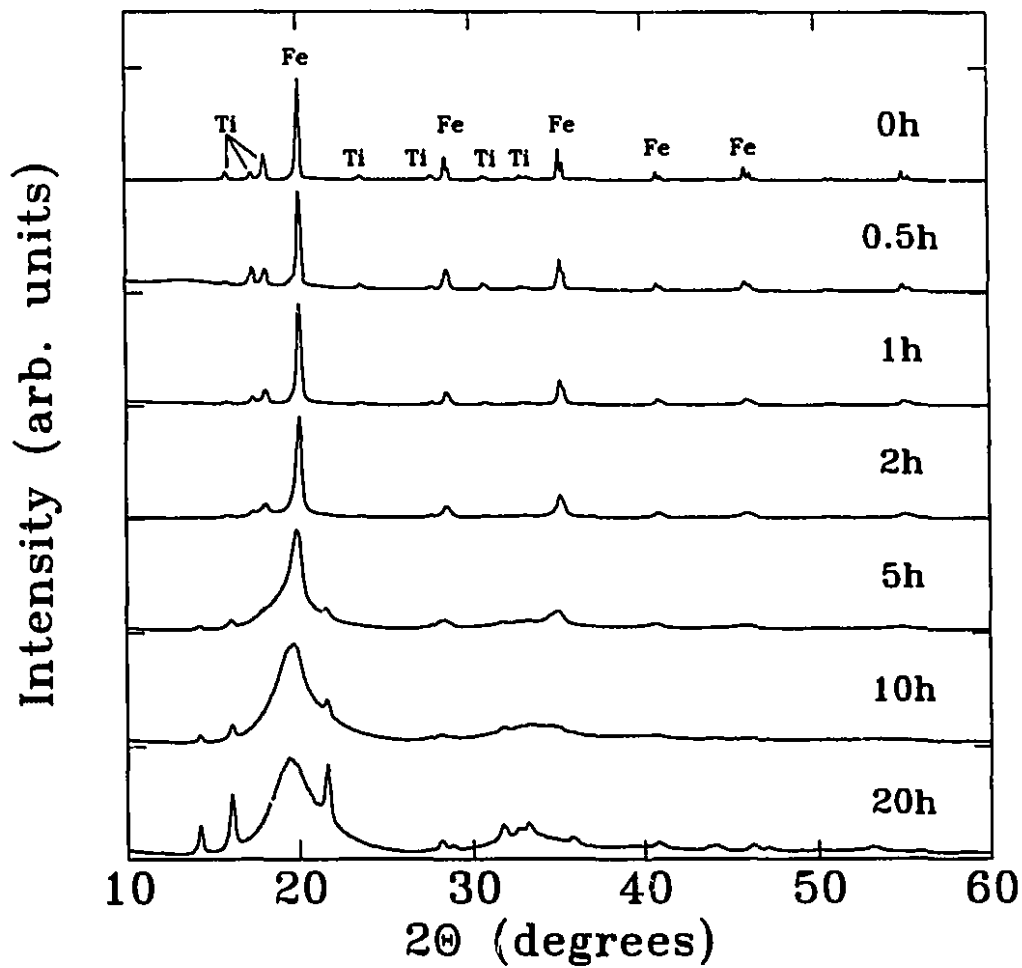


Figure 6.26: X-ray pattern of Fe₆₇Ti₃₃ (elemental powders) after 0, 0.5, 1, 2, 5, 10, and 20 hours of milling.

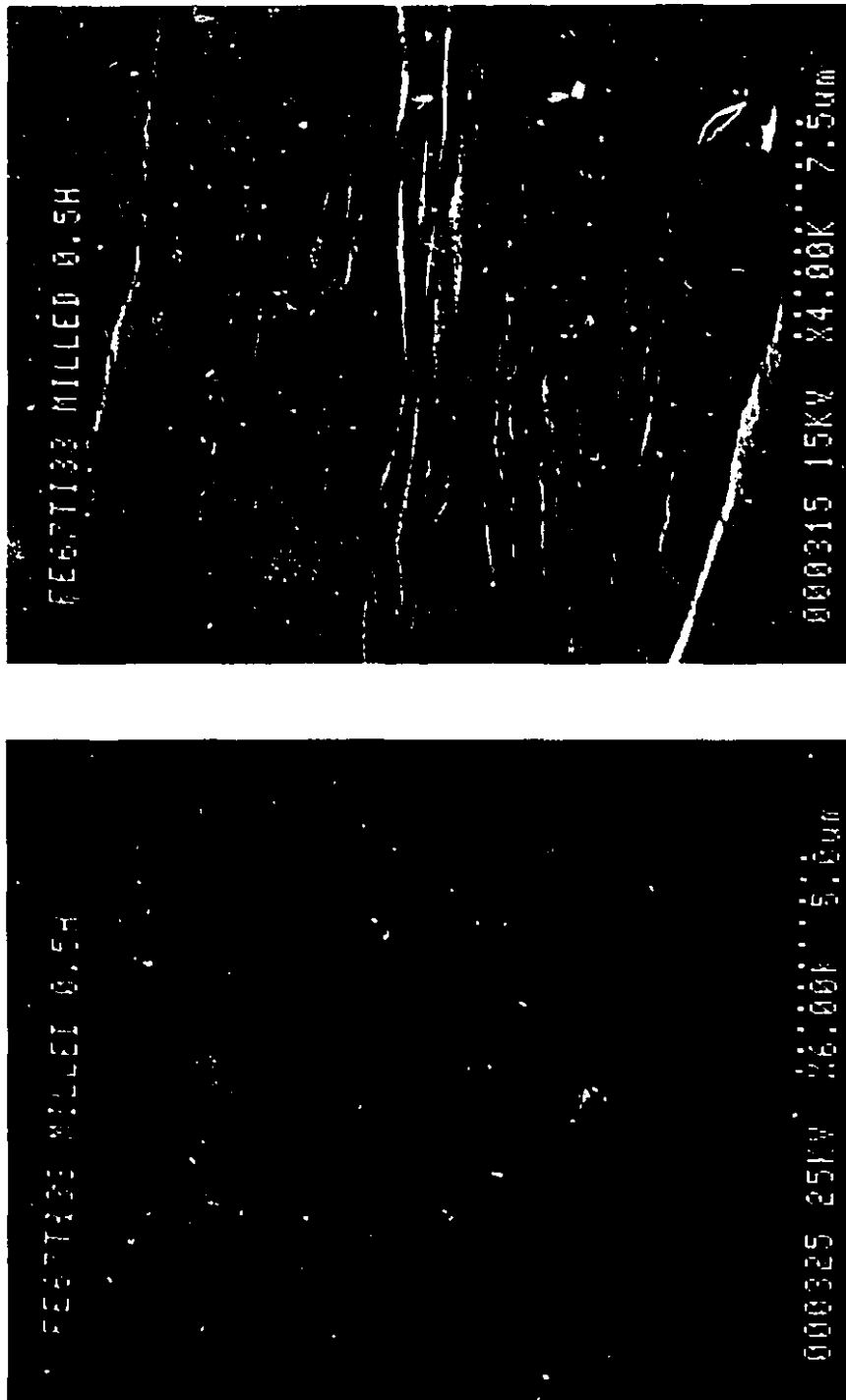


Figure 6.27: Scanning electron micrographs of Fe₆₇Ti₃₃ (elemental powders) milled 0.5 hour.

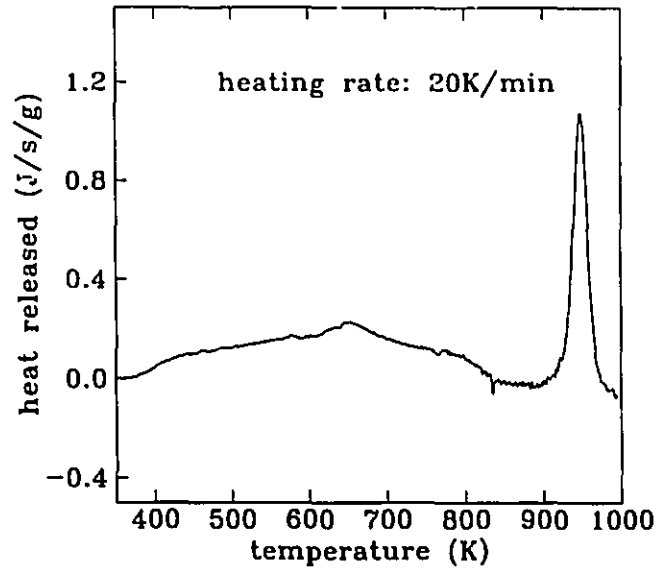


Figure 6.28: DSC scan of Fe₆₇Ti₃₃ milled 20 hours.

From the DSC scan (figure 6.28) we found the enthalpy of crystallization to be 85.6 J/gram and the crystallization temperature 948K at 20 K/min. There is also a large heat release from 375K to 825K, 184J/gram, which is likely the result of some irreversible relaxation phenomenon and, possibly, a redistribution of oxygen into a more stable chemical state. Using the area of X-ray peaks to estimate the amount of tungsten carbide, we find for the crystallization enthalpy of the pure amorphous phase 93.0 ± 1.9 J/g (4.95 ± 0.10 kJ/mol). This is comparable to the crystallization enthalpy of vapor-quenched amorphous Fe₆₆Ti₃₄ films (4.57 kJ/mol) [95].

6.6 Nanocrystalline Fe₄₀Ti₆₀

The milling of Fe₄₀Ti₆₀ proceeds in a similar fashion as Fe₆₀Ti₅₀. After 5 hours of milling however we see a major peak corresponding to the new cubic phase while titanium and iron peaks are still well visible. The lattice parameter after 20 hours of milling is 2.998Å. From this and using Vegard's law we find that the average composition of nanocrystals in this sample is Fe₄₆Ti₅₄. The long-range order parameter is 0.54. The maximum possible for this composition is $S = 0.8$. The final crystallite

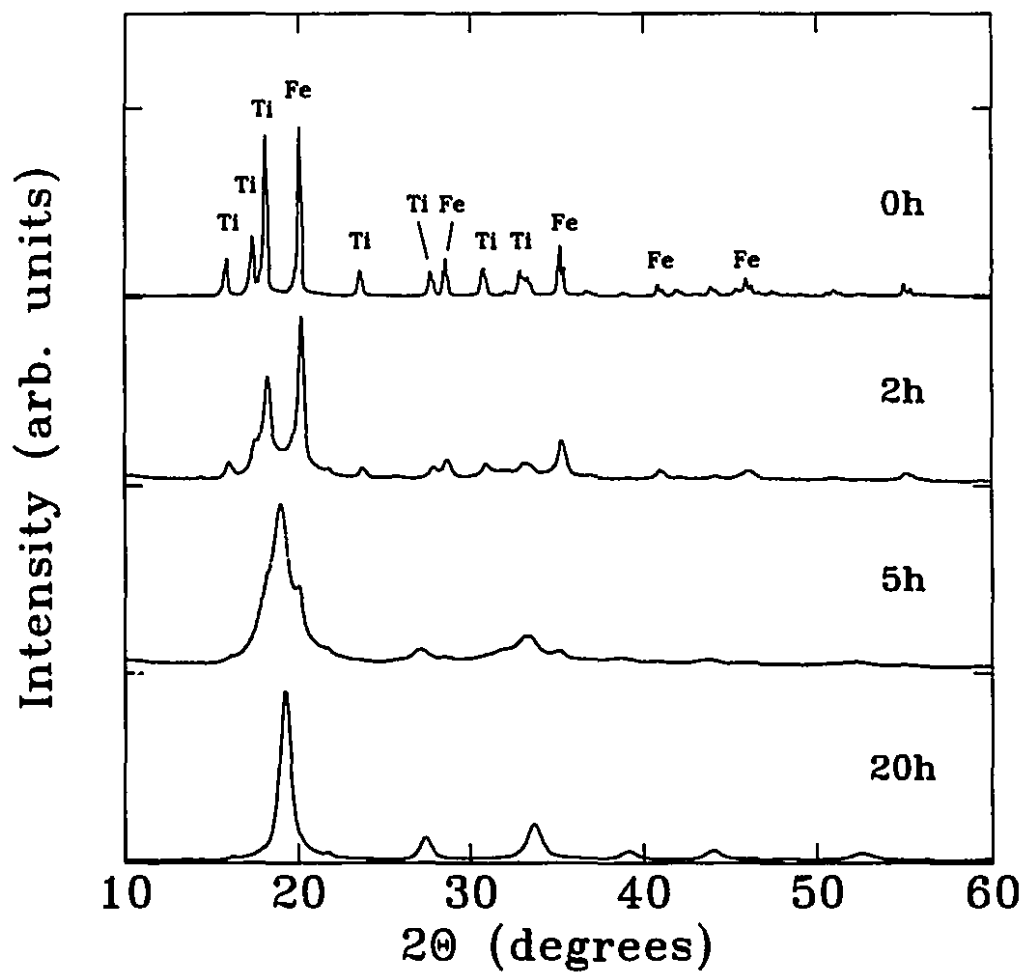


Figure 6.29: X-ray pattern of Fe₄₀Ti₆₀ (elemental powders) after 0, 2, 5, and 20 hours of milling.

size is 11nm and the strain 1.56%.

6.7 General discussion

Although the technique of ball milling is simple in its design, the modifications it produces on materials can be very complex. The analysis of transformations is also hampered by the fact that we do not know precisely what temperature is to be considered. An agreement seems to be emerging in the research community that the local temperature increase during collisions does not usually exceed 200K [19, 35]. It must be emphasized however that transformations occurring during ball milling are not simply the result of repeated heat transfers to the material and that mechanical effects have to be considered [90].

In the case of the FeTi intermetallic compound, ball milling changes the material on the macroscopic, microstructural, and structural (atomic) level. The first—obvious—effect is that the ingot made by arc-melting is rapidly crushed during the first minutes of milling. After less than one hour of milling the material is completely transformed into a powder. Scanning electron microscopy of the final powder (20 hours of milling) shows fine powder particles (1-10 μ m), but most are packed into large agglomerates. We do not expect the macroscopic aspect of the material to have any influence on the final phases produced by milling.

The microstructural evolution during milling is essentially a reduction of the crystallite size (figure 6.2). Microscopic observations by A. Zaluska [103] of FeTi at intermediate milling times show grains divided by low-angle grain boundaries. We suspect that dislocations caused by milling-induced mechanical deformations pile up into low-angle grain boundaries. The misorientation of the smaller sub-grains so-produced supposedly increases with further milling, leading to completely separate crystallites. The refinement of the crystallites is expected to change the relative stability of the FeTi compound, for the same reason that a refinement in crystallite size reduces the melting temperature of metals [13, 14, 78]. In terms of free energies, we might say that the free energy of a nanocrystalline material is increased by the high density of grain boundaries. If the free energy is increased beyond the free energy of some other phase, a phase transformation may occur. It might be argued that

one should not analyze ball milling with equilibrium thermodynamics, however since the temperature increase during collisions is rarely sufficient to produce the phase transformations observed, the process can be seen as one where the free energy of the material is gradually increased by the slow introduction of defects. In the case where no phase transformation takes place, the crystallite size reaches a constant value after just a few hours of milling (there is no significant difference between samples milled 10 and 20 hours). Further reductions in crystallite size which might have occurred after much longer milling times (~ 100 hours) would likely be due to impurities coming from the wear of the milling tools. The final crystallite size that can be reached by ball milling has recently become an important subject in research on ball milling [55, 35, 65]. A few models have been proposed but there is no consensus on that matter.

This leads us to discuss the structural defects introduced by milling, such as chemical disorder. Chemical disorder is directly observed in our experiments. In the literature concerning the FeTi compound there is usually no data given on chemical disorder. With the equipment available and using a sufficiently long counting time we were able to follow the (100) peak of FeTi and obtain values of the long-range order parameter with a reasonable precision. From the values obtained after 20 hours of milling, we see that the location of Fe and Ti atoms is far from being random. An order parameter $S = 0.65$ means that the probability of finding the right atom on any site is approximately 0.8. Looking at the free energies of the amorphous and bcc phase (figure 2.15), we see that in order to raise the free energy of the FeTi compound close to that of the amorphous phase it is necessary to decrease the long-range order parameter close to zero.

There is a partial amorphization of the compound during milling. But our measurements of oxygen content and our milling experiments on $\text{Fe}_{50-\frac{x}{2}}\text{Ti}_{50-\frac{x}{2}}\text{O}_x$ clearly show that any amorphization at the $\text{Fe}_{50}\text{Ti}_{50}$ composition after long milling times is directly the result of the oxygen present in samples. We believe that the evidence given by the X-ray analysis, especially the comparison between the sum of the broad peaks obtained by fitting the 6 nm sample of L. Zaluski and the experimental X-ray pattern of fully amorphous $\text{Fe}_{45}\text{Ti}_{45}\text{O}_{10}$ is convincing. Using a convolution of

a Lorentzian function and the experimental peak function from the coarse-grained sample, we were able to show that the difference between the calculated pattern and the amorphous pattern in figure 6.12 (the displacement toward higher angles of the first maximum) comes from the asymmetric shape of low-angle diffraction peaks. We did not determine the exact mechanism by which oxygen initiates amorphization but we expect it is related to the strong bonds oxygen can establish with iron and titanium and the distortion this would produce in the vicinity of oxygen atoms. In order to reduce the associated strain these disordered clusters probably assemble into larger amorphous regions, otherwise the amorphous phase would not be visible by transmission microscopy [104].

The very large strain observed after 20 hours of milling can be due to several defects: chemical disorder, dislocations, oxygen impurities, and stress near grain boundaries. Some answers will come later as we look at the effect of the activation treatment. However we may already mention that oxygen impurities can probably not be linked to these high strains because the low-oxygen 12 nm sample has a strain level, $1.48 \pm 0.07\%$, as high as other 12 nm samples with higher oxygen content. Microscopic observation would be necessary to determine if dislocations are present or if strain is important near grain boundaries. The presence of dislocations is very likely, given that our materials are produced by mechanical deformations. The increase in lattice parameter observed during milling appears to be related to chemical disorder caused by milling.

Concerning the stability of defects in the nanocrystalline microstructure, the results on crystallite size and strain level in milling experiments on Fe-Ti-Fe₂O₃ mixtures are particularly interesting. As the average crystallite is reduced below 10 nm, the average strain level is strongly reduced too (figures 6.20 and 6.21). This means that below a certain crystallite size a defective structure really becomes unstable with respect to the amorphous phase. This goes along the other changes in stability associated to the nanocrystalline microstructure, such as the reduction in melting temperature of nanometer-sized metals.

The milling experiments on mixtures of pure Fe and Ti powders proceed in a very different fashion. On a macroscopic level, the pure metallic powders are ductile and

form flakes in the first hour of milling. The flakes obtained after half an hour of milling are wide (~ 1 mm) and very thin compared to those milled one hour which are much more "powder-like". The final product is a powder identical to that made by milling the intermetallic compound. On a different level, a lamellar microstructure (figure 6.27) is obtained in the early stages of milling. This microstructure is simply the result of repeated pressing and cold welding during collisions. It provides numerous clean interfaces for the reaction between the two metals.

The reaction between Fe and Ti proceeds by the transformation of hcp α -Ti into bcc β -Ti(3 at. % Fe) followed by gradual enrichment of this bcc structure. The main peak of bcc Ti(Fe) is very difficult to isolate because it is superposed to α -Ti peaks. We were able to show however that the X-ray spectrum of $\text{Fe}_{50}\text{Ti}_{50}$ milled 2 hours (figure 6.24) cannot be fitted with only four peaks (for α -Ti and Fe) and that a good fit may be obtained using an extra peak for β -Ti(Fe) and a broad peak from an amorphous phase. There is also some diffusion of Ti into bcc α -Fe. In a previous article [104] our group has shown, on the basis of transmission electron microscopic observations, that the transformations from hcp α -Ti to bcc β -Ti(3 at. % Fe) occurs at α -Ti grain boundaries. If we follow the free energy of bcc Ti(Fe) (figure 2.15), we see that it becomes higher than that of amorphous Fe-Ti at a concentration of 30 atomic percent iron. A transformation would have been possible, had the bcc structure not reordered. The gradual enrichment of bcc Ti(Fe) does not appear in the X-ray patterns of $\text{Fe}_{50}\text{Ti}_{50}$ after increasing milling time because this process occurs for the most part between 5 and 10 hours of milling and we did not make an X-ray scan between these two periods. However a bcc phase is very visible in the X-ray pattern of $\text{Fe}_{40}\text{Ti}_{60}$ milled five hours. We see a peak at an intermediate position, slightly left of the (100) peak of the final $\text{Fe}_{40}\text{Ti}_{60}$ bcc phase obtained after 20 hours of milling.

As to the amorphous phase for which there is evidence in X-ray patterns of $\text{Fe}_{50}\text{Ti}_{50}$ it is not clear whether it is a temporary reaction product coming from interdiffusion of Fe in Ti such as that forming in annealed Fe-Ti multilayers [97] or just the result of oxygen present on the surface of the initial powder. In the case of multilayers, the amorphous phase is formed because the formation of the more stable crystalline

structure is kinetically suppressed. Issues of interface coherency also arise. It is very difficult to understand how an amorphous phase could form at the same time bcc β -Ti does during ball milling. Unfortunately the experimental evidence here is very indirect.

In the X-ray pattern of $\text{Fe}_{40}\text{Ti}_{60}$ milled 5 hours the (101) peak of α -Ti (third peak from the left in figure 6.29) is far too intense compared to the (002) peak (second from the left), indicating the presence of β -Ti(Fe). At the same time the far reaching shoulder on the high-angle side of the Fe (110) peak indicates the presence of an amorphous phase. If the amorphous phase present at intermediate milling times (2-5 hours) was attributed to a kinetic suppression of formation of a more stable bcc phase, the relative amount of amorphous material and bcc Ti(Fe) might be explained by the different average composition and the rate of diffusion, both leading to a different distribution of concentration.

In next chapter we will examine the change in samples after activation and repeated hydrogen absorption-desorption in order to draw additional conclusions concerning the defects produced by the milling process.

HYDROGEN STORAGE IN BALL-MILLED FE-TI

7.1 Overview of hydrogen storage results

We present in this chapter the equilibrium behavior of five samples: coarse-grained FeTi made by milling the intermetallic compound for two minutes, two nanocrystalline samples made from the intermetallic compound and from elemental powders and called nanocrystalline FeTi and nanocrystalline Fe₅₀Ti₅₀ respectively, nanocrystalline Fe₄₀Ti₆₀ obtained by milling Fe and Ti powders in the 40:60 atomic ratio, as well as amorphous Fe₆₇Ti₃₃ made from powders mixed in the 67:33 atomic ratio. The four latter samples were milled 20 hours.

The pressure-composition isotherm of coarse-grained FeTi prepared by milling an ingot of the intermetallic compound for 2 minutes is shown in figure 7.1. The results are similar to those of Reilly and Wiswall [70]. The total storage capacity is somewhat lower: 0.8 hydrogen per metal atom instead of 0.9. The plateau corresponding to the transformation from the α to the β phase is at the same pressure and extends over

Table 7.1: Pressure of the absorption and desorption plateaus of each crystalline sample (in atmospheres). The midpoint is determined from the arithmetic mean of the logarithm of the two plateaus.

sample	absorption	desorption	midpoint
coarse-grained FeTi	12.6	4.9	7.9
nanocrystalline FeTi	12.1	4.5	7.4
nanocrystalline Fe ₅₀ Ti ₅₀	11.1	4.4	7.0
nanocrystalline Fe ₄₀ Ti ₆₀	3.1	1.7	2.3

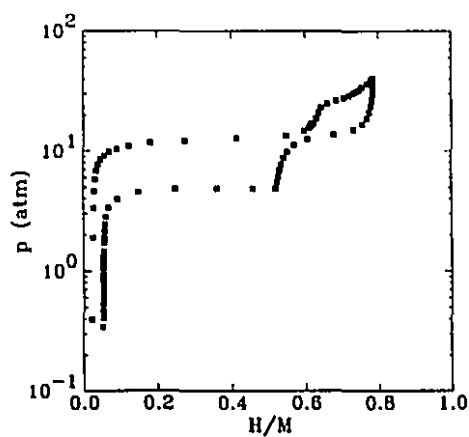


Figure 7.1: Pressure-composition isotherm for coarse-grained FeTi.

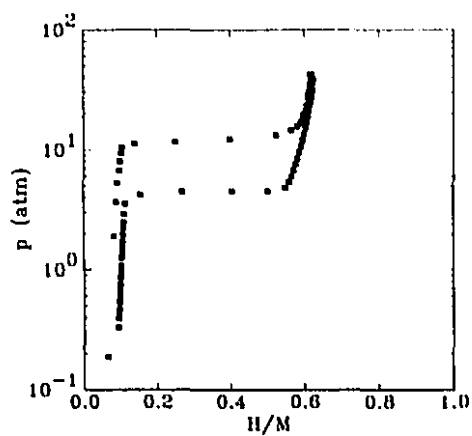


Figure 7.2: Pressure-composition isotherm for nanocrystalline FeTi made from the intermetallic compound FeTi (crystallite size: 12nm).

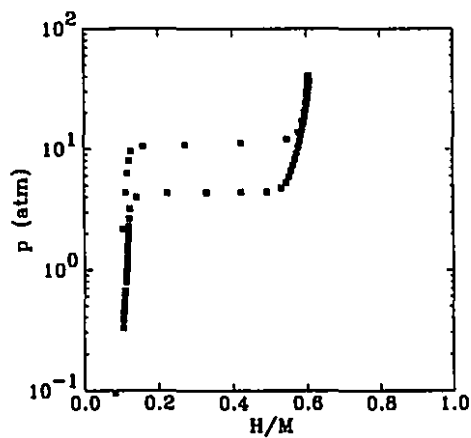


Figure 7.3: Pressure-composition isotherm for nanocrystalline Fe₅₀Ti₅₀ made from elemental powders (crystallite size: 12nm).

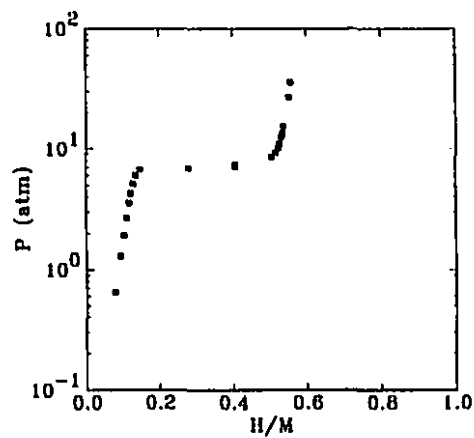


Figure 7.4: Pressure-composition isotherm for nanocrystalline Fe₅₀Ti₅₀ made from elemental powders (crystallite size: 6nm, result taken from [104], absorption only).

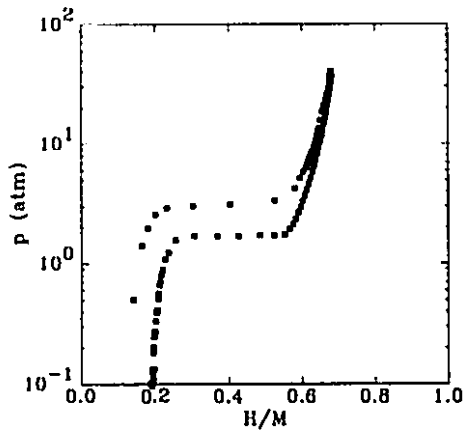


Figure 7.5: Pressure-composition isotherm for nanocrystalline $\text{Fe}_{40}\text{Ti}_{60}$ (crystallite size: 11 nm).

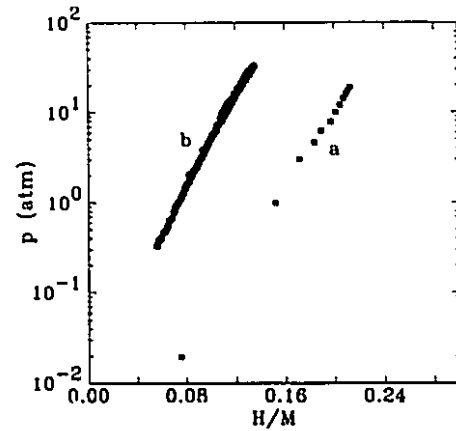


Figure 7.6: Pressure-composition isotherm for amorphous $\text{Fe}_{67}\text{Ti}_{33}$: squares: first storage cycle (absorption only), circles: after repeated storage cycles.

the same composition range. On desorption we find the same dip at $H/M=0.6$, but it is much less pronounced than what is shown in [70]. Such a dip has to be a non-equilibrium feature. There is no transformation to the $\gamma\text{-FeTiH}_{1.90}$ in the pressure range investigated.

The sample obtained by milling the intermetallic compound for 20 hours has a significantly altered pressure-composition isotherm. There is additional solubility before the appearance of the β phase and the total storage capacity is reduced to 0.6. Both plateaus (absorption and desorption) occur at slightly reduced pressure. The other nanocrystalline $\text{Fe}_{50}\text{Ti}_{50}$ sample made from elemental powders has a similar isotherm, the absorption plateau however is found at a pressure slightly lower than in the case of nanocrystalline FeTi. We also show the absorption curve for the 6 nm $\text{Fe}_{50}\text{Ti}_{50}$ sample made by L. Zaluski [104] (figure 7.4).

The nanocrystalline $\text{Fe}_{40}\text{Ti}_{60}$ sample has an isotherm similar to $\text{Fe}_{50}\text{Ti}_{50}$ but the plateau is shifted to a significantly lower pressure. The absorption plateau is at 3 atm and the desorption plateau at 1.7 atm. This is very different from Ti-rich materials made by conventional methods which separate into titanium hydride and FeTi-H [70].

Figure 7.6 shows the pressure-composition isotherm of amorphous $\text{Fe}_{67}\text{Ti}_{33}$ for the first storage cycle and one of the subsequent cycles. The curves are typical of what is

found in amorphous systems. The concentration slowly increases with pressure and there is no miscibility gap. The analysis of the sample retrieved after storage experiments revealed a hydrogen concentration lower than 0.01 hydrogen/metal, confirming that there is indeed a difference between the first and subsequent cycles, and that it is not related to hydrogen being permanently trapped in deep storage sites (with very low energies). The change observed is therefore related to a relaxation of the amorphous structure during the first cycle. There is no change in storage behavior after the second cycle. The displacement of the curve toward higher pressures must be related to a densification of the structure during the first storage cycle. The steeper slope indicates a narrowing of the site energy distribution.

It is very interesting to note that the intermetallic compound of the same composition Fe_2Ti does not absorb hydrogen. The structure of amorphous alloys, with a wide variety of local coordinations between nearest-neighbour atoms, explains this striking difference in storage properties between two materials having the same chemical composition. Interstitial sites with varying numbers of Ti and Fe neighbour atoms are expected to exist, each with different binding energies.

7.2 Activation

As in the case of polycrystalline FeTi with large crystallites, our coarse-grained material with an average crystallite size of 29 nm required a long activation procedure. Precisely, ten activation cycles were necessary to obtain reproducible storage results. In the case of nanocrystalline samples, a second activation cycle did not change the storage results from those obtained after a first cycle.

The amorphous $\text{Fe}_{67}\text{Ti}_{33}$ sample had very slow kinetics. In absorption experiments at 50atm, equilibrium was established only after 20 hours, compared to approximately 30 minutes for nanocrystalline materials. In order to measure pressure-composition isotherms we had our amorphous sample treated with palladium by L.Zaluski in the same way as for Mg_2Ni [105, 107]. The amount of palladium introduced in the form of clusters on the amorphous powder is less than one weight percent and the palladium is not dissolved in the amorphous matrix. This procedure allowed the study of the amorphous material by greatly accelerating absorption and desorption. In addition

Table 7.2: Crystallite size of samples after activation and repeated hydrogen absorption-desorption cycles (in nanometers). For coarse-grained FeTi, the linear regression led to the origin of the axes with the error bar spanning positive and negative values. The domain size along the [h00] direction is too large to be accurately determined from the width of X-ray peaks.

sample	reflections	before H cycling	after activation and H cycling
coarse-grained FeTi	110,220	29 ± 10	83 ± 52
	200,400	very large	very large
nanocrystalline FeTi	110,220	12 ± 2	13 ± 2
	200,400	7 ± 1	15 ± 3
nanocrystalline Fe ₅₀ Ti ₅₀	110,220	12 ± 2	12 ± 2
	200,400	7 ± 1	12 ± 2
nanocrystalline Fe ₄₀ Ti ₆₀	110,220	11 ± 2	10 ± 1
	200,400	6 ± 1	17 ± 4

to this, the material did not require any activation.

7.3 Microstructure and phase stability

Preserving the nanocrystalline structure during the activation and the hydrogen storage cycles is a critical aspect in research on these materials. The crystallite size, measured along the [h00] and [hh0] directions, are collected on table 7.2. The 2 minutes of milling to which the coarse-grained sample was subjected were sufficient to reduce the crystallite size to 29 nm. However the material obtained after activation and hydrogen cycling has a much larger crystallite size (83 nm). The large uncertainty for large sizes is typical of this method of size determination. The size along the [h00] direction is very large, indicating that the growth of the FeTi structure proceeds preferentially along this direction. The final size is the one which is representative of the material studied in the equilibrium storage experiments, not the initial size (as-milled).

The nanocrystalline FeTi sample is stable, at least when we consider the size along the [hh0] direction. The initial and final size are equal (considering the uncertainty).

Table 7.3: Strain values for samples after activation and repeated hydrogen absorption-desorption cycles.

sample	reflections	before H cycling	after activation and H cycling
coarse-grained FeTi	110,220	0.22 ± 0.05	0.71 ± 0.05
	200,400	0.31 ± 0.05	0.65 ± 0.06
nanocrystalline FeTi	110,220	1.48 ± 0.07	0.14 ± 0.07
	200,400	0.29 ± 0.08	0.15 ± 0.07
nanocrystalline Fe ₅₀ Ti ₅₀	110,220	1.51 ± 0.07	0.18 ± 0.07
	200,400	0.31 ± 0.08	0.05 ± 0.07
nanocrystalline Fe ₄₀ Ti ₆₀	110,220	1.56 ± 0.07	0.23 ± 0.07
	200,400	0.37 ± 0.08	0.71 ± 0.07

Table 7.4: Amorphous content, lattice parameter d , and long-range order parameter S of samples as-milled.

sample	amorphous content (%)	d (Å)	S
coarse-grained FeTi	0.0	2.978	0.96
nanocrystalline FeTi	5.1	2.984	0.74
nanocrystalline Fe ₅₀ Ti ₅₀	9.7	2.982	0.65
nanocrystalline Fe ₄₀ Ti ₆₀	9.8	2.998	0.54

Table 7.5: Amorphous content, lattice parameter d , and long-range order parameter S of samples after activation and repeated hydrogen absorption-desorption cycles.

sample	amorphous content (%)	d (Å)	S
coarse-grained FeTi	0.0	2.978	0.88
nanocrystalline FeTi	5.4	2.977	0.91
nanocrystalline Fe ₅₀ Ti ₅₀	6.7	2.978	0.86
nanocrystalline Fe ₄₀ Ti ₆₀	6.2	2.987	0.91

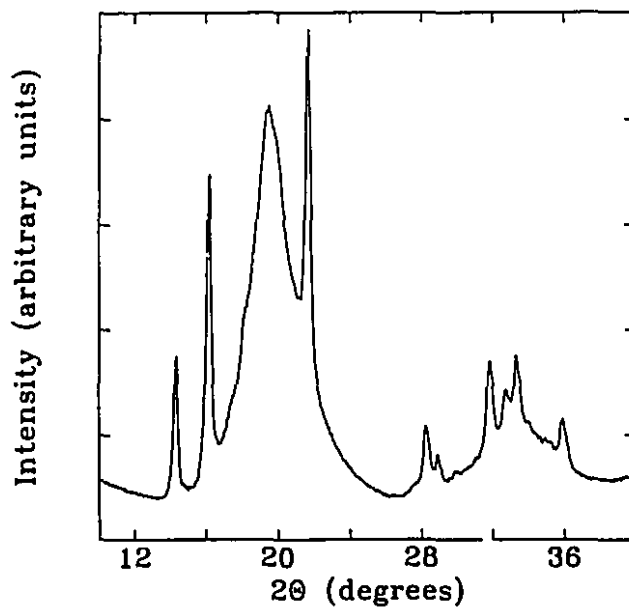


Figure 7.7: X-ray diffraction pattern of amorphous $\text{Fe}_{67}\text{Ti}_{33}$ treated with palladium. The crystalline peaks are those of tungsten carbide impurities. There is not enough palladium to produce visible peaks.

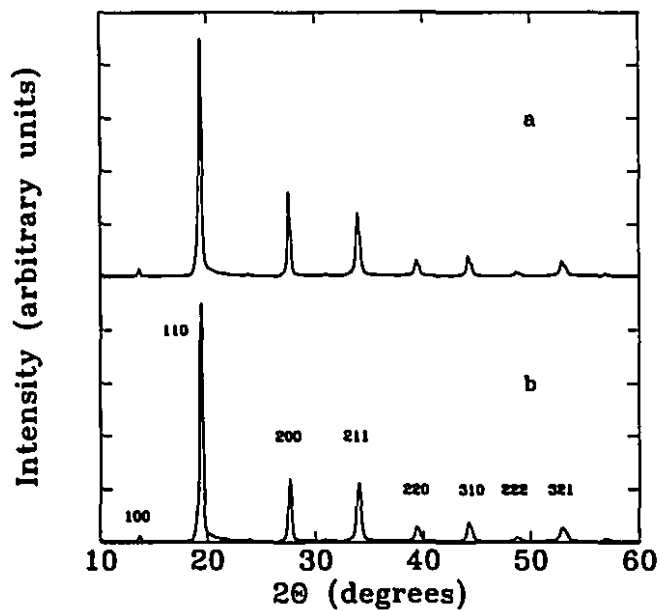


Figure 7.8: X-ray diffraction pattern of coarse-grained FeTi before (a) and after (b) storage experiments.

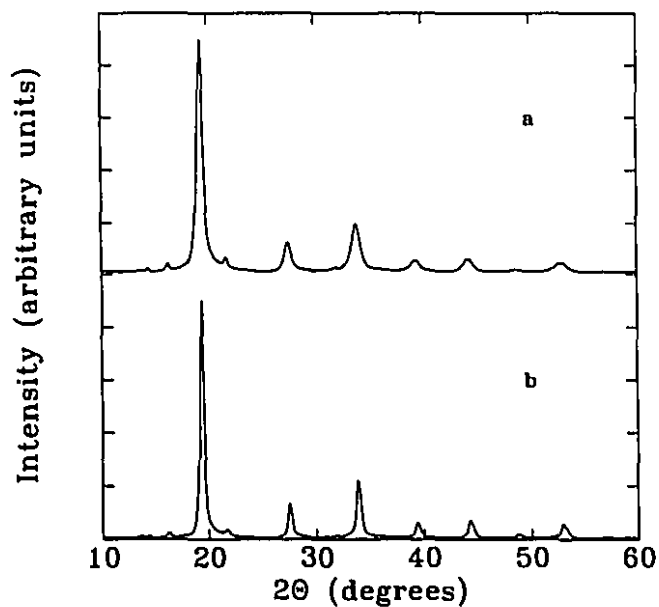


Figure 7.9: X-ray diffraction pattern of nanocrystalline FeTi before (a) and after (b) storage experiments.

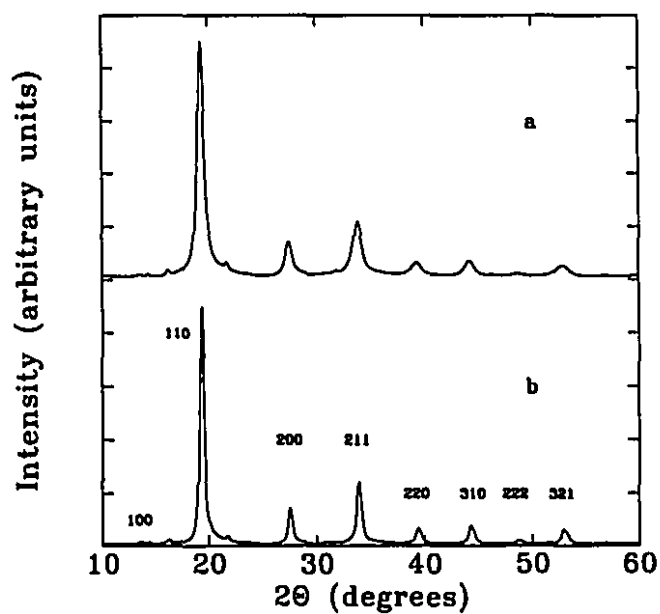


Figure 7.10: X-ray diffraction pattern of nanocrystalline $\text{Fe}_{50}\text{Ti}_{50}$ before (a) and after (b) storage experiments.

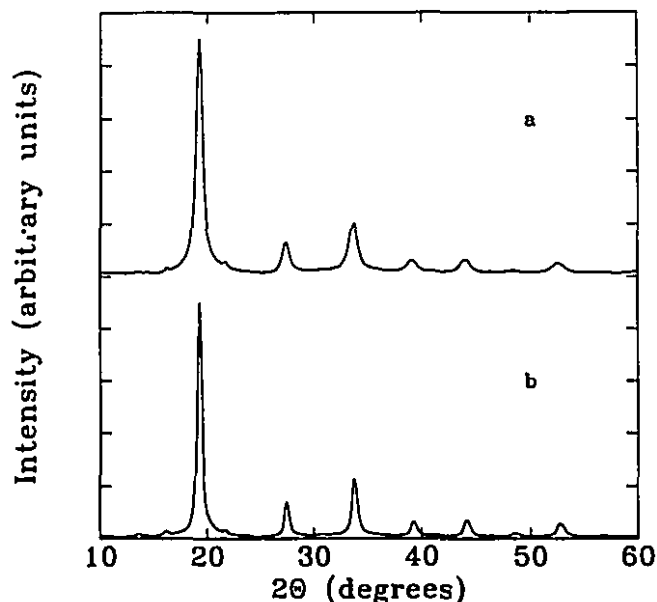


Figure 7.11: X-ray diffraction pattern of nanocrystalline $\text{Fe}_{40}\text{Ti}_{60}$ before (a) and after (b) storage experiments.

There is some growth however along the $[h00]$ direction, for which the domain size increases twofold. Nanocrystalline $\text{Fe}_{50}\text{Ti}_{50}$ and $\text{Fe}_{40}\text{Ti}_{60}$ behave in the same manner.

The strain values are also given on table 7.3. The results are rather surprising. As expected, the strain values for coarse-grained FeTi are low: 0.22 and 0.31 for $[hh0]$ and $[h00]$ respectively. There is a significant increase in strain after H cycling. This must be due to the defects created by the inhomogeneous volume expansion upon transforming to the β phase in absorption and back to the α phase during desorption. The creation of these defects is associated with hysteresis.

A different behavior is found in the case of nanocrystalline materials. The as-milled samples are highly strained along the $[hh0]$ direction. After activation and H cycling, there is little strain left, except in the case of nanocrystalline $\text{Fe}_{40}\text{Ti}_{60}$ along the $[h00]$ direction. These results, given the different activation behavior of coarse-grained and nanocrystalline sample, suggest that the defects created by the formation of the hydride in coarse-grained materials are essential for the absorption of hydrogen to take place. The results on nanocrystalline samples lead us to conclude that below

a certain crystallite size the hydride phase can form without defects being initially present. It might prove interesting to study the diffusion of hydrogen in a crystal, as a function of crystallite size, taking into account the elastic energy. Possibly, in large crystals, the interaction with a dislocation is necessary for the hydrogen atom to be able to move easily into the bulk of the crystal.

Unfortunately, since our material was heated to 400° after each measurement of the pressure-composition isotherm in order to remove all the hydrogen, it is likely that the lower strain in nanocrystalline is simply the result of thermal relaxation of the sample.

As could be expected the amorphous content of some samples is reduced by the activation treatment and the absorption-desorption cycling (see table 7.5). In all nanocrystalline samples, the amorphous content after hydrogen storage experiments is around 5-6%.

The lattice parameter of all equiatomic samples goes back to the value of coarse-grained FeTi 2.977-2.978 Å (see table 7.5). The long-range order parameter of all samples go to a rather high value (~ 0.9), providing additional evidence to relate the increase of the lattice parameter during milling to chemical disorder. Using Vegard's law to calculate the composition of the nanocrystals in Fe₁₀Ti₆₀, we obtain Fe₄₈Ti₅₂, a somewhat disappointing result (the nanocrystals return to the equiatomic composition, a more stable titanium-rich composition might have had interesting hydrogen storage properties).

In figure 7.7 we give the X-ray pattern of amorphous Fe₆₇Ti₃₃, treated with palladium, after several absorption-desorption cycles. The only crystalline peaks visible are those of tungsten carbide impurities, with the exception of a very weak and broad peak at 18.1° which would correspond to the Pd (111) reflection. The amorphous structure is not changed by the storage experiments (there is no significant change in the X-ray diffraction pattern).

The X-ray patterns of the nanocrystalline samples before and after activation and repeated storage cycles are given in figures 7.8, 7.9, 7.10, and 7.11.

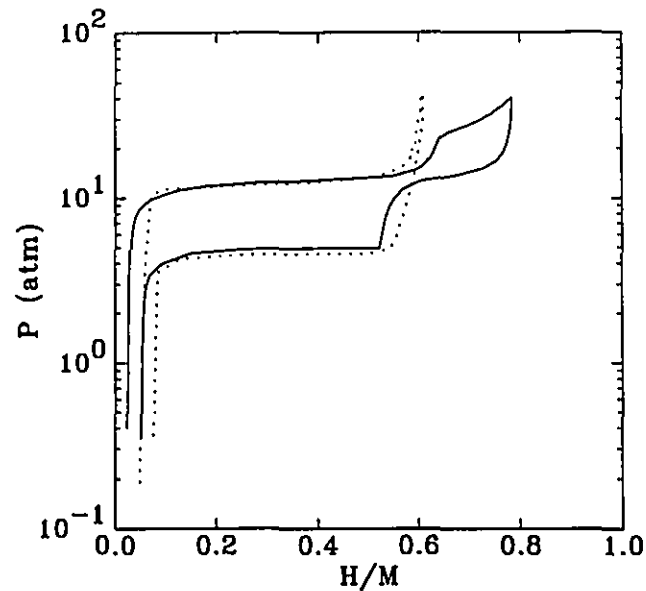


Figure 7.12: Pressure-composition isotherm of the crystalline component of coarse-grained FeTi (solid line) and nanocrystalline FeTi (dotted line), obtained by subtracting the amount of hydrogen corresponding to absorption in the amorphous phase using the isotherm of relaxed amorphous $\text{Fe}_{50}\text{Ti}_{50}$.

7.4 Discussion

7.4.1 Nanocrystalline Fe-Ti

As a first approximation, the pressure-composition isotherm of nanocrystalline FeTi can be explained by taking into account the storage capacity of amorphous Fe-Ti. We discussed in the previous chapter the presence of amorphous material in ball-milled FeTi. As we shall see later, there is an interaction between the nanocrystals and the amorphous regions. From the relative area of X-ray diffraction patterns, we estimated the amorphous content of nanocrystalline FeTi after storage experiments at 5%. We used the pressure-composition isotherm of relaxed amorphous $\text{Fe}_{50}\text{Ti}_{50}$ determined by L. Zaluski (reference [104] and figure 7.23) and subtracted it from the isotherm of coarse-grained FeTi and nanocrystalline FeTi according to the relation

$$c_{\text{crystal}}(P) = \frac{1}{1 - f_a} [c_{\text{observed}}(P) - f_a c_{\text{amorphous}}(P)] \quad (7.1)$$

where c is the concentration, P the pressure and f_a the fraction of amorphous phase in the sample. The concentration obtained is that of the crystalline fraction of the

sample. The resulting isotherms are shown in figure 7.12.

The results indicate that the plateau in the absorption isotherm of nanocrystalline FeTi, corresponding to the transformation from the α phase to the β phase, is narrower than that of coarse-grained FeTi. In addition, there is no transformation to the γ phase in the pressure range investigated. Since there is no transformation to the γ phase, it is not surprising that on desorption the material transforms back to the α phase without following a desorption isotherm similar to that of coarse-grained FeTi.

The narrowing of the miscibility gap is largely due to the presence of an amorphous component in the material. There is a reduction of the gap because of the presence of the amorphous fraction itself, reducing the amount of material involved in the α β transformation, and an additional reduction caused by the elastic stress between the two phases which, as we shall see below, counteracts the hydrogen-hydrogen effective interaction responsible for the miscibility gap. The evidence for the reduction caused by the interaction of the two phases comes from the fact that even when we consider the isotherm of the purely crystalline component, the plateau for the nanocrystalline sample is reduced with respect to that of coarse-grained FeTi.

As we said, the amorphous phase, in addition to having a different storage capacity, interacts with the crystallites through long-range stresses. As the amorphous component absorbs hydrogen, it expands and therefore exerts a negative pressure on the crystalline component, decreasing therefore the energy of solution by increasing the lattice spacing. Upon transforming to the β phase, the volume expansion of the crystalline component exceeds that of the amorphous. The latter then exerts a positive pressure on the nanocrystals, hindering the transformation to the γ phase by effectively compressing the lattice with respect to the value it would reach were the surface of the nanocrystals stress-free. The effective lattice compression increases the energy of the (4Fe,2Ti) sites involved in the formation of the γ phase.

It is possible to model the interaction between the crystalline and amorphous components using elasticity theory with a few simplifications as to the microstructure of the material. This is the purpose of the next sections. We shall first calculate the force-dipole tensor of FeTi, a necessary step to relate lattice expansion or compression to the energy of solution of hydrogen in the material.

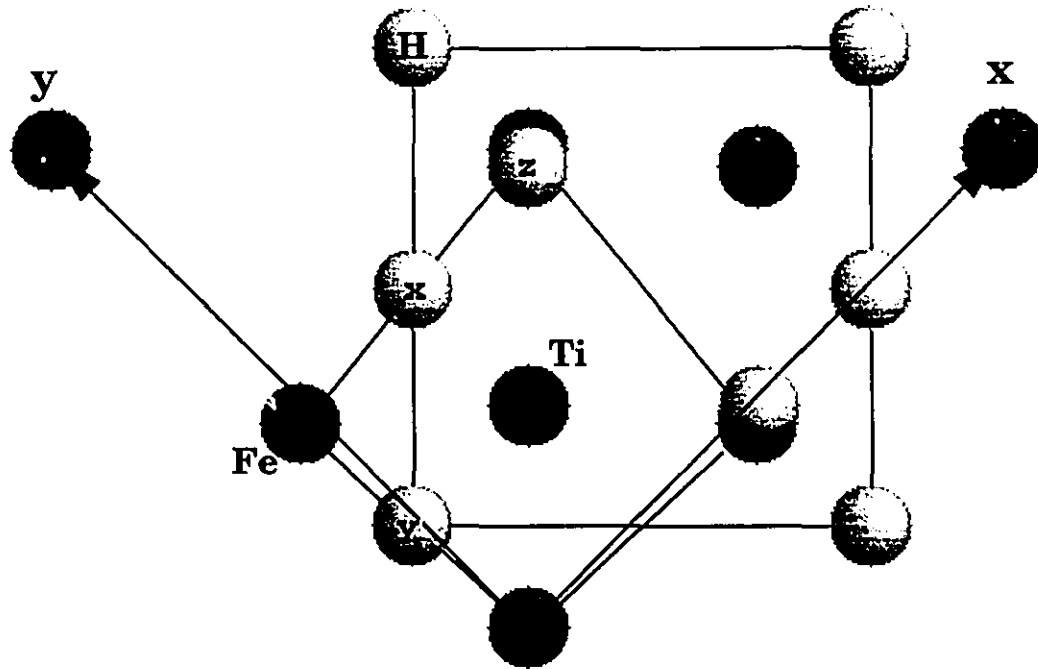


Figure 7.13: β_1 -FeTiH_{0.94} in the y-z plane (large cell: unit cell, small cell: FeTi distorted cell, Ti atoms and H atoms hiding iron are above the plane of the paper). Also drawn are the x and y axes of the initial FeTi cell, its z axis is normal to the paper. The x,y, and z sites are identified.

7.4.2 Force-dipole tensor of FeTi

The force-dipole tensor of FeTi can be evaluated from the deformation of the lattice measured by X-ray or neutron diffraction. With the lattice parameters of the distorted cell measured for one of the hydride phases one can calculate the strain tensor and, knowing the density of hydrogen atoms on each site, use equations (2.43) and (2.51) to obtain the components of the force-dipole tensor.

In the case of the β_1 phase, the lattice parameters are $a=2.954\text{\AA}$, $b=4.538\text{\AA}$, and $c=4.381$. The initial FeTi cell has two axes oriented along the $\frac{1}{2}(b+c)$ and $\frac{1}{2}(b-c)$ vectors of the new unit cell. We choose these to be the y and x axes of the FeTi cell respectively. The z axis of the FeTi cell now corresponds to the x axis of the hydride phase. For the sake of clarity we have reproduced in figure 7.13 the structure of the β_1 phase with the axes of the initial FeTi cell. The H1 sites located at the corners of the unit cell are y sites, the other H1 sites are x sites, and the H2 sites are z sites (see figure 7.13).¹

¹The sites x, y, and z correspond to $j=1$, $j=2$, and $j=3$ respectively.

We have to neglect the alternating displacements of the iron atoms from one FeTi cell to the other. These are due to the ordered occupation of sites which is not treated in this model. The determination of the parameters of the distorted cell is made over two cells. The strain tensor for β_1 -FeTiH_{0.94} is:

$$\epsilon = \begin{bmatrix} 0.059 & 0.019 & 0 \\ 0.019 & 0.059 & 0 \\ 0 & 0 & -0.0075 \end{bmatrix}. \quad (7.2)$$

The elastic constants of FeTi are (in matrix notation) [11]:

$$c_{11} = 325 \pm 10 \text{ GPa} \quad (7.3)$$

$$c_{12} = 121 \pm 10 \text{ GPa} \quad (7.4)$$

$$c_{44} = 69 \pm 1 \text{ GPa}. \quad (7.5)$$

The occupancy of H1 and H2 sites were given in chapter 2 for β_1 -FeTiD_{1.0}. We shall assume that the H1 and H2 sites will be occupied in the same ratio as the D1 and D2 sites in the deuteride. The number of hydrogen atoms on each site per unit cell is:

$$N_1 = 0.414 \quad (7.6)$$

$$N_2 = 0.414 \quad (7.7)$$

$$N_3 = 0.113, \quad (7.8)$$

and the corresponding densities are:

$$\rho_1 = 1.350 \times 10^{28} \text{ m}^{-3} \quad (7.9)$$

$$\rho_2 = 1.350 \times 10^{28} \text{ m}^{-3} \quad (7.10)$$

$$\rho_3 = 4.28 \times 10^{27} \text{ m}^{-3}. \quad (7.11)$$

The force-dipole tensor we obtain for x sites is:

$$P_1 = - \begin{bmatrix} 1.66 & 0.12 & 0.12 \\ 0.12 & 0.18 & -0.16 \\ 0.12 & -0.16 & 0.18 \end{bmatrix} \times 10^{-18} \text{ joule} \quad (7.12)$$

$$P_1 = - \begin{bmatrix} 10.36 & 0.75 & 0.75 \\ 0.75 & 1.12 & -0.99 \\ 0.75 & -0.99 & 1.12 \end{bmatrix} \text{ eV}. \quad (7.13)$$

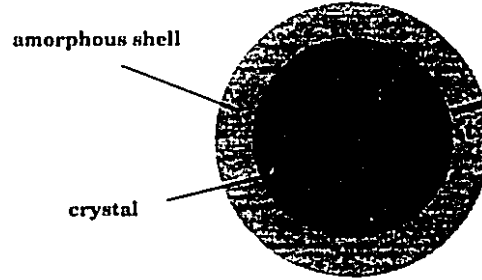


Figure 7.14: Spherical shell model.

Given the symmetry of the octahedral sites in FeTi, the model we use is not consistent with non-zero off-diagonal components in the force-dipole 7.13. The shear deformation found in the hydride phase is a result of the ordering of the hydrogen on the z sites. If shear deformations were found without any ordered occupation breaking the crystallographic symmetry, it would be a second-order effect in terms of the shear components of the strain tensor, however we only consider effects which are linear in terms of the deformation. Consequently, the off-diagonal terms will be dropped. The force-dipole tensor will be used only in the case of uniform pressures where shear deformations do not play a role.

The β_2 -FeTi_{1.40} phase has equal numbers of hydrogen atoms on the three types of sites, therefore only the trace of the dipole tensor is accessible. The trace is 13.4eV, compared to 12.6eV for the β_1 phase. The precision of calculations made using the force-dipole tensor is therefore restricted to 10%, considering also the uncertainty on the elastic constants.

7.4.3 Spherical shell model

In the presence of external forces the condition of time-averaged mechanical equilibrium becomes:

$$\overline{\left(\frac{H_{tot}}{\partial v_{m\mu}}\right)} = F_{m\mu} \quad (7.14)$$

where F_m is the force applied on atom m . We will be interested only in cases where it vanishes everywhere except on the surface of a crystal. Equation 2.37 is changed to:

$$\Phi_{mn} \cdot \nu_n = -\Psi_m + F_m. \quad (7.15)$$

In the continuum model, this translates into a new boundary condition (see equa-

tion 2.49):

$$C_{\alpha\beta\mu\nu}\hat{n}_\beta(\mathbf{r})\epsilon_{\mu\nu}(\mathbf{r}) = -\hat{n}_\beta(\mathbf{r})[\Pi_{\alpha\beta}(\mathbf{r}) - \sigma_{\alpha\beta}] \quad (7.16)$$

where $\sigma_{\alpha\beta}$ is the homogeneous external constraint producing the forces \mathbf{F}_m . The stress tensor $\sigma_{\alpha\beta}$ will go into equation (2.47) where it was set to zero for free crystals. Equation (2.52) becomes

$$\epsilon_{\mu\nu}(\mathbf{r}) = -S_{\mu\nu\alpha\beta}[\Pi_{\alpha\beta}(\mathbf{r}) - \sigma_{\alpha\beta}] \quad (7.17)$$

and, instead of 2.63, we find

$$H_{elastic} = -\frac{1}{2} \int \Pi_{\alpha\beta}(\mathbf{r}) S_{\alpha\beta\mu\nu} \Pi_{\mu\nu}(\mathbf{r}) d^3\mathbf{r} + \frac{1}{2} \int \sigma_{\alpha\beta} S_{\alpha\beta\mu\nu} \sigma_{\mu\nu} d^3\mathbf{r} \quad (7.18)$$

$$= -\frac{1}{2} \int \Pi_{\alpha\beta}(\mathbf{r}) S_{\alpha\beta\mu\nu} \Pi_{\mu\nu}(\mathbf{r}) d^3\mathbf{r} + \frac{V}{2} \sigma_{\alpha\beta} S_{\alpha\beta\mu\nu} \sigma_{\mu\nu} \quad (7.19)$$

$$= -\frac{1}{2} \int \Pi_{\alpha\beta}(\mathbf{r}) S_{\alpha\beta\mu\nu} \Pi_{\mu\nu}(\mathbf{r}) d^3\mathbf{r} + \frac{1}{2} K V \sigma^2, \quad (7.20)$$

where we only consider a uniform pressure on the crystal ($\sigma_{\alpha\beta} = \sigma\delta_{\alpha\beta}$). The second term in (7.20) is the change to the potential energy caused by the external pressure. The total potential energy is the sum of the harmonic potential of the host lattice and the hydrogen potential energy which includes a constant term and a linear hydrogen-metal term. The potential energy of the metal-hydrogen solution near its point of stress-free equilibrium has the same quadratic dependence in terms of lattice expansion than the pure metal around its own point of mechanical equilibrium. Adding an external pressure will change the potential energy in the same manner as it would change that of the pure lattice, by adding a term depending on the external pressure σ . There is no term involving both the force-dipole and the external pressure.

The negative pressure on nanocrystals is caused by the expansion of the amorphous regions as they absorb hydrogen prior to the transformation of the crystalline component from α -FeTi-H to β -FeTi-H, after which the reverse takes place, the crystals exert a positive pressure on the amorphous regions. We present here two simple models to describe this: a spherical shell model (figure 7.14) where the amorphous material forms a shell on the surface of spherical crystals and a uniform dispersion model where amorphous inclusions are homogeneously dispersed throughout the material. There is experimental evidence to support the spherical shell model. Transmission elec-

iron microscopy on nanocrystalline $\text{Fe}_{50}\text{Ti}_{50}$ [104] shows nanometer-sized crystallites separated by a thin amorphous or highly disordered layer.

To describe the equilibrium of the composite material we need the force-dipole tensor and the elastic constants of both phases. The force-dipole tensor of crystalline FeTi was previously calculated from crystallographic data and the elastic constants have also been reported [11]. In the absence of data for amorphous $\text{Fe}_{50}\text{Ti}_{50}$ we have to extrapolate on the basis of empirical observations on amorphous alloys. The bulk and shear modulus of amorphous transition metal alloys are generally 4% and 30% lower, respectively, than those of the crystalline intermetallic compound of the same composition [50]. The bulk modulus of FeTi is 189GPa and the shear modulus is 69GPa. We therefore use 181GPa and 48GPa for amorphous $\text{Fe}_{50}\text{Ti}_{50}$. The Poisson ratio and Young's modulus can also be found by assuming that the amorphous phase is isotropic [75].

For the amorphous phase we assume an isotropic and diagonal force-dipole tensor with diagonal elements given by (2.59):

$$P_a = -Bv_H, \quad (7.21)$$

where the index a stands for the amorphous phase and v_H is the volume expansion per hydrogen atom. Although there are no precise figures for v_H , the literature [34] on amorphous transition metal alloys suggests it should be around 2.8\AA^3 . The use of a single force-dipole tensor is not strictly correct since there is a variety of sites with probably differing volume expansions associated to them. However, since the volume expansion per hydrogen atom is usually around $2.8 \pm 0.2\text{\AA}^3$ for most metal-hydrogen systems, we may think it does not vary much from one type of site to another in the same material.

The spherical shell of inner and outer radii R_1 and R_2 respectively is subjected to a pressure $-\sigma$ on the inner surface. The outer surface will be considered free. This model would become extremely complicated otherwise. The stress components on such a spherical shell with an inner pressure are given as an exercise in Landau and

Lifshitz [54]. In spherical coordinates (r, θ, ϕ) they are ¹:

$$\sigma_{rr} = -\frac{\sigma R_1^3}{R_2^3 - R_1^3} \left(1 - \frac{R_2^3}{r^3}\right) \quad (7.22)$$

$$\sigma_{\theta\theta} = \sigma_{\phi\phi} = -\frac{\sigma R_1^3}{R_2^3 - R_1^3} \left(1 + \frac{R_2^3}{2r^3}\right). \quad (7.23)$$

In the case of a thin shell ($t = R_2 - R_1 \ll R_1, R_2$) we have

$$\sigma_{rr} = \frac{\sigma}{2} \quad (7.24)$$

$$\sigma_{\theta\theta} = \sigma_{\phi\phi} = -\frac{\sigma r}{2t}. \quad (7.25)$$

For 10 nm crystallites and 10% amorphous content the thickness is $t = 0.19$ nm.

Using

$$P_c = \frac{P + 2P'}{3}, \quad (7.26)$$

where the index c designates the crystal, we find for the elastic energy of the crystal and the amorphous shell:

$$H_c = -\frac{1}{2} \frac{P_c^2 K_c N_c^2}{V_c} + \frac{1}{2} K_c V_c \sigma^2 \quad (7.27)$$

(see equation (2.66) and (7.20)) and

$$H_a = -\frac{1}{2} \frac{P_a^2 K_a N_a^2}{V_a} + V_a \frac{1}{2} \sigma_{\alpha\alpha} S_{a,\alpha\alpha\mu\mu} \sigma_{\mu\mu} \quad (7.28)$$

respectively. We want to eliminate σ in the equations above. The constraint that the situation dictates is that linear deformations along the surface of the shell must be equal to linear deformations inside the crystal. This will ensure contact between the crystal and the shell. In other words:

$$\epsilon_{\theta\theta} = \epsilon_{\phi\phi} = \frac{1}{3} \epsilon_{c,\mu\mu} \quad (7.29)$$

By using one third of the relative volume expansion in (7.29) we neglect the change of shape of the crystal, since its expansion is not equal in the three perpendicular directions. This approximation is not worse than choosing a spherical crystal in the first place.

¹There is no summation on indices r, θ , and ϕ .

Using equation (7.17) we have:

$$\epsilon_{c,\mu\mu} = -S_{c,\mu\mu\alpha\beta} [\Pi_{\alpha\beta} - \sigma_{\alpha\beta}] \quad (7.30)$$

$$= -\frac{K_c P_c N_c}{V_c} + K_c \sigma \quad (7.31)$$

For the amorphous shell

$$\epsilon_{\theta\theta} = -\frac{1}{3} \frac{K_a N_a P_a}{V_a} + S_{a,\theta\theta\alpha\alpha} \sigma_{\alpha\alpha}. \quad (7.32)$$

Inserting equations 7.31 and 7.32 in 7.29 we find

$$-\frac{K_c P_c N_c}{V_c} + K_c \sigma = -\frac{K_a N_a P_a}{V_a} + 3S_{a,\theta\theta\alpha\alpha} \sigma_{\alpha\alpha}. \quad (7.33)$$

We isolate σ :

$$\sigma = \frac{\frac{K_c P_c N_c}{V_c} - \frac{K_a P_a N_a}{V_a}}{K_c + \frac{3\nu_a}{2Y_a} + \frac{3r}{2Y_a t} - \frac{3\nu_a r}{2Y_a t}}, \quad (7.34)$$

where Y_a is Young's modulus and ν_a the Poisson ratio of the amorphous phase. In terms of the concentration in the crystalline (c_c) and the amorphous (c_a) components we have

$$\sigma = \frac{\frac{K_c P_c c_c}{v_c} - \frac{K_a P_a c_a}{v_a}}{K_c + \frac{3\nu_a}{2Y_a} + \frac{3r}{2Y_a t} - \frac{3\nu_a r}{2Y_a t}}, \quad (7.35)$$

where v_c and v_a is the specific volume of each component. Here we have changed our convention from $c = N/N_H$ to $c = N/N_L$.

We now have an expression for the pressure exerted on the crystal as a function of the number of hydrogen atoms N_c and N_a dissolved in the crystal and the amorphous shell respectively. N_a does not vary much in the pressure range of interest, we may therefore use a single value and study the effect on the pressure-composition isotherm of the crystalline part. For fully relaxed amorphous Fe₅₀Ti₅₀ (reference [108] and figure 7.23) we have

$$N_a = 0.35N_{a,L}. \quad (7.36)$$

The correction to the chemical potential in equation (2.18) comes from the last term of equations 7.27 and 7.28. By differentiating with respect to N (N_c), we obtain

$$\Delta\mu = \frac{\partial}{\partial N_c} \left(\frac{1}{2} K_c V_c \sigma^2 + \frac{1}{2} V_a \sigma_{\alpha\alpha} S_{a,\alpha\alpha\mu\mu} \sigma_{\mu\mu} \right) \quad (7.37)$$

$$\Delta\mu = \left[\frac{1}{2} K_c V_c + \frac{1}{8} V_a \left[\frac{2r}{t} \left(\frac{\nu_a}{Y_a} + \frac{r}{Y_a t} - \frac{\nu_a r}{Y_a t} \right) + \frac{1}{Y_a} + \frac{2\nu_a r}{Y_a t} \right] \right] \cdot 2\sigma \frac{\partial \sigma}{\partial N_c}, \quad (7.38)$$

where

$$\frac{\partial \sigma}{\partial N_c} = \frac{K_c P_c}{V_c} \left[K_c + \frac{3\nu_a}{2Y_a} + \frac{3r}{2Y_{at}} - \frac{3\nu_a r}{2Y_{at}} \right]^{-1}. \quad (7.39)$$

The pressure-composition isotherm of the crystal surrounded by an amorphous shell is given by:

$$\frac{1}{2}kT \ln \left(\frac{P'}{P_0} \right) = \mu_0(T) - \frac{E_d}{2} + kT \ln \left(\frac{c}{0.7 - c} \right) - a_{int}c + \Delta\mu. \quad (7.40)$$

Following our new convention $c = N/N_L$, we had to put 0.7 instead of 1 in the configuration entropy term

$$kT \ln \left(\frac{c}{0.7 - c} \right). \quad (7.41)$$

Subtracting the equation for the purely crystalline material

$$\frac{1}{2}kT \ln \left(\frac{P}{P_0} \right) = \mu_0(T) - \frac{E_d}{2} + kT \ln \left(\frac{c}{0.7 - c} \right) - a_{int}c, \quad (7.42)$$

from (7.40), we obtain the relation between the pressures corresponding to each material at equal concentration:

$$P' = P e^{\left(\frac{2\Delta\mu}{kT} \right)}. \quad (7.43)$$

In the case of 10 nm crystals with 10% amorphous phase and $c_a=0.35$ we get from equation (7.35)

$$\sigma = -1.4 \times 10^9 c_c + 3.7 \times 10^8 \text{ Pa} \quad (7.44)$$

and the correction to the chemical potential becomes

$$\Delta\mu = 4.9 \times 10^{-21} c_c - 1.4 \times 10^{-21} \text{ J} \quad (7.45)$$

$$\Delta\mu = 0.031 c_c - 0.009 \text{ eV}. \quad (7.46)$$

The change in pressure at 32°C is given by

$$P' = P e^{(2.4c_c - 0.6)}. \quad (7.47)$$

We see immediately that the onset of the plateau corresponding to the transformation from the β_2 phase to the γ phase and which occurs at a concentration of 0.7 hydrogen per metal and a pressure of 25 atm will be shifted to a pressure of 68 atm, slightly above the range limit of our transducer. If the amount of amorphous phase is 5%, the pressure for that transformation goes to 39 atm.

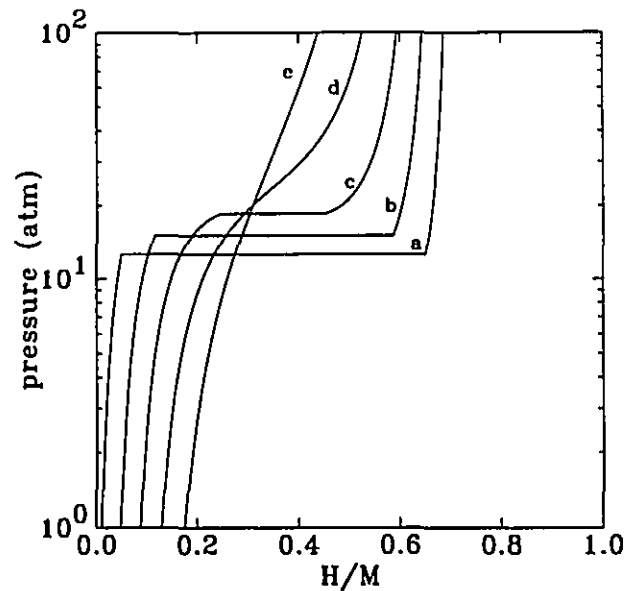


Figure 7.15: Calculated pressure-composition isotherms for different amounts of amorphous phase with hydrogen concentration $c_a=0.35$, as calculated using the spherical shell model. The initial isotherm has a plateau at 12.6 atm and a maximum solubility in the α phase of 0.05 hydrogen/metal. The amorphous content is: (a) 0%, (b) 10%, (c) 20%, (d) 30%, (e) 40%.

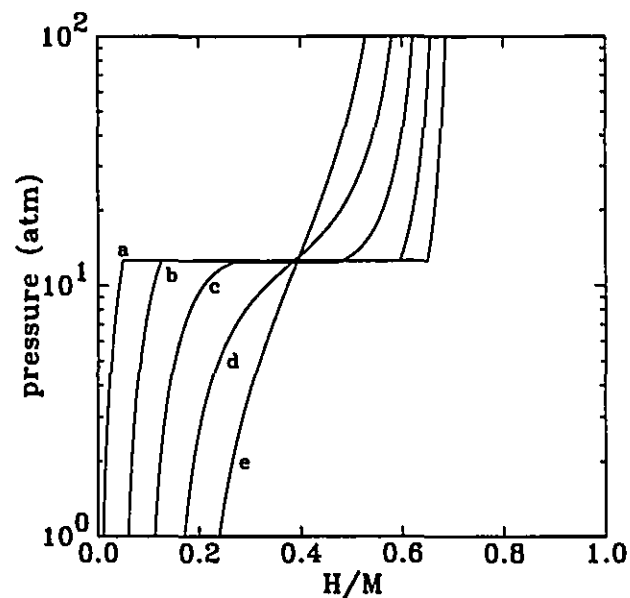


Figure 7.16: Calculated pressure-composition isotherms for different amounts of amorphous phase with hydrogen concentration $c_a=0.45$, as calculated using the spherical shell model. The amorphous content is: (a) 0%, (b) 10%, (c) 20%, (d) 30%, (e) 40%.

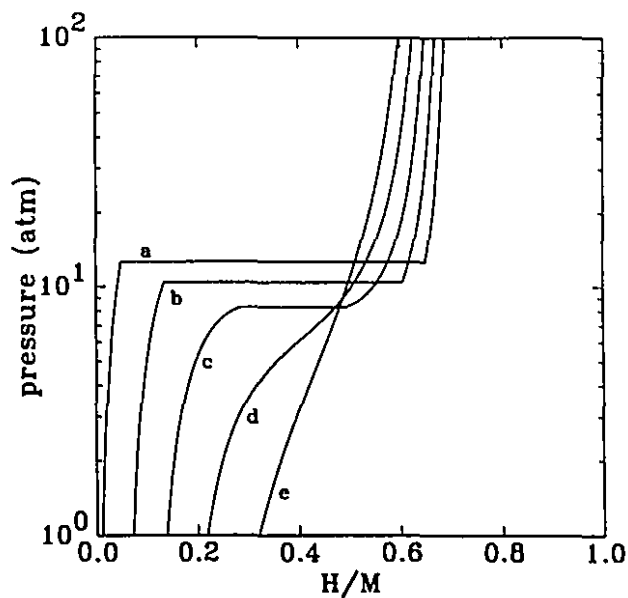


Figure 7.17: Calculated pressure-composition isotherms for different amounts of amorphous phase with hydrogen concentration $c_a=0.55$, as calculated using the spherical shell model. The amorphous content is: (a) 0%, (b) 10%, (c) 20%, (d) 30%, (e) 40%.

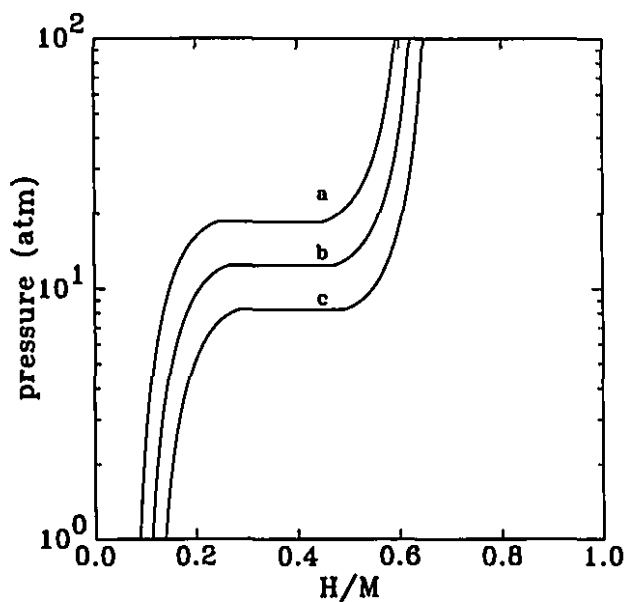


Figure 7.18: Calculated pressure-composition isotherms for different concentrations of hydrogen in the amorphous phase: (a) $c_a=0.35$, (b) $c_a=0.45$, (c) $c_a=0.55$. The amorphous content of the material is set to 20%.

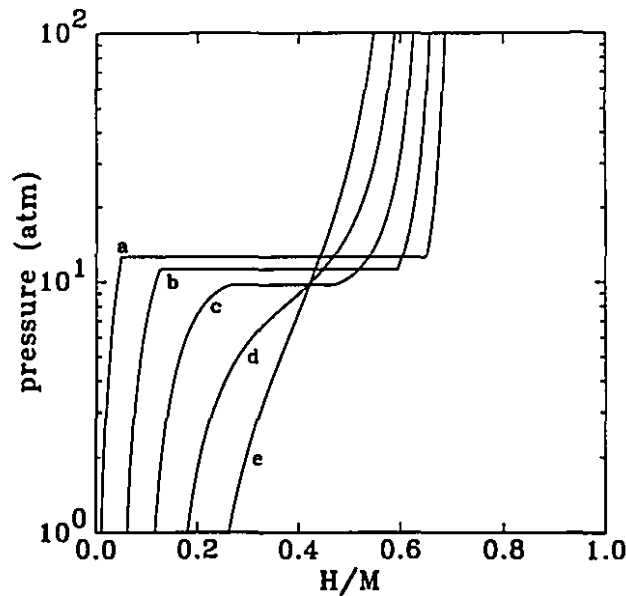


Figure 7.19: Calculated pressure-composition isotherms for different amounts of amorphous phase with hydrogen concentration $c_a=0.45$, as calculated using the spherical shell model. The volume expansion per hydrogen absorbed is assumed to be the same for the amorphous phase and β_1 -FeTiH_{0.94}. The amorphous content is: (a) 0%, (b) 10%, (c) 20%, (d) 30%, (e) 40%.

In figures 7.15, 7.16, 7.17, 7.18 we describe the influence of the amorphous phase on the absorption properties of the material for a crystal size of 12 nm. Since the plateau does not correspond to the chemical potential of an homogeneous solution we have to fit the data of coarse-grained FeTi, our reference sample, with equation (2.20). The correction to the chemical potential can be applied and the new plateau calculated from the modified chemical potential curve. First we have to calculate the constant terms in (2.20):

$$\frac{1}{2}kT \ln \left(\frac{P}{P_0} \right) = \mu_0(T) - \frac{E_d}{2} + kT \ln \left(\frac{c}{0.7 - c} \right) - a_{int}c. \quad (7.48)$$

We have arbitrarily chosen the concentration in β_1 FeTiH_{1.40} ($c = 0.7$) to be the number of storage sites, in order to simplify the model. The absorption plateau of coarse-grained FeTi is at 12.6 atm. We fix the solubility limit in the α phase to be 0.05 hydrogen per metal, the value given by Reilly and Wiswall [70]. From these values we determined the constants in the reference isotherm equation (7.48), then

we applied the correction for the chemical potential calculated above. The values are

$$a_{int} = 0.157\text{eV} \quad (7.49)$$

$$\mu_0 = 2.181\text{eV}. \quad (7.50)$$

From (7.49) we get for the critical temperature of formation of β -FeTiH_{1.10} $T_c = 455\text{K}$ (using $T_c = a_{int}/4k$, section 2.2). The phase diagram of the FeTi-H system determined by Reilly and Wiswall [70] ends at 70°C, but, extrapolating from the available data, the critical temperature seems to be located around 370K.

In the case of where the hydrogen concentration in the amorphous phase is $c_a = 0.35$ (figure 7.15), increasing the amount of amorphous phase increases the pressure of the plateau. The width of the plateau is also reduced, because of the amorphous phase which has a nearly fixed concentration, and because the elastic stress it exerts on the crystals counteracts the effective hydrogen-hydrogen interaction. For an amorphous content of 30%, there is no miscibility gap.

In the case of $c_a = 0.45$ (figure 7.16), which is the hydrogen concentration in unrelaxed amorphous Fe₅₀Ti₅₀, the same narrowing of the miscibility gap is observed, but there is almost no change in the pressure of the absorption plateau. If we consider an even higher concentration in the amorphous phase $c_a = 0.55$ (figure 7.17), the pressure of the plateau decreases with increasing concentration. This is the behavior we observe in our nanocrystalline materials. Our samples, with a crystal size of 12 nm and an amorphous content of 5-6% show a slight reduction in the pressure of the absorption plateau. The sample of L. Zaluski, with a smaller crystal size and a more important amorphous fraction show a significant reduction in pressure. It must be noted that his sample was heated only once at 400°C for 30 minutes, while our samples were heated several times. We also give the effect of varying the hydrogen concentration, keeping fixed the amount of amorphous phase, in figure 7.18. The lack of experimental data on the expansion of the amorphous phase leaves the possibility of substantial error in the evaluation of the force-dipole tensor of the amorphous phase. For example if we assume that the volume expansion per hydrogen atom dissolved in the amorphous phase is the same as that in the crystal (3.1\AA^3) instead of 2.8\AA^3 and use $c_a = 0.45$, the effect of the amorphous layer is to decrease the pressure of the plateau (figure 7.19).

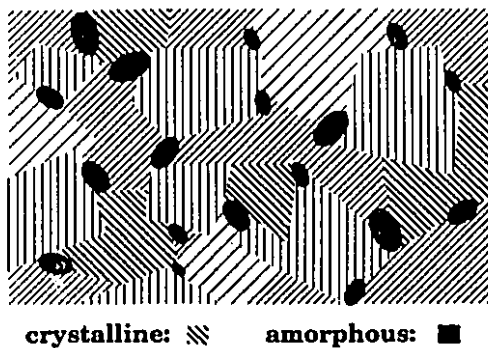


Figure 7.20: Uniform dispersion model.

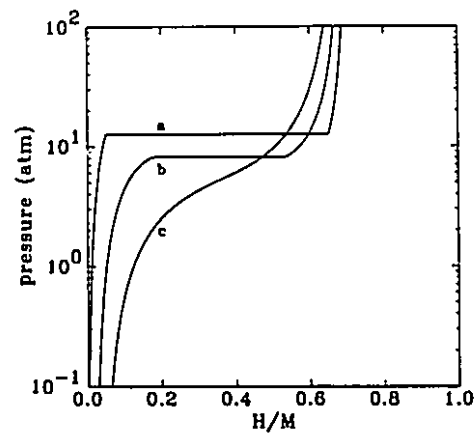


Figure 7.21: Calculated pressure-composition isotherms using the uniform dispersion model for different amounts of amorphous phase: (a) 0%, (b) 5%, (c) 10%.

Our conclusion on these matters is that the spherical shell model provides a sound framework for analyzing the stress-induced modifications to the storage behavior but that some specific parameters would need to be determined more precisely. It is still remarkable that this simple model produces elastic stresses of the good order of magnitude to affect the storage properties of materials in a fashion similar to what is observed in experiments.

7.4.4 Uniform dispersion model

We now consider an alternative model where small amorphous regions are uniformly dispersed throughout the material (figure 7.20). We disregard possible rearrangements at the microstructural level and consider the volume expansion of the matrix caused by hydrogen absorption in the amorphous regions to be homogeneous. Disregarding microstructural rearrangements such as cracking is not totally unjustified since electron microscopy observations of hydrogenated nanocrystalline samples show no sign of decrepitation [106]. We make two further simplifications. We assume that the bulk moduli of the crystalline and amorphous phases are equal and that the volume expansion per hydrogen atom dissolved is the same in both phases. Since this expansion is usually around 2.8\AA^3 for a large variety of hydrogen absorbing alloys, it

is not totally unreasonable to assume that the expansion is approximately the same for the different sites in the amorphous phase. The energy of solution will of course be different from one site to another.

We have a distribution of energies in the amorphous phase but since the hydrogen content of the amorphous phases varies slowly compared to the crystalline phase, especially in the plateau region, we might consider the hydrogen concentration constant.

The model is equivalent to having "amorphous" sites dispersed throughout the material. The chemical potential will therefore be given by:

$$\frac{1}{2}kT \ln \left(\frac{P}{P_0} \right) = \mu_0(T) - \frac{E_d}{2} + kT \ln \left(\frac{c_c}{0.7 - c_c} \right) - a_{int}c, \quad (7.51)$$

where we put again that only 0.7 sites per unit cell of the crystalline phase are accessible. Note that the configurational entropy term involves the hydrogen concentration in the crystalline phase while the interaction term involves the overall concentration. In principle, the configurational entropy term should involve the amorphous sites which have the same energy as the the crystalline sites. However the energy distribution of amorphous sites is very broad and most of them have an energy either smaller or larger than that of crystalline sites. Only a few sites within a narrow energy interval have to be counted with the crystalline sites and they are numerically unimportant.

We may express (7.51) as:

$$\frac{1}{2}kT \ln \left(\frac{P}{P_0} \right) = \mu_0(T) - \frac{E_d}{2} + kT \ln \left(\frac{c_c}{0.7 - c_c} \right) - a_{int}c_c f_c - a_{int}c_a f_a, \quad (7.52)$$

where f_c and f_a are the respective fractions of crystalline and amorphous phase ($f_c = 1 - f_a$). In order to obtain the correction to the chemical potential with respect to the reference isotherm (7.48) we must replace f_c by $1 - f_a$ in (7.52):

$$\frac{1}{2}kT \ln \left(\frac{P}{P_0} \right) = \mu_0(T) - \frac{E_d}{2} + kT \ln \left(\frac{c_c}{0.7 - c_c} \right) - a_{int}c_c - a_{int}(c_a - c_c)f_a. \quad (7.53)$$

The correction to the chemical potential —in the formalism of equation (7.43) —, is

$$\Delta\mu = -a_{int}(c_a - c_c)f_a. \quad (7.54)$$

The expression (7.54) elegantly and very simply express the fact that the amorphous phase pre-expands the matrix before the plateau and resists further expansion

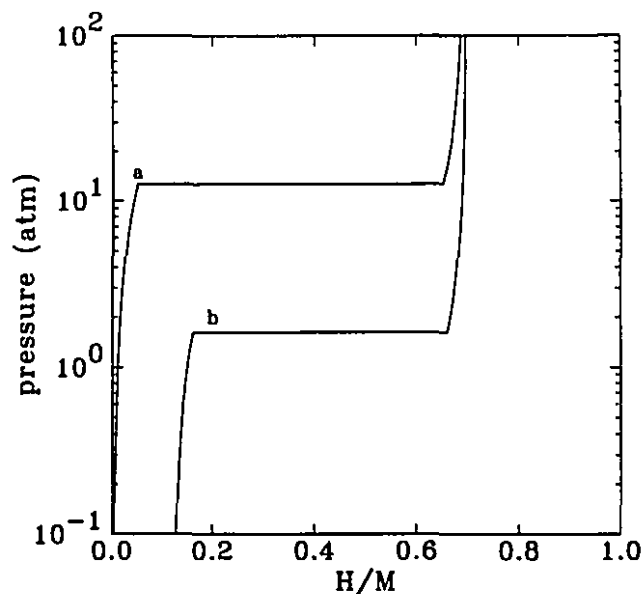


Figure 7.22: Calculated pressure-composition isotherms for partially disordered ($S = 0.9$) FeTi (b) and reference isotherm for fully ordered FeTi (a).

as the concentration in the crystalline phase exceeds that in the amorphous phase. Figure 7.21 shows the pressure-concentration isotherm for different amounts of amorphous phase in the material. Here we used $c_a = 0.45$.

The effect of the amorphous phase is stronger than what is found in the spherical shell model, probably because the amorphous regions do not have free surface in the uniform dispersion model. The full effect of the expansion of the amorphous phase is felt by the crystalline matrix.

7.4.5 Chemical disorder

Another important factor which can influence storage properties is the chemical disorder on the FeTi lattice. In all our equiatomic samples the long-range order parameter S is around 0.9. This means that the probability of finding a Ti atom on a Ti lattice site is 0.95 (see equation 6.1). The probability is the same for Fe atoms on Fe sites. Let us consider what happens then to the storage sites of the β phase (with 4 Ti and 2 Fe lattice sites). In the fully ordered FeTi compound we find 1.5 of these sites per metal atom. We suppose now that $S = 0.9$. We also assume that there is no

Table 7.6: Number of each site per metal atom for $S = 0.9$.

6Fe,0Ti	0.00000846
5Fe,1Ti	0.00064392
4Fe,2Ti	0.01839409
3Fe,3Ti	0.23406516
2Fe,4Ti	1.12712379
1Fe,5Ti	0.11671017
0Fe,6Ti	0.00305441

short-range order other than that coming from long-range order. In other words the probability of finding the right atom on the right lattice site is 0.95, regardless of the neighbouring atoms. We give below the number of each type of site per metal atom. We disregard the precise coordination but classify sites on the basis of the number of Fe and Ti atoms present. However the number of (4Ti,2Fe) sites with one or two Fe atoms on the Ti lattice (hereafter called "abnormal" (4Ti,2Fe) sites) is very small: 2% of the total number of (4Ti,2Fe) sites.

It is not clear what the energy of the "abnormal" (4Ti,2Fe) sites would be, but it is very likely that the (6Ti) and (5Ti,1Fe) sites have a potential energy lower than that of the normal (4Ti,2Fe) sites. We also expect the energy of the sites with 3 Fe atoms or more to have a higher potential energy. The (2Ti,4Fe) octahedral sites of the intermetallic compound may also have their energies changed by chemical disorder.

Upon filling the sites with hydrogen, we expect the low energy sites which exist because of chemical disorder to be occupied first. Among these, the (5Ti,1Fe) sites with the Fe atom on the Fe sublattice are the only which numerically matter. Then the normal (4Ti,2Fe) sites should be numerous enough to fill the sample up to 0.7 hydrogen per metal atom, the concentration of the β_2 phase. It is not clear how the pressure of the plateau would be affected, however the occupation of low energy (5Ti,1Fe) sites randomly located could well prevent the formation of any ordered configuration of hydrogen atoms, such as the octahedrally-coordinated hydrogen sublattice of the γ -FeTiH_{1.90} structure. It is also certain that the reduction of the normal

storage sites will translate into a further narrowing of the miscibility gap.

We illustrate the effect of disorder in figure 7.22 by calculating again the change to a reference pressure-composition isotherm with a plateau at 12.6 atm. We assume that the maximum number of hydrogen that can be absorbed in a disordered configuration is 0.7 per metal atom and that all the low energy sites, (6Ti) and (5Ti,1Fe), are occupied when we start filling the (4Ti,2Fe) sites for which we neglect the precise configuration. Therefore in this model, at $c=0.7$, we have 0.12 hydrogen per metal atom in deep sites and 0.58 in normal sites. The pressure-composition isotherm is given by:

$$\frac{1}{2}kT \ln \left(\frac{P}{P_0} \right) = \mu_0(T) - \frac{E_d}{2} + kT \ln \left(\frac{x}{0.58 - x} \right) - a_{int}c, \quad (7.55)$$

where x is the partial occupation of normal sites and c is the total concentration $c = 0.12 + 0.58 \cdot x$.

We do not really expect all deep sites to be filled before the (4Ti,2Fe) sites start being occupied nor do we assert that the maximum capacity will remain at $c=0.7$; our purpose here is to estimate the change in plateau pressure caused by chemical disorder. We wish to compare the changes to those caused by the elastic stress. The expansion caused by the hydrogen atoms located in deep sites is taken into account in the concentration dependent term. The potential energy of normal sites is fixed at the same value as that of fully ordered FeTi. We see that the effect of chemical disorder is to reduce the pressure of the plateau and the extent of the miscibility gap. There is also a shift of the plateau region to higher concentrations. This shift is observed for unrelaxed nanocrystalline $\text{Fe}_{50}\text{Ti}_{50}$ (section 7.5 below). The reduction in pressure is far too large with respect to the experimental observations. It is possible that the different chemical environment of the low energy sites leads to smaller lattice expansion, a lattice contraction is even observed in certain metals [34]. Consequently we may have exaggerated the interaction between the hydrogen atoms in the two kind of sites. More experimental data would be needed to treat this problem. However the 6 nm sample of L.Zaluski has a stronger reduction of the plateau pressure and since it was heated only 30 minutes at 400°C, we think that its initial long-range order parameter $S = 0.65$ may not have increased to 0.9 as in our samples. The additional chemical disorder may be responsible for the further reduction of the plateau pressure

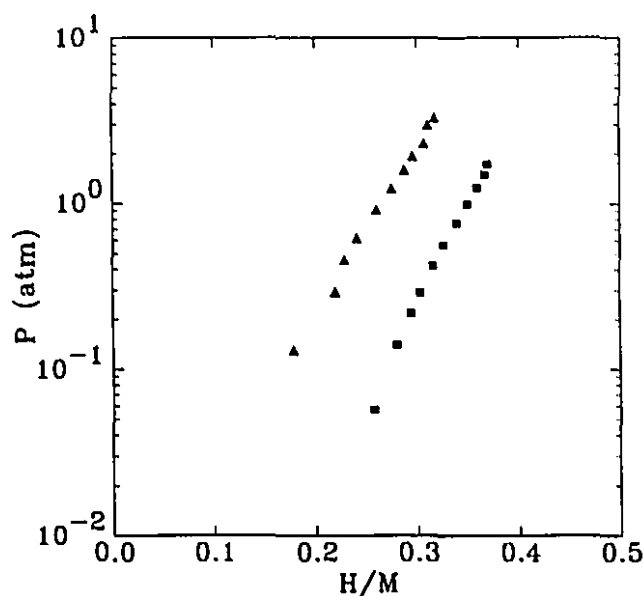


Figure 7.23: Pressure-composition isotherm for amorphous $\text{Fe}_{50}\text{Ti}_{50}$ measured by L. Zaluski [108] (squares: as-milled material, triangles: relaxed material).

(to ~ 7 atm).

7.4.6 Nanocrystalline $\text{Fe}_{40}\text{Ti}_{60}$

The nanocrystalline $\text{Fe}_{40}\text{Ti}_{60}$ exhibits a significantly lower plateau pressure. Supposing we accept the result that the composition of nanocrystals in this sample, as calculated using Vegard's law, is $\text{Fe}_{48}\text{Ti}_{52}$ (very close to the equiatomic composition), the number of "deep sites" is larger than what is found in $\text{Fe}_{50}\text{Ti}_{50}$ (0.18 per metal atom compared to 0.12 per metal atom respectively). Here we have used $S=0.9$ for both compositions. Given that the effect of filling these deep storage sites is to decrease the plateau pressure and shift the isothermal curve toward higher concentrations, the absorption behaviour of $\text{Fe}_{40}\text{Ti}_{60}$ is well described by this very approximate model.

The larger lattice parameter, compared to $\text{Fe}_{50}\text{Ti}_{50}$, may have some effect on the plateau pressure. Electronic effects could also play a role.

7.4.7 Relaxation in amorphous Fe-Ti

In this section we present our analysis of the effects of relaxation on hydrogen storage in amorphous $\text{Fe}_{50}\text{Ti}_{50}$ milled with palladium. The samples were made by L. Zaluski

and the content of this section has been published in a recent article [108].

Figure 7.23 shows the absorption curves of amorphous $\text{Fe}_{50}\text{Ti}_{50}$ as-milled and after annealing one hour at 400° . An irreversible relaxation takes place during annealing since the absorption curve, which is a straight line for all practical purposes, is shifted toward higher pressures.

The fact that relaxation does not change the slope of the isotherm but only shifts it to higher pressures suggests that the distribution of site energies is not changed in form but only shifted to higher energies. Assuming this displacement is caused by densification, it is possible to calculate the change in specific volume v_M from the pressure shift of the isotherm. We use the same linear potential between protons and metal atoms and hard core repulsion between protons [92], together with an isotropic and diagonal force-dipole tensor and replacing its diagonal component P by

$$P = -Bv_H, \quad (7.56)$$

where B is the bulk modulus of amorphous $\text{Fe}_{50}\text{Ti}_{50}$ and v_H the volume expansion per hydrogen absorbed. We feel justified in making use of an isotropic and diagonal force-dipole tensor since an amorphous material has no preferred direction and, on a scale larger than interatomic distances, can be considered isotropic.

Upon relaxation, the specific volume of the alloy decreases. We simply consider to have a material with the same elastic constants, but with a hydrogen-metal potential energy decreased by the amount corresponding to the change associated with the lattice expansion (or contraction in this case):

$$\Psi(\tau) = \Psi_o(\tau) + \Psi_m(\tau) \cdot \Delta\mathbf{u}_m, \quad (7.57)$$

where $\Delta\mathbf{u}_m$ is the displacement of metal atoms caused by relaxation, and $\Psi_o(\tau)$ is the potential energy of a site in the un-relaxed material prior to the equilibration of neighbouring metal atoms (see equation 2.35). The hard-core potential does not change with expansion or contraction and the purely elastic energy of the host alloy (the second term in equation 2.35) has its equilibrium point at the new hydrogen-free configuration. The energy associated with the relaxation enters into the first term Φ which does not affect the chemical potential of hydrogen.

The correction $\Psi_m(\tau) \cdot \Delta u_m$ to the potential energy becomes, in the continuum model,

$$\int \Pi_{\alpha\beta} \epsilon_{\alpha\beta} d^3r. \quad (7.58)$$

The $\epsilon_{\alpha\beta}$ of the last equation is the deformation produced by relaxation. We treat it as a pure contraction and find

$$\Delta H = -Bv_H \left(\frac{\Delta V}{V} \right) N, \quad (7.59)$$

where N is the number of dissolved protons.

The correction to the chemical potential is

$$\Delta\mu = -Bv_H \left(\frac{\Delta V}{V} \right). \quad (7.60)$$

The pressure in the relaxed material corresponding to a given concentration of hydrogen is related to that for the as-made material by the expression:

$$\frac{1}{2}kT \ln P' + Bv_H \frac{\Delta v_M}{v_M} = \frac{1}{2}kT \ln P. \quad (7.61)$$

The change in specific volume is

$$\frac{\Delta v_M}{v_M} = \frac{kT}{2Bv_H} \ln \frac{P}{P'}. \quad (7.62)$$

Using $v_H = 2.8\text{\AA}^3$ and $B=181\text{GPa}$ gives $\Delta v_M/v_M \approx -1\%$ and $\Delta\mu \approx 0.03\text{eV}$.

7.5 Relaxation in nanocrystalline Fe-Ti revisited

The effects of relaxation on hydrogen storage in nanocrystalline $\text{Fe}_{50}\text{Ti}_{50}$ with Pd catalyst have been reported by our group in a recently published article [108]. The results are reproduced in figure 7.24. The difference between the as-milled and annealed samples is attributed to the high level of strain and chemical disorder in ball-milled samples.

The calculated pressure-composition isotherm of section 7.4.5 does resemble the isotherm of as-milled $\text{Fe}_{50}\text{Ti}_{50}$, at least with regard to the decrease in plateau pressure and the large initial solubility at low pressure (discussed as a shift to higher concentrations in section 7.4.5). The disappearance of the plateau is likely due to the fact

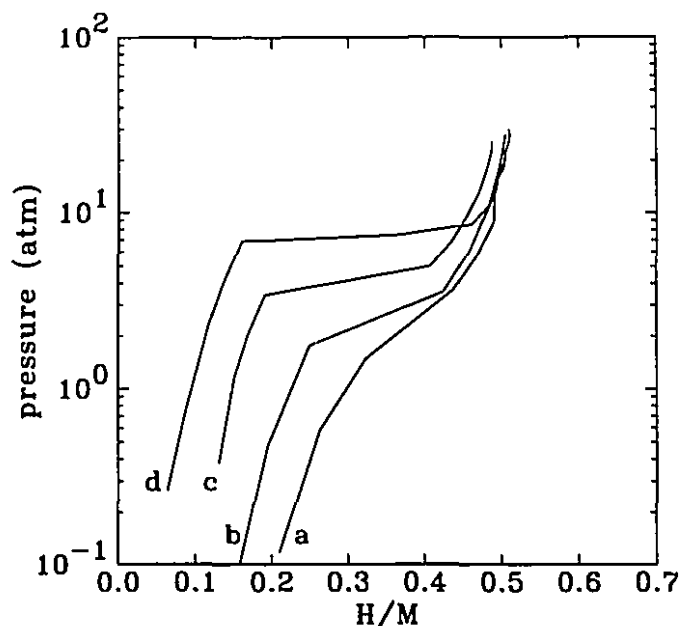


Figure 7.24: Pressure-composition isotherms of nanocrystalline $\text{Fe}_{50}\text{Ti}_{50}$ with Pd catalyst measured by I. Zaluski [108]: (a) as-milled, (b) after annealing at 300°C for 0.5 hour, (c) at 400°C for 0.5 hour, (d) after long annealing at 400°C .

that the energy distribution of $(4\text{Ti},2\text{Fe})$ storage sites can no longer be represented by a delta function, given the disorder of the surrounding lattice.

The long-range order parameter of our nanocrystalline samples increases substantially during activation, supporting the explanation offered in [108] for the change in storage properties upon relaxation. No significant recrystallization was reported in the above reference. If there were, it would also have the effect of raising the plateau pressure and extending the miscibility gap.

7.6 Hydrogen absorption in nanocrystalline palladium

In chapter 5 we discussed the experiments of several investigators on hydrogen absorption in nanocrystalline palladium. To summarize the literature on the subject, the experiments of Mütschele and Kirchheim [63, 62] show a broad distribution of sites linked to the presence of a large number of grain boundaries, while the experiments of Eastman et al. [83, 31, 23, 25] demonstrate that grain boundary regions are not different from those found in coarse-grained polycrystalline materials, and that

the hydrogen absorbed before the transformation to the hydride phase expands the palladium nanocrystals.

The neutron inelastic scattering experiments of Stuhr et al. [79] confirm the link between the broadening of the site energy distribution and the presence of a high density of grain boundaries. They propose that the grain boundary sites, while still located on lattice positions of the crystal, have their energies changed because of the proximity of the grain boundary. They also suggest that the hydrogen absorbed near the grain boundary causes an expansion of the whole nanocrystal, making it appear in the X-ray pattern as if there were only one type of site corresponding to absorption into the bulk. We agree with Stuhr et al. that this explanation reconciles the absorption data of Mütschle and Kirchheim with the structural observations of Eastman et al. on nanocrystalline palladium.

We have several reasons to propose for the modification of the energy of sites near the grain boundaries. First, strain near the grain boundaries caused by the different atomic coordinations in the boundary itself, is likely to extend several atomic layers inside the crystals. Considering that changes in density of 1% (for example in the case of amorphous $\text{Fe}_{50}\text{Ti}_{50}$), are sufficient to change the absorption pressure by an order of magnitude, moderate strains near the grain boundary may substantially change the energy of these sites. It is not necessary, therefore, to postulate the existence of a thick and highly disordered phase to explain the broadened energy distribution. Secondly, second and third nearest neighbour may contribute significantly to the elastic constants of the metal (see equation 2.41 and reference [28]), again the different atomic coordinations at grain boundaries probably affect the stress-strain relation over a distance larger than the thickness of the grain boundary itself. Finally, measurements of the vibrational spectrum of nanocrystalline materials [100] indicate a change in surface or interfacial modes, which is likely to affect the absorption on the sites near grain boundaries.

The hydrogen storage properties of nanocrystalline palladium, seen as a network of grain boundaries surrounding nanometer-sized grains, can very likely be modeled using an approach similar to what we have used in our study of Fe-Ti. At the time of writing, Eastman [24] has proposed such a model. We point out that the appropriate

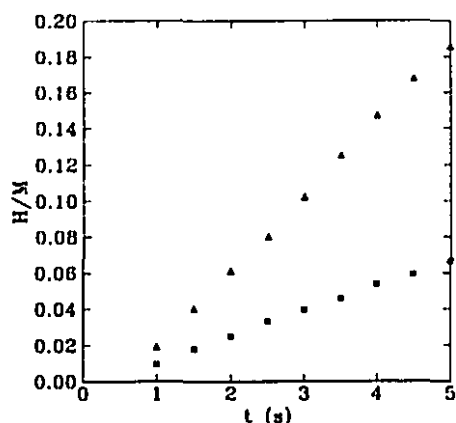


Figure 7.25: Concentration as a function of time in coarse-grained FeTi (squares) and nanocrystalline FeTi (triangles) at early times.

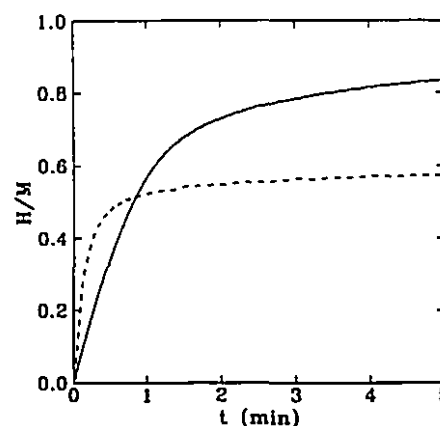


Figure 7.26: Concentration as a function of time in coarse-grained FeTi (solid line) and nanocrystalline FeTi (dashed line) for long times.

mathematical expressions, at least for a simplified model, have been presented here.

7.7 Kinetic properties

In view of possible applications, good kinetic properties are absolutely essential. Our group has already reported major improvements with respect to the rate of absorption of hydrogen in storage compounds [107]. Aoki et al. [3] have also reported an increase in absorption rate after milling. They attribute the increase to a smaller particle size. We report our own data here on coarse-grained FeTi and nanocrystalline FeTi. In these experiments the pressure was suddenly increased from 0 to 50 atm and the absorption measured. Typical absorption curves are shown on figures 7.25 and 7.26. Figure 7.25 gives the absorption data in the first five seconds, providing the absorption rate at low concentration. Figure 7.26, instead, gives the absorption curve in the first five minutes, where both samples practically reach their maximum storage capacity. The absorption rate at early times (low concentration) is 0.0133 ± 0.0002 hydrogen atom per metal atom per second in coarse-grained FeTi and 0.0371 ± 0.0006 in nanocrystalline FeTi. The absorption rate scales with the grain boundary volume but the relation is not simply linear. The results may indicate that the diffusion of hydrogen is faster along grain boundaries but they could also mean that the formation

of the hydride phase in the bulk of crystallites proceed faster because of different mechanical properties.

CONCLUSION

We summarize here the work we have presented. We performed two main kinds of experiments: ball milling of Fe-Ti at different compositions, monitored by X-ray diffraction, and hydrogen storage measurements on the resulting materials.

8.1 Milling experiments

Milling experiments on the FeTi intermetallic compound result in a rapid decrease of the crystallite size and the long-range order parameter, as well as an increase of the strain. The final crystallite size after 20 hours of milling is 12 nm. A fraction of the material is amorphous. This amount of amorphous phase correlates very well with the amount of oxygen contamination.

Milling a mixture of pure powders of composition $\text{Fe}_{50}\text{Ti}_{50}$ gives a similar material. The diffusion of Fe in hexagonal Ti transforms it into bcc Ti(Fe). Gradual enrichment of bcc Ti(Fe) brings it to partially disordered FeTi compound. An amorphous phase is already present at intermediate milling times (2-5 hours). It is not clear whether this amorphous phase is an intermediate reaction product or the result of oxygen-induced amorphization.

In order to establish more clearly the link between amorphous and oxygen contents, we performed a series of milling experiments on mixtures of iron titanium and iron oxide (Fe_2O_3). There is a linear relation between the amount of amorphous phase and the oxygen content after 20 hours of milling. An interesting result of these experiments is the decrease of strain as the average crystallite size goes below 10 nm.

In the case of the $\text{Fe}_{40}\text{Ti}_{60}$ composition the reactions proceed in the same manner as with $\text{Fe}_{50}\text{Ti}_{50}$. The final lattice parameter is larger than that of the equiatomic nanocrystalline sample, a result of the larger titanium content. The X-ray patterns at

intermediate milling times clearly show a bcc Fe-Ti structure with a lattice parameter between those of bcc β -Ti(3 at. % Fe) and cubic FeTi (CsCl structure).

After 20 hours of milling the Fe₆₇Ti₃₃ is completely amorphous. The crystallization enthalpy is slightly larger than that of vapor-quenched films [95].

Ball milling experiments were also analyzed using thermodynamic calculations performed by Zhi-Hua Yan using the CALPHAD method. These calculations show that, apart from the Fe rich region, the free energies of the amorphous phase and the bcc phase are very close and that an almost complete chemical disorder is necessary in order to have a transformation to the amorphous phase. In the iron-rich region there is a rather stable amorphous phase. This explains the ease to synthesize amorphous Fe₆₇Ti₃₃.

8.2 Hydrogen storage experiments

8.2.1 Equilibrium properties

The pressure-composition isotherm for coarse-grained FeTi is similar to what is found in the literature. The nanocrystalline samples however have a very different behaviour. In the case of nanocrystalline FeTi, there is no transformation to the γ -FeTiH_{1.90} phase. The pressure of the absorption and desorption plateau is reduced and the plateau is reduced in width. The results are similar for equiatomic samples made either by refinement of the intermetallic compound or by mechanical alloying of the pure elemental powders.

The presence of the amorphous phase was of critical importance in the analysis of the hydrogen storage properties of nanocrystalline FeTi. While the presence of the amorphous phase modifies the storage behavior by the simple reduction of the amount of crystalline material available for storage, the elastic stress between the amorphous and crystalline component modifies the chemical potential. This change is responsible for reducing the miscibility gap of the crystalline component and destabilizing the γ -FeTi-H phase. The interaction between the two phases reduces the pressure of the plateau corresponding to the transformation from the α to the β phase.

This interaction between the amorphous and crystalline component was analyzed using two simplified models of the microstructure. In the first model, a spherical

shell of amorphous material covers a nanocrystal. Elasticity theory then allows to establish a relation between the elastic stress and the hydrogen concentration in each phase. By assuming a constant hydrogen concentration in the amorphous phase over the pressure range of interest we were able to give the effective pressure on the nanocrystal and calculate the induced correction to the chemical potential.

The correction easily explains the destabilization of the γ phase. It also explains the change of the plateau pressure for the α - β transformation. The sign of this change is unfortunately dependent on data which are not available concerning the absorption properties of the amorphous phase as well as its elastic properties. Extrapolation from other amorphous metal-hydrogen systems leaves both possibilities open.

A similar behavior was found using a uniform dispersion model, where small inclusions of amorphous are uniformly dispersed in the material. The fact that nanocrystalline Fe-Ti does not decrepitate allows one to treat the amorphous inclusions as "amorphous" storage sites in an otherwise crystalline material.

The possible effect of chemical disorder was also analyzed. The calculated effect on the pressure-composition isotherm is much larger than the equilibrium pressure reduction observed in our samples. However the calculation might apply to a 6 nm sample made by L. Zaluski which was heated for a short time and showed an increased reduction in plateau pressure.

Nanocrystalline $\text{Fe}_{40}\text{Ti}_{60}$ shows a further reduction of the plateau pressure compared to $\text{Fe}_{50}\text{Ti}_{50}$. Several reasons can explain this difference: the increased number of sites with 5 or 6 Ti atoms, the larger lattice parameter compared to the equiatomic materials, or some electronic effect.

We also found that amorphous $\text{Fe}_{67}\text{Ti}_{33}$ absorbs hydrogen. This is totally different from the intermetallic compound Fe_2Ti which does not absorb hydrogen. The reason for this difference lies in the disordered nature of the amorphous structure which creates a wide distribution of storage energies. This amorphous alloy undergoes an irreversible relaxation upon a first hydrogen absorption-desorption cycle. A similar behavior was found by L. Zaluski when annealing amorphous $\text{Fe}_{50}\text{Ti}_{50}$ obtained by milling with extra oxygen. By assuming that the relaxation of the latter alloy was essentially a densification, we were able to estimate the change in specific volume

from the displacement of the pressure-composition isotherm after relaxation. To do this we considered the change in the metal-hydrogen potential due to the average reduction of interatomic distances.

Finally we gave a number of possible explanations for the narrowing of the miscibility gap in nanocrystalline palladium. Especially, we stressed the large changes in absorption behavior that can arise from very moderate lattice distortions near grain boundaries.

8.2.2 *Kinetic properties*

Our final word on this study is concerned with kinetic properties. The ability to store and retrieve hydrogen very rapidly is essential to the future use of metal hydride reservoirs. On this point, nanocrystalline materials are a step in the right direction. The absorption rate of nanocrystalline FeTi at low concentration is almost three times that of coarse-grained FeTi. The total storage capacity is unfortunately reduced, but this may be an acceptable compromise.

8.2.3 *Future experiments*

The use of X-ray diffraction during hydrogen charging of nanocrystalline samples could prove useful in confirming the validity of the model presented here. For example, if a shift of X-ray peaks was observed before there is any significant hydrogen absorption in the crystalline component, it would indicate that the stress caused by the absorption in grain boundary regions is expanding the lattice.

Finally, the long-term stability of the nanometer-sized microstructure after large numbers of absorption-desorption cycles needs to be determined in order to assess the usefulness of nanocrystalline metal hydrides.

APPENDICES

A.1 Chemical potential of hydrogen gas.

The free energy of a system is given by

$$A = -kT \ln Z, \quad (\text{A.1})$$

where k is Boltzmann's constant, T the temperature, and Z the partition function:

$$Z = \sum_i e^{-\frac{E_i}{kT}} \quad (\text{A.2})$$

where i runs over all states of the system. E_i is the energy of state i [88].

The most simple gas consists of a single particle without internal degrees of freedom in a cubic box. The energy eigenvalues are specified by three positive quantum numbers a, b , and c :

$$E_{a,b,c} = (a^2 + b^2 + c^2) \frac{h^2}{8ml^2}, \quad (\text{A.3})$$

(h is Planck's constant, m the mass of the particle and l the edge of the cube) [17].

We wish to evaluate (A.2) by changing it into an integral. At room temperature the energy step from one level to another is very small compared to kT , therefore we may disregard the discrete nature of the energy spectrum. We first need the density of states, that is the number of states per energy unit. The number of states with energy less than a given value is the volume of the region in Cartesian coordinates specified by

$$a > 0 \quad (\text{A.4})$$

$$b > 0 \quad (\text{A.5})$$

$$c > 0 \quad (\text{A.6})$$

$$a^2 + b^2 + c^2 < \frac{8ml^2 E}{h^2} \quad (\text{A.7})$$

(we have replaced the traditional coordinates x, y, z by a, b, c). This is the portion of the sphere of radius

$$r = \sqrt{\frac{8ml^2 E}{h^2}} \quad (\text{A.8})$$

comprised in the first octant. The volume of the region considered is therefore the eighth of the complete sphere:

$$n(E) = \frac{1}{8} \cdot \left(\frac{4\pi r^3}{3} \right) \quad (\text{A.9})$$

$$= \frac{4\pi l^3}{3h^3} (2mE)^{3/2} \quad (\text{A.10})$$

$$= \frac{4\pi V}{3h^3} (2mE)^{3/2} \quad (\text{A.11})$$

(V is the volume of the cube). The density of states $D(E)$ is then

$$D(E) = \frac{\partial n}{\partial E} \quad (\text{A.12})$$

$$= \frac{2\pi V}{h^3} (2m)^{3/2} \sqrt{E}. \quad (\text{A.13})$$

The sum (A.2) becomes

$$Z = \sum_i e^{-\frac{E_i}{kT}} \quad (\text{A.14})$$

$$= \int_0^\infty e^{-\frac{E}{kT}} dn \quad (\text{A.15})$$

$$= \int_0^\infty e^{-\frac{E}{kT}} \frac{\partial n}{\partial E} dE \quad (\text{A.16})$$

$$= \int_0^\infty e^{-\frac{E}{kT}} D(E) dE \quad (\text{A.17})$$

$$= \frac{2\pi V}{h^3} (2m)^{3/2} \int_0^\infty e^{-\frac{E}{kT}} \sqrt{E} dE \quad (\text{A.18})$$

$$= \frac{V}{h^3} (2\pi mkT)^{3/2}. \quad (\text{A.19})$$

We now consider a gas made of N identical molecules. The partition function for such a gas is:

$$Z = \sum_{E_1, E_2, \dots, E_N} \frac{N_j! N_k! \dots N_m!}{N!} e^{-\frac{E_1 + E_2 + \dots + E_N}{kT}}, \quad (\text{A.20})$$

where j, k, \dots, m designate occupied states. The factorials are introduced to take into account the indistinguishability of identical particles prescribed by quantum mechanics. The number of ways to have a given total energy is

$$\frac{N!}{N_j! N_k! \dots N_m!}. \quad (\text{A.21})$$

In the range of temperature and pressure used in our laboratory, the probability of having two molecules in the same eigenstate is very small, therefore all the $N_j!, N_k!, \dots, N_m!$ can be considered to be equal to 1. We are left with

$$Z = \frac{1}{N!} \sum_{E_1, E_2, \dots, E_N} e^{-\frac{E_1 + E_2 + \dots + E_N}{kT}} \quad (\text{A.22})$$

$$= \frac{1}{N!} \left(\sum_{E_1} e^{-\frac{E_1}{kT}} \right) \left(\sum_{E_2} e^{-\frac{E_2}{kT}} \right) \dots \left(\sum_{E_N} e^{-\frac{E_N}{kT}} \right) \quad (\text{A.23})$$

$$= \frac{1}{N!} \left(\sum_E e^{-\frac{E}{kT}} \right)^N. \quad (\text{A.24})$$

In the more general case where the energy levels of a single molecule are degenerate, we must introduce a factor g_E :

$$Z = \frac{1}{N!} \left(\sum_E g_E e^{-\frac{E}{kT}} \right)^N. \quad (\text{A.25})$$

The energy of the hydrogen molecule is a sum of translational, electronic, vibrational, and rotational terms. At room temperature we may neglect the electronic and vibrational excitations. For example the first excited vibrational state has an excitation energy of 0.5160eV. The ratio of the probability of finding an H_2 molecule in that state to the probability of finding it in the ground state is

$$\frac{P_{v=1}}{P_{v=0}} = e^{-\frac{0.5160}{kT}}, \quad (\text{A.26})$$

where v is the quantum number specifying the vibrational eigenstate. Our experiments were done at 305K and we have $k = 8.6171 \times 10^{-5} \text{eVK}^{-1}$. We find

$$\frac{P_{v=1}}{P_{v=0}} = 3 \times 10^{-9}. \quad (\text{A.27})$$

The electronic excitation energies are also of the order of electron-volts [8], therefore hydrogen molecules can be considered to be in the ground electronic and vibrational states.

The rotational states cannot be neglected. The first excitation energy is $7.32 \times 10^{-3} \text{eV}$. It is of the same order of magnitude as kT . The rotational eigenvalues are specified by the quantum number J :

$$E_J = \frac{J(J+1)h^2}{8\pi^2 I}, \quad (\text{A.28})$$

where I is the moment of inertia of the molecule. The degeneracy of each level is

$$g_J = 2J + 1. \quad (\text{A.29})$$

Were the molecule made of different nuclei an extra factor of two would have to be included for the exchange of the two nuclei. However in the case of two protons, the wavefunction must be antisymmetric (because the two nuclei are fermions) and there will be a coupling between the molecular angular momentum and the total nuclear spin, lifting the degeneracy [34].

Denoting translational eigenstates by the wave vector \mathbf{k} , equation (A.25) becomes

$$Z = \frac{1}{N!} \left(\sum_{\mathbf{k}, J} g_J e^{-\frac{E_0 + E_{\mathbf{k}} + E_J}{kT}} \right)^N \quad (\text{A.30})$$

$$= \frac{1}{N!} e^{-\frac{NE_0}{kT}} \left(\sum_{\mathbf{k}} e^{-\frac{E_{\mathbf{k}}}{kT}} \right)^N \left(\sum_J g_J e^{-\frac{E_J}{kT}} \right)^N, \quad (\text{A.31})$$

where E_0 is the ground state energy. The first summation was evaluated in (A.19). We transform the second into an integral:

$$\sum_{J=0}^{\infty} (2J+1) e^{-\frac{J(J+1)\hbar^2}{8\pi^2 I k T}} = \int_0^{\infty} (2J+1) e^{-\frac{J(J+1)\hbar^2}{8\pi^2 I k T}} dJ \quad (\text{A.32})$$

$$= \frac{8\pi^2 I k T}{h^2}. \quad (\text{A.33})$$

We use Stirling's approximation for the factorial:

$$N! \simeq \sqrt{2\pi N} \left(\frac{N}{e}\right)^N, \quad (\text{A.34})$$

with $e = 2.7183$.

The final result for the partition function is:

$$Z = e^{-\frac{N E_0}{k T}} \frac{1}{\sqrt{2\pi N}} \left[\left(\frac{c}{N}\right) \cdot \frac{V}{h^3} (2\pi m k T)^{3/2} \cdot \frac{8\pi^2 I k T}{h^2} \right]^N. \quad (\text{A.35})$$

Inserting (A.35) into the expression (A.1) for the free energy leads to:

$$A = N E_0 - k T \left[-\frac{1}{2} \ln 2\pi N - N \ln N + N + N \ln \left(\frac{V}{h^3} (2\pi m k T)^{3/2} \frac{8\pi^2 I k T}{h^2} \right) \right]. \quad (\text{A.36})$$

For the chemical potential, using (2.10), we obtain:

$$\mu = E_0 - k T \left[-\frac{1}{2N} - \ln N + \ln \left(\frac{V}{h^3} (2\pi m k T)^{3/2} \frac{8\pi^2 I k T}{h^2} \right) \right]. \quad (\text{A.37})$$

The first term inside the brackets is negligible when N is large. Isolating N in the ideal gas law

$$P V = N k T \quad (\text{A.38})$$

(where P is the pressure) and inserting in (A.37) we are left with

$$\mu = E_0 + k T \left[\ln P + - \ln \left(\frac{(2\pi m k T)^{3/2} 8\pi^2 I (k T)^2}{h^5} \right) \right]. \quad (\text{A.39})$$

If we put

$$P_0 = \frac{(2\pi m k T)^{3/2} 8\pi^2 I (k T)^2}{h^5}, \quad (\text{A.40})$$

(A.39) simply becomes

$$\mu = E_0 + k T \ln \frac{P}{P_0}. \quad (\text{A.41})$$

Taking the separate hydrogen atoms as the reference state, we replace the ground state energy by the negative of the dissociation energy E_d of the hydrogen molecule:

$$\mu = -E_d + k T \ln \frac{P}{P_0}. \quad (\text{A.42})$$

The value of P_0 at 305 K is 4.28×10^{10} Pa. The dissociation energy is $E_d = 4.478$ eV (432.1 kJ/mol).

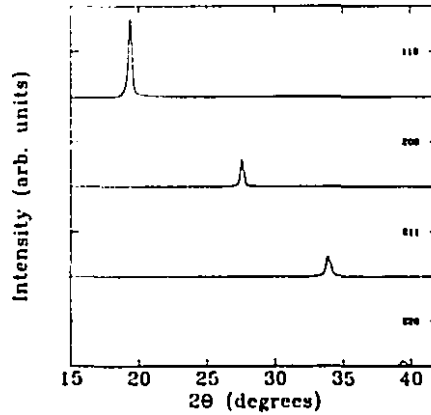


Figure A.1: Peak functions determined from the X-ray pattern of coarse-grained FeTi and used for fitting experimental peaks in patterns with an amorphous component.

A.2 Evaluation of the amorphous content.

Because of the asymmetry of the experimental peaks, we have to use the experimental peaks as a function for the fitting of X-ray patterns if we want to simultaneously evaluate the intensity of the amorphous background.

To determine the peak function we take a peak from the pattern of coarse-grained FeTi. For example the first peak ([110]) is in the 20 degrees region. We assume that the intensity at 15 and 25 degrees is solely due to the incoherent background which we assume to be linear in that interval. Let us put that the signal of the [110] peak is given by

$$I_{peak} = I_{exp} - (ax + b) \quad (\text{A.43})$$

where I_{exp} is the experimental intensity, I_{peak} is the intensity of the peak, and $(ax + b)$ is the straight line passing through the experimental points at 15 and 25 degrees. I_{peak} is the function we used for fitting other patterns. Its value outside of the 15-25 degrees range is set to zero (see figure A.1). The others peaks, [200], [211], and [220], were treated in the same fashion, with a suitable interval for each peak. All fits were performed in the interval from 15 to 42 degrees.

The calculated intensity of a peak is a convolution of the experimental peak function with a Lorentzian function:

$$I(\theta) = \int_{15}^{\theta} Lor(\theta - x) I_{peak}(x) dx. \quad (\text{A.44})$$

A Lorentzian function is given by

$$Lor(x) = \frac{A}{1 + \left(\frac{x-x_0}{w}\right)^2}. \quad (\text{A.45})$$

A , x_0 , w , the intensity, position shift, and broadening of the peak are optimized by the fitting program.

Since our peak function is not an analytical expression but a series of data points from 15 to 42 degrees, the integral (A.44) is replaced by a sum:

$$I(\theta) = \sum_i L_{or}(\theta - x_i) I_{peak}(x_i), \quad (\text{A.46})$$

where i runs over all points from 15 to 42 degrees.

The total calculated intensity is given by

$$I_{calc} = I_{[110]} + I_{[200]} + I_{[211]} + I_{[220]} + z \times I_{amor}(\theta) + c\theta + d. \quad (\text{A.47})$$

$I_{[110]}$, the intensity of the the first peak, as well as that of the three other peaks, is calculated from (A.46). $I_{amor}(\theta)$ is the intensity from the experimental X-ray pattern of the amorphous phase. The relative intensity of the amorphous component, z , is also optimized by the computer, as well as the parameters c and d of the linear background. Figure 6.18 gives an example of such a fit, for nanocrystalline $\text{Fe}_{50}\text{Ti}_{50}$.

The analysis of the patterns for the purpose of determining the crystallite size and strain level was done on the experimental patterns after subtraction of $z \times I_{amor}(\theta)$.

BIBLIOGRAPHY

- [1] G. Alefeld. *Ber. Bunsenges. Phys. Chem.*, 76:335, 1972.
- [2] G. Alefeld and J. Völkl, editors. *Hydrogen in Metals II*. Topics in Applied Physics. Springer-Verlag, Heidelberg, 1978.
- [3] K. Aoki, H. Aoyagi, A. Memezawa, and T. Masumoto. Effect of ball milling on the hydrogen absorption rate of FeTi and Mg₂Ni compounds. *Journal of Alloys and Compounds*, 203:17-19, 1994.
- [4] K. Aoki, M. Kamachi, and T. Masumoto. *Journal of Non-Crystalline Solids*, 61/62:679, 1984.
- [5] M. Atzmon. Characterization of AlNi formed by a self-sustaining reaction during mechanical alloying. In *Proceedings of the Seventh International Conference on Rapidly Quenched Materials, Stockholm, August 1990*, volume 134 of *Materials Science and Engineering A*, pages 1326-1329, 1991.
- [6] D.L. Beke, H. Bakker, and P.I. Loeff. On the elastic mismatch in the order-disorder transformation and solid state amorphization of intermetallic compounds—II. Criteria for the solid-amorphous transformation on intermetallic compounds. *Acta Metallurgica et Materialia*, 39(6):1267-1273, 1991.
- [7] J.S. Benjamin and T.E. Volin. The mechanism of mechanical alloying. *Metallurgical Transactions*, 5:1929-1934, 1974.
- [8] H. Beutler and H.O. Junger. Über das absorptionsspektrum des wasserstoffs. III. Die autoionisierung im term $3p\pi^1\Pi_u$ des H₂ und ihre auswahlgesetze. Bestimmung des ionisierungsenergie des H₂. *Zeitschrift für physik*, 100:80-94, 1936.
- [9] R. Birringer, H. Gleiter, H.-P. Klein, and P. Marquardt. Nanocrystalline materials. an approach to a novel solid structure with gas-like disorder? *Physics Letters*, 102A(8):365-369, June 1984.
- [10] R. Brüning, Z. Altounian, J.O. Ström-Olsen, and L. Schultz. A comparison between the thermal properties of Ni-Zr amorphous alloys obtained by mechanical alloying and melt-spinning. In *Proceedings of the Sixth International Conference on Rapidly Quenched Metals, Montréal, August 1987*, volume 97 of *Materials Science and Engineering*, pages 317-320, 1988.
- [11] U. Buchenau, H.R. Schober, J.-M. Welter, G. Arnold, and R. Wagner. Lattice dynamics of Fe_{0.5}Ti_{0.5}. *Physical Review B*, 27(2):955-962, 1983.
- [12] W. Buckel. Elektronenbeugungs-aufnahmen von dünnen metallschichten bei tiefen temperaturen. *Zeitschrift für physik*, 138:136-150, 1954.

- [13] P. Buffat and J.P. Borel. Size effect on the melting temperature of gold particles. *Physical Review A*, 13(6):2287-2298, June 1976.
- [14] T. Castro, R. Reifengerger, E. Choi, and R.P. Andres. Size-dependent melting temperature of individual nanometer-sized metallic clusters. *Physical Review B*, 42(13):8548-8556, November 1990.
- [15] B.-L. Chu, S.-M. Lee, and T.-P. Perng. Formation of amorphous Ti-Fe alloys by mechanical alloying. *Journal of Applied Physics*, 69(8):4211-4215, April 1991.
- [16] G. Cocco, N. Cowlam, and S. Enzo. Evidence for fractals in the preliminary stages of amorphization by mechanical alloying. *Materials Science and Engineering A*, 178:29-34, 1994.
- [17] C. Cohen-Tannoudji, B. Diu, and F. Laloë. *Mécanique quantique I*. Hermann, Paris, 1977.
- [18] W.A. Curtin and J.H. Harris. Thermodynamics of H in amorphous alloys: A lattice-gas model. In *Proceedings of the Sixth International Conference on Rapidly Quenched Metals, Montréal, August 3-7, 1987*, volume 99 of *Materials Science and Engineering*, pages 463-467, 1988.
- [19] R.M. Davis, B. McDermott, and C.C. Koch. Mechanical alloying of brittle materials. *Metallurgical Transactions A*, 19:2867-2874, December 1988.
- [20] S. Dietrich and H. Wagner. Model calculation for the incoherent phase-transition in the palladium-hydrogen system. *Zeitschrift für Physik B*, 36:121-126, 1979.
- [21] B.P. Dolgin, M.A. Vanek, T. McGory, and D.J. Ham. Mechanical alloying of Ni, Co, and Fe with Ti. Formation of an amorphous phase. *Journal of Non-Crystalline Solids*, 87:281-289, 1986.
- [22] J.H. Dymond and E.B. Smith. *The virial coefficients of pure gases and mixtures: a critical compilation*. Oxford science research papers. Clarendon Press, Oxford, 1980.
- [23] J.A. Eastman, M.R. Fitzsimmons, M. Müller-Stach, G. Wallner, and W.T. Elam. Characterization of nanocrystalline Pd by X-ray diffraction and EXAFS. *Journal of Nanostructured Materials*, 1:47-52, 1992.
- [24] J.A. Eastman, M.R. Fitzsimmons, L.J. Thompson, M.A. Beno, and G.S. Knapp. High angle diffraction studies of defects and phase stability in nanocrystalline materials. presented at the 1995 International Symposium on Metastable, Mechanically Alloyed and Nanocrystalline Materials, ISMANAM-95, Quebec City, 1995.
- [25] J.A. Eastman, L.J. Thompson, and B.J. Kestel. Narrowing of the palladium-hydrogen miscibility gap in nanocrystalline palladium. *Physical Review B*, 48(1):84-92, July 1993.

- [26] J. Eckert, J.C. Holzer, C.E. Krill III, and W.L. Johnson. Reversible grain size changes in ball-milled nanocrystalline Fe-Cu alloys. *Journal of Materials Research*, 7(8):1980-1992, August 1992.
- [27] J. Eckert, L. Schultz, and K. Urban. Synthesis of Ni-Ti and Fe-Ti alloys by mechanical alloying: formation of amorphous phases and extended solid solutions. *Journal of Non-Crystalline Solids*, 127:90-96, 1991.
- [28] C. Elsässer, M. Fähule, L. Schimmele, C.T. Chan, and K.M. Ho. Range of forces on host-metal atoms around interstitial hydrogen in Pd and Nb. *Physical Review B*, 50(8):5155-5159, August 1994.
- [29] J.D. Eshelby. Distortion of a crystal by point imperfections. *Journal of Applied Physics*, 25(2):255-261, 1954.
- [30] P. Fisher, W. Hälg, L. Schlapbach, F. Stucki, and A.F. Andresen. Deuterium storage in FeTi: measurement of desorption isotherms and structural studies by means of neutron diffraction. *Materials Research Bulletin*, 13(9):931-946, 1978.
- [31] M.R. Fitzsimmons, J.A. Eastman, and M. Müller-Stachand G. Wallner. Structural characterization of nanometer-sized crystalline Pd by x-ray-diffraction techniques. *Physical Review B*, 1991(6):2452-2460, August 1991.
- [32] T.B. Flanagan, B.S. Bowerman, and G.E. Biehl. Hysteresis in metal/hydrogen systems. *Scripta Metallurgica*, 14:443-447, 1980.
- [33] T.B. Flanagan and W.A. Oates. The effect of hysteresis on the phase diagram of Pd-H. *Journal of the Less-Common Metals*, 92:131-142, 1983.
- [34] Yuh Fukai. *The Metal-Hydrogen System*. Springer-Verlag, Heidelberg, 1993.
- [35] E. Gaffet, N. Malhouroux-Gaffet, M. Abdellaoui, and A. Malchère. Transitions de phases sous sollicitations mécaniques: élaboration de matériaux à nanostructures (alliages métalliques, semi-conducteurs, céramiques). *La Revue de Métallurgie-CIT/Science et Génie des Matériaux*, pages 757-769, 1994.
- [36] G.H. Gessinger. Mechanical alloying of IN-738. *Metallurgical Transactions A*, 7:1203-1209, August 1976.
- [37] H. Gleiter. On the structure of grain boundaries in metals. *Materials Science and Engineering*, 52:91-131, 1982. presented at the NATO Advanced Research Institute Meeting on the Atomistics of Fracture, Calcatoggio, Corsica, May 22-31, 1980.
- [38] A.T. Gorton, C. Bitsianes, and T.L. Joseph. Thermal expansion coefficients for iron and its oxides from X-ray diffraction measurements at elevated temperatures. *Transactions of the Metallurgical Society of AIME*, 233:1519-1525, 1965.

- [39] T. Graham. In *Philosophical Transactions of the Royal Society*, volume 156, page 399, London, 1866.
- [40] R. Griessen. Phase separation in amorphous metal hydrides: A stoner-type criterion. *Physical Review B*, 27:7575-7582, June 1983.
- [41] J.H. Harris, W.A. Curtin, and M.A. Tenhover. Universal features of hydrogen absorption in amorphous transition-metal alloys. *Physical Review B*, 36:5784-5797, 1987.
- [42] H. Horner and H. Wagner. A model calculation for the $\alpha - \alpha'$ phase transition in metal-hydrogen systems. *Journal of Physics C: Solid State Physics*, 7:3305-3325, 1974.
- [43] J. Horvath, R. Birringer, and H. Gleiter. Diffusion in nanocrystalline materials. *Solid State Communications*, 62(5):319-322, May 1987.
- [44] W. Klement Jr., R.H. Willens, and P. Duwez. Non-crystalline structure in solidified gold-silicon. *Nature*, 187:869-870, September 1960.
- [45] H. Kaneko, T. Kajitani, M. Hirabayashi, M. Ueno, and K. Suzuki. In *Fourth International Conference on Rapidly Quenched Metals*, volume 2, page 1605, Sendai, Japan, 1981.
- [46] H. Kanzaki. Point defects in face-centered cubic lattice-I distortion around defects. *The Physics and Chemistry of Solids*, 2:24-36, 1957.
- [47] J. Karch, R. Birringer, and H. Gleiter. Ceramics ductile at low temperature. *Nature*, 330:556-558, December 1987.
- [48] L. Kaufman and H. Bernstein. *Computer Calculations of Phase Diagrams*. Academic Press, New York, 1970.
- [49] H.P. Klug and L.E. Alexander. *X-ray diffraction procedures for polycrystalline and amorphous materials*. Wiley, New York, 1974.
- [50] G. Knuyt, L. De Schepper, and L.M. Stals. Calculation of elastic constants for an amorphous metal. In *Proceedings of the Sixth International Conference on Rapidly Quenched Metals, Montréal, August 3-7, 1987*, volume 98 of *Materials Science and Engineering*, pages 527-529, 1988.
- [51] C.C. Koch. *Mechanical Milling and Alloying*, volume 15 of *Materials Science and Technology*, chapter 5, pages 193-245. VCH, Weinheim, 1991.
- [52] C.C. Koch, O.B. Cavin, C.G. McKamey, and J.O. Scarbrough. Preparation of "amorphous" $\text{Ni}_{60}\text{Nb}_{40}$ by mechanical alloying. *Applied Physics Letters*, 43(11):1017-1019, December 1983.
- [53] T. Kuji and W.A. Oates. Thermodynamic properties of Nb-H alloys II: The β and δ phases. *Journal of the Less-Common Metals*, 102:261-271, 1984.

- [54] L. Landau and E. Lifshitz. *Théorie de l'élasticité*. Physique théorique. Editions Mir, Moscow, 1990.
- [55] S. Li, K. Wang, L. Sun, and Z. Wang. A simple model for the refinement of nanocrystalline grain size during ball milling. *Scripta Metallurgica and Materialia*, 27:437-442, 1992.
- [56] E.H. Love. *A Treatise on the Mathematical Theory of Elasticity*. Dover, New York, 4 edition, 1944.
- [57] H.L. Lukacs, E.T. Henig, and B. Zimmermann. *CALPHAD*, 1:225, 1977.
- [58] H.L. Lukacs, J. Weiss, and E.T. Henig. *CALPHAD*, 6:229, 1982.
- [59] F.D. Manchester, A. San-Martin, and J.M. Pitre. The H-Pd (hydrogen-palladium) system. *Journal of Phase Equilibria*, 15(1):62-83, 1994.
- [60] D.R. Maurice and T.H. Courtney. The physics of mechanical alloying: A first report. *Metallurgical Transactions A*, 21:289-303, February 1990.
- [61] P.J. Miller, C.S. Coffey, and V.F. DeVost. *Journal of Applied Physics*, 59:913, 1986.
- [62] T. Mütschele and R. Kirchheim. Hydrogen as a probe for the average thickness of a grain boundary. *Scripta Metallurgica*, 21:1101-1104, 1987.
- [63] T. Mütschele and R. Kirchheim. Segregation and diffusion of hydrogen in grain boundaries of palladium. *Scripta Metallurgica*, 21:135-140, 1987.
- [64] SGTE Data for Pure Elements, NPL Report, DMA(A), 1989.
- [65] P. Pochet, P. Bellon, L. Chaffron, and G. Martin. Phase transformation under ball milling: theory versus experiment. 1995 International Symposium on Metastable, Mechanically Alloyed and Nanocrystalline Materials, ISMANAM-95, Quebec City, 1995.
- [66] P. Ramachandrarao, B. Cantor, and R.W. Cahn. Free volume theories of the glass transition and the special case of metallic glasses. *Journal of Materials Science*, 12:2488-2502, 1977.
- [67] R. Ray, B.C. Giessen, and N.J. Grant. The constitution of metastable titanium-rich Ti-Fe alloys: An order-disorder transition. *Metallurgical Transactions*, 3:627-629, 1972.
- [68] O. Redlich and A.T. Kister. *Industrial and Engineering Chemistry*, 40:345, 1948.
- [69] F. Reidinger, J.F. Lynch, and J.J. Reilly. An X-ray examination of the FeTi-H₂ system. *Journal of Physics F: Metal Physics*, 12:L49-55, 1982.

- [70] J.J. Reilly and R.H. Wiswall Jr. Formation and properties of iron titanium hydride. *Inorganic Chemistry*, 13(1):218-222, 1974.
- [71] R.O. Scattergood and C.C. Koch. A modified model for hall-petch behavior in nanocrystalline materials. *Scripta Metallurgica et Materialia*, 27:1195-1200, 1992.
- [72] J. Schefer, P. Fisher, W. Hälg, F. Stucki, L. Schlapbach, and A.F. Andresen. Structural phase transitions of Fe-Ti-deuterides. *Materials Research Bulletin*, 14(10):1281-1294, 1979.
- [73] L. Schlapbach, editor. *Hydrogen in Intermetallic Compounds I. Topics in Applied Physics*. Springer-Verlag, Heidelberg, 1988.
- [74] L. Schlapbach, editor. *Hydrogen in Intermetallic Compounds II. Topics in Applied Physics*. Springer-Verlag, Heidelberg, 1992.
- [75] E. Schreiber, O.L. Anderson, and N. Soga. *Elastic Constants and Their Measurement*. McGraw-Hill, New York, 1973.
- [76] R.B. Schwarz and W.L. Johnson. Formation of an amorphous alloy by solid-state reaction of the pure polycrystalline metals. *Physical Review Letters*, 51(5):415-418, August 1983.
- [77] R.B. Schwarz and C.C. Koch. Formation of amorphous alloys by the mechanical alloying of crystalline powders of pure metals and powders of intermetallics. *Applied Physics Letters*, 49(3):146-148, July 1986.
- [78] F.G. Shi. Size dependent thermal vibrations and melting in nanocrystals. *Journal of Materials Research*, 9(5):1307-1313, May 1994.
- [79] U. Stuhr, H. Wipf, T.J. Udovic, J. Weismüller, and H. Gleiter. The vibrational excitations and the position of hydrogen in nanocrystalline palladium. *Journal of Physics: Condensed Matter*, 7:219-230, 1995.
- [80] K. Sumiyama, H. Ezawa, and Y. Nakamura. *Physica Status Solidi A*, 93, 1986.
- [81] K. Suzuki, K. Hayashi, Y. Tomizaka, T. Fukunaga, and K. Kai. *Journal of Non-Crystalline Solids*, 61:637, 1984.
- [82] P. Tessier, M.L. Trudeau, J.O. Ström-Olsen, and R. Schulz. Structural transformations and metastable phases produced by mechanical deformations in the Bi-Sr-Ca-Cu-O superconducting system. *Journal of Materials Research*, 8(6):1258-1267, June 1993.
- [83] G.J. Thomas, R.W. Siegel, and J.A. Eastman. Grain boundaries in nanophase palladium: high resolution electron microscopy and image simulation. *Scripta Metallurgica et Materialia*, 24:201-206, 1990.

- [84] P. Thompson, M.A. Pick, F. Reidinger, L.M. Corliss, J.M. Hastings, and J.J. Reilly. Neutron diffraction study of β iron titanium deuteride. *Journal of Physics F: Metal Physics*, 8(4):L75–80, 1978.
- [85] P. Thompson, F. Reidinger, J.J. Reilly, L.M. Corliss, and J.M. Hastings. Neutron diffraction study of α -iron titanium deuteride. *Journal of Physics F: Metal Physics*, 10:L57–59, 1980.
- [86] P. Thompson, J.J. Reilly, F. Reidinger, J.M. Hastings, and L.M. Corliss. Neutron diffraction study of γ iron titanium deuteride. *Journal of Physics F: Metal Physics*, 9(4):L61–66, 1979.
- [87] T.Kuji, W.A. Oates, B.S. Bowerman, and T.B. Flanagan. *Journal of Physics F*, 13:1785, 1983.
- [88] Richard C. Tolman. *The Principles of Statistical Mechanics*. Dover, New York, 1979.
- [89] M.L. Trudeau, L. Dignard, R. Schulz, P. Tessier, L. Zaluski, and J.O. Ström-Olsen. Oxidation behaviour of nanocrystalline Fe-Ti prepared by high-energy ball milling. In *Journal of Nanostructured Materials*, volume 1, pages 457–464. First International Conference on Nanostructured Materials, 1992.
- [90] M.L. Trudeau, R. Schulz, D. Dussault, and A. Van Neste. Structural changes during high-energy ball milling of iron-based amorphous alloys: Is high-energy ball milling equivalent to a thermal process? *Physical Review Letters*, 64(1):99–102, January 1990.
- [91] P. Villars and L.D. Calvert. *Pearson's handbook of crystallographic data for intermetallic phases*. ASM International, Materials Park, 1991.
- [92] H. Wagner and H. Horner. Elastic interaction and the phase transition in coherent metal-hydrogen systems. *Advances in Physics*, 23:587–637, 1974.
- [93] Bertram E. Warren. *X-Ray Diffraction*. Dover, New York, 1990.
- [94] R.J. Wolf, M.W. Lee, and J.R. Ray. Pressure-composition isotherms for nanocrystalline palladium hydride. *Physical Review Letters*, 73(4):557–560, July 1994.
- [95] Z.-H. Yan. to be published.
- [96] Z.-H. Yan, T. Klassen, C. Michaelsen, M. Oehring, and R. Bormann. Inverse melting in the Ti-Cr system. *Physical Review B*, 47(14):8520–8527, 1993.
- [97] Z.-H. Yan, M.L. Trudeau, A. Van Neste, R. Schulz, D.H. Ryan, P. Tessier, R. Bormann, and J.O. Ström-Olsen. Artificially synthesized non-coherent interfaces in Fe-Ti multilayers and their influence on solid state reactions. In K. Barmak, M.A. Parker, J.A. Floro, R. Sinclair, and D.A. Smith, editors, *Polycrystalline Thin Films: Structure, Texture, Properties and Applications*,

volume 343 of *Symposium proceedings*, pages 235-240, Pittsburgh, 1994. Materials Research Society.

- [98] A.E. Yermakov, V.A. Barionov, and E.E. Yurchikov. *Fiz. Metal. Metalloved.*, 54:935, 1982.
- [99] A.E. Yermakov, E.E. Yurchikov, and V.A. Barionov. *Fiz. Metal. Metalloved.*, 52:1184, 1981.
- [100] J.Y. Ying, J.B. Benziger, and H. Gleiter. Photoacoustic infrared spectroscopy of nanometer-sized Al_2O_3 clusters and cluster-assembled solids. *Physical Review B*, 48(3):1830-1836, July 1993.
- [101] H. Zabel and H. Peisl. Sample-shape-dependent phase transition of hydrogen in niobium. *Physical Review Letters*, 42:511-514, 1979.
- [102] H. Zabel and H. Peisl. *Acta Metallurgica*, 28:589, 1980.
- [103] A. Zaluska. private communication.
- [104] L. Zaluski, P. Tessier, D.H. Ryan, C.B. Doner, A. Zaluska, J.O. Ström-Olsen, M.L. Trudeau, and R. Schulz. Amorphous and nanocrystalline Fe-Ti prepared by ball-milling. *Journal of Materials Research*, 3(12):3059-3068, December 1993.
- [105] L. Zaluski, A. Zaluska, and J.O. Ström-Olsen. Hydrogen absorption in nanocrystalline Mg_2Ni formed by mechanical alloying. *Journal of Alloys and Compounds*, 217:245-249, 1995.
- [106] L. Zaluski, A. Zaluska, P. Tessier, J.O. Ström-Olsen, and R. Schulz. Nanocrystalline hydrogen absorbers. 1995 International Symposium on Metastable, Mechanically Alloyed and Nanocrystalline Materials, ISMANAM-95, Quebec City, 1995.
- [107] L. Zaluski, A. Zaluska, P. Tessier, J.O. Ström-Olsen, and R. Schulz. Catalytic effect of Pd on hydrogen absorption in mechanically alloyed Mg_2Ni , LaNi_5 and FeTi. *Journal of alloys and compounds*, 217:295-300, 1995.
- [108] L. Zaluski, A. Zaluska, P. Tessier, J.O. Ström-Olsen, and R. Schulz. Effects of relaxation on hydrogen absorption in Fe-Ti produced by ball milling. *Journal of alloys and compounds*, 227:53-57, 1995.
- [109] Y. Zhao. *Hydrogen in amorphous Ni-based alloys - The chemical potential and the diffusion constant*. PhD thesis, McGill University, Montréal, 1994.
- [110] X. Zhu, R. Birringer, U. Herr, and H. Gleiter. X-ray diffraction studies of the structure of nanometer-sized crystalline materials. *Physical Review B*, 35(17):9085-9090, June 1987.